NOVEL RF CMOS INTEGRATED CIRCUITS AND SYSTEMS FOR BROADBAND DIELECTRIC SPECTROSCOPY

A Dissertation

by

MASOUD MOSLEHI BAJESTAN

Submitted to the Office of Graduate and Professional Studies of
Texas A&M University
in partial fulfillment of the requirements for the degree of

DOCTOR OF PHILOSOPHY

Chair of Committee,	Kamran Entesari
Committee Members,	Sam Palermo
	Jun Zou
	Mahmoud El-Halawagi
Head of Department,	Miroslav M. Begovic

December 2015

Major Subject: Electrical Engineering

ABSTRACT

Broadband dielectric spectroscopy has proven to be a valuable technique for characterization of chemicals and biomaterials. It has the great potential to become an indispensable and cost-effective tool in point-of-care medical applications due to its label-free and non-invasive operation. However, most of the existing dielectric spectroscopy instruments require bulky, heavy and expensive measurement set-up, restricting their use to only special applications in industry and laboratories. Therefore, integrated dielectric spectroscopy on silicon capable of direct detection of chemicals/biomaterials' complex permittivity can yield significant cost and size reduction, system integration, portability, enormous processing, and high throughput.

A CMOS wideband dielectric spectroscopy system is proposed for chemical and biological material characterization. The complex permittivity detection is performed using a configurable harmonic-rejecting receiver capable of indirectly measuring the complex admittance of sensing capacitor exposed to the material-under-test (MUT) and subject to RF signal excitation with a frequency range of 0.62-10 GHz. The sensing capacitor is embedded in a voltage divider topology with a fixed capacitor and the relative variations in the magnitude and phase of the voltages across the capacitors are used to find the real and imaginary parts of the permittivity. The sensor achieves an rms permittivity error of less than 1% over the entire operation bandwidth.

Using a sub-harmonic mixing scheme, the system can perform complex permittivity measurements from 0.62 to 10 GHz while requiring an input signal source with frequency range of only from 5 to 10 GHz. Thereby, the permittivity measurement system can be easily made self-sustained by implementing a 5-10 GHz frequency

synthesizer on the same chip. One of the key building blocks in such a frequency synthesizer is the voltage-controlled oscillator (VCO) which has to cover an octave of frequency range. A novel low-phase-noise wide-tuning range VCO is presented using a triple-band LC resonator. The implemented VCO in 0.18μm CMOS technology achieves a continuous tuning range of 86.7% from 5.12 GHz to 12.95 GHz while drawing 5 to 10 mA current from 1-V supply. The measured phase noise at 1 MHz offset from carrier frequencies of 5.9, 9.12 and 12.25 GHz is -122.9, -117.1 and -110.5 dBc/Hz, respectively. Also, a dual-band quadrature voltage-controlled oscillator (QVCO) is presented using a transformer-based high-order LC-ring resonator which inherently provides quadrature signals without requiring noisy coupling transistors as in traditional approaches. The proposed resonator shows two possible oscillation frequencies which are exploited to realize a wide-tuning range QVCO employing a mode-switching transistor network. Due to the use of transformers, the oscillator has minimal area penalty compared to the conventional designs. The implemented prototype in a 65-nm CMOS process achieves a continuous tuning range of 77.8% from 2.75 GHz to 6.25 GHz while consuming 9.7 to 15.6 mA current from 0.6-V supply. The measured phase noise figure-of-merit (FoM) at 1 MHz offset ranges from 184 dB to 188.2 dB throughout the entire tuning range. The QVCO also exhibits good quadrature accuracy with 1.5° maximum phase error and occupies a relatively small silicon area of 0.35 mm^2.

To my parents,

and

To my amazing wife, Samira

ACKNOWLEDGEMENTS

This work could have not been accomplished without the help and support of others. First of all, I would like to deeply thank my research advisor, Prof. Kamran Entesari for his continuous support and encouragement, his valuable guidance, and his incredible patience throughout my graduate studies at Texas A&M University. I also wish to thank Prof. Sam Palermo, Prof. Jun Zou, and Prof. Mahmoud El-Halwagi for serving on my committee and reviewing this thesis.

This research has been made possible due to the support and help from a large number of friends who have helped make my stay in College Station a pleasant and memorable experience. I would like to especially thank my best friends Hajir Hedayati, Ehsan Zhian Tabassy, Vahid Dabbagh Rezaei, Alireza Pourghorban Saghati, Ali Pourghorban Saghati, Ali Agha-Mohammadi, Negar Rashidi, Saman Kabiri, and Shokoufeh Arbabi, each of whom gave me a lot of help in many aspects and made my time at Texas A&M unforgettable. By being part of Analog and Mixed-Signal Group, I also had the pleasure of working with many other graduate students including but not limited to Ahmed A. Helmy, Mohamed El-Kholy, Eugene Foli, and Hubert Attah. Thank you all for the great help during the past several years.

I would like to express my deepest gratitude to my parents. I find myself in great debt to them for their unconditional love, sacrifice and support.

Finally and foremost, I would like to thank my wife, Samira, for her encouragement, patience, support and sacrifice throughout all these years. This work would have not been possible without her.

TABLE OF CONTENTS

Page

LIST OF FIGURES

FIGURE Page

LIST OF TABLES

TABLE Page

1. INTRODUCTION

1.1 Complex Permittivity Definition

The dielectric permittivity of any material is a frequency dependent complex quantity ($\varepsilon(\omega) = \varepsilon'(\omega) - j\varepsilon''(\omega)$) which has a real part $\varepsilon'(\omega)$ describing how much energy from an external electric field is stored in a material, and an imaginary part $\varepsilon''(\omega)$ showing how lossy a material is to an external electric field [4]. The dependency of the complex permittivity, $\varepsilon(\omega)$, on frequency, for a large class of compounds, is represented by frequency dispersive equations. Many representations exist for frequency dispersive complex permittivities. One of the most common representations is the Cole-Cole equation [2, 3] and is given by

$$\varepsilon(\omega) = \varepsilon'(\omega) - j\varepsilon''(\omega) = \varepsilon_\infty + \frac{\varepsilon_0 - \varepsilon_\infty}{1 + (j\omega\tau)^{1-\alpha}}. \tag{1.1}$$

where ε_0 and ε_∞ are the "static" and "infinite frequency" dielectric constants, ω is the angular frequency, τ is the characteristic relaxation time, and α is the distribution parameter which takes a value between 0 and 1. As an example, Fig. 1.1 shows the complex permittivities of ethanol and methanol as a function of frequency using their reported Cole-Cole parameters [2, 3].

1.2 Broadband Dielectric Spectroscopy

Broadband Dielectric spectroscopy (BDS) is the measurement of complex permittivity of a material over a wide frequency range. BDS is a versatile and powerful technique for characterization of materials' properties with a wide range of industrial, scientific and medical applications such as oil exploration and processing [5], food and drug safety [6–8], chemical/biological sensing, and disease diagnosis [9–11], to

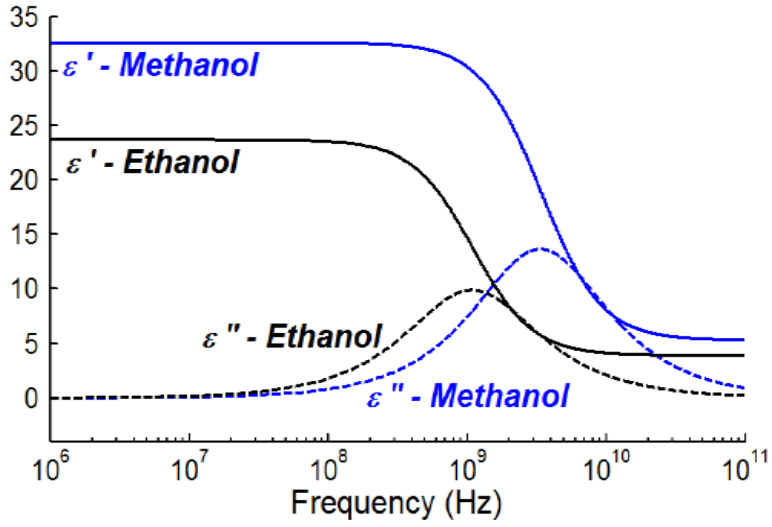

Fig. 1.1: Complex permittivty of ethanol and methanol versus frequency following the Cole-Cole model.

name a few. More specifically, because of the non-invasive, label-free and real-time nature of dielectric spectroscopy, it has the great potential to become a valuable and cost-effective tool for point-of-care medical applications [12]. The techniques for complex dielectric spectroscopy can be generally classified into time-domain [13–15] and frequency-domain [16–20] techniques. The time-domain techniques have the advantage of detecting the permittivity versus frequency at once by sensing the reflection profile of a step voltage applied to a transmission line exposed to the material under test (MUT). In frequency-domain based sensors, a frequency sweep generator is needed to find the frequency dispersive properties of the permittivity separately at each frequency. Existing instruments for BDS incorporate conventional microwave sensors such as waveguide and transmission-lines along with a vector network analyzer (VNA) or scope [21, 22]. These instruments are thereby constrained by high cost and bulky size of measurement set-up and require large volume of MUT, making them unsuitable for portable applications. On the other hand, the advantages

of BDS would be widely available if a miniaturized and low cost instrument could be implemented. This motivates the development of a silicon-based integrated BDS system which in addition to considerable reduction in size and cost, can achieve high-throughput measurements with enormous data processing using only a small volume of MUT.

Recently, several CMOS-based integrated dielectric spectroscopy systems have been reported in literature [23–26]. A self-sustained system was proposed in [23] for the detection of the real part of permittivity over the frequency range of 7-9 GHz. An integrated capacitive sensor exposed to the MUT is placed inside the LC tank of a voltage-controlled oscillator (VCO) and hence, the free running frequency of the VCO changes according to the dielectric constant of the MUT. The VCO is then embedded in a phase-locked loop (PLL) which translates the variation in the free running frequency of the VCO into a change in the VCO control voltage for further analysis and processing. Another PLL-based sensing system proposed in [24] utilizes a reference VCO, in addition to the sensing VCO, and a fractional-N frequency synthesizer architecture to further improve the system sensitivity by tracking the low-frequency drifts caused by environmental variations. However, both of the designs in [23] and [24], suffer from several drawbacks including: 1) the maximum sensing frequency range is determined by the tuning range of the LC-VCO and thereby these systems are not able to cover a very wide frequency band, 2) only the real part of complex permittivity can be detected, and 3) the VCO might fail to operate for very lossy materials due to substantial drop in the quality factor of the LC tank. As opposed to PLL-based architectures, [25] measures the S_{21} characteristics of an off-chip center-gapped transmission line using an integrated heterodyne downconversion architecture to realize the permittivity detection in a wide frequency range from 50 MHz to 3 GHz. Another work reported in [26] incorporates an on-chip coplanar waveguide (CPW)

transmission-line sensor with an integrated heterodyne receiver front-end, enabling the complex permittivity measurements from 1 to 50 GHz. Since both of the designs in [25] and [26] incorporate the conventional heterodyne scheme for frequency down-conversion, they need two separate signal sources for input RF and LO signals with frequency coverage equal to the desired sensing range.

In the second section of this dissertation, a novel integrated sensing system is presented for complex dielectric spectroscopy in the 0.62-10 GHz frequency range. A capacitive sensor exposed to the MUT shows variations in its admittance according to the complex permittivity of MUT. The sensing capacitor along with a fixed capacitor forms a voltage divider circuit and is excited by an RF signal at the sensing frequency. The magnitude and phase of the voltages across the two capacitors which depend on the sensor admittance are measured using a quadrature downconversion architecture to find the real and imaginary parts of the MUT's permittivity. At the lower frequency end, the system is configured as a direct-conversion architecture with 3^{rd} and 5^{th} harmonic-rejection to alleviate the problem of harmonic mixing and improve the sensitivity. On the other hand, at the higher frequency end, the system works as a dual-downconversion topology and employs a sub-harmonic mixing technique to reduce the required input clock frequency span. As a proof of concept, the spectroscopy system is used for complex permittivity detection of pure organic chemicals and shows an rms permittivity error of less than 1% over the frequency range of 0.62-10 GHz. The fabricated chip in 0.18-μm CMOS occupies an active area of 2.3 mm^2 and consumes 65-72 mW from a 1.8 V supply.

The second section also provides an in-depth analysis on the BDS system performance and its permittivity detection sensitivity. The impacts of different non-idealities of a downconversion architecture such as harmonic mixing, noise, gain compression and dc offset are analyzed and it is shown how the system deals with

these non-idealities to achieve the best performance.

1.3 Wideband Frequency Generation

The proposed permittivity measurement system can be easily made self-sustained by implementing a 5-10 GHz frequency synthesizer on the same chip to generate the RF excitation signal for the sensor, as well as the LO signals for the downconversion path. One of the key building blocks in such a frequency synthesizer is the voltage-controlled oscillator (VCO) which has to cover an octave of frequency range. A single-tank LC VCO relying on only switched capacitor technique cannot cover such a wide frequency range while satisfying the required phase noise performance. Alternatively, multiple VCOs can be employed. However, this technique requires large silicon area and therefore increases the cost. Other techniques have been reported to widen the oscillator tuning range including VCOs exploiting switched inductors [2] and coupled inductors [3]-[6]. The VCOs based on switched inductors suffer from poor phase noise performance due to the loss of the switches inside the tank. On the other hand, in the VCOs with coupled inductors, the multi-oscillation modes of the resonator are employed to make a multi-band oscillator without using lossy switches to achieve better phase noise performance and more compact layout. Using this technique, two novel wideband VCOs are proposed in this dissertation as follows

Chapter 3 presents a low-phase-noise wide-tuning range VCO using an LC resonator with three potential oscillation modes. Implemented in 0.18μm CMOS technology, the VCO prototype achieves a continuous tuning range of 86.7% from 5.12 GHz to 12.95 GHz while drawing 5 to 10 mA current from 1-V supply. The measured phase noise at 1 MHz offset from carrier frequencies of 5.9, 9.12 and 12.25 GHz is -122.9, -117.1 and -110.5 dBc/Hz, respectively. The VCO occupies a chip area of 0.33 mm^2.

In Chapter 4, a novel dual-band quadrature voltage-controlled oscillator (QVCO) is presented using a transformer-based LC ring. In contrary to the conventional approaches that use transistor-coupled LC oscillators, the proposed resonator inherently provides quadrature signals by employing both magnetic and capacitive couplings in a ring structure, resulting in low phase noise performance and high quadrature accuracy. Additionally, it offers two oscillation modes which are exploited to realize a wide-tuning-range QVCO. The implemented prototype in a 65-nm CMOS process shows 2.75-6.25 GHz continuous tuning range, phase noise figure-of merit (FoM) of 188.2 dB at 3 GHz and better than 184 dB across the entire operating frequency range, 1.5° maximum phase error while consuming 9.7-15.6 mA from 0.6-V supply. The QVCO occupies an active chip area of 0.35 mm^2.

2. A BROADBAND DIELECTRIC SPECTROSCOPY SYSTEM IN CMOS*

2.1 Proposed BDS System

The proposed integrated BDS system is composed of two essential parts: 1) a sensing capacitor which its complex admittance changes based on the dielectric permittivity of the exposed MUT, and 2) the interface circuitry which indirectly measures the complex admittance of the sensing element. The key design techniques for the capacitive sensor and the fundamental operation of the proposed system are presented in this section.

2.1.1 Sensing Element

The dielectric permittivity of any material is a frequency dependent complex quantity ($\varepsilon(\omega) = \varepsilon'(\omega) - j\varepsilon''(\omega)$) which has a real part $\varepsilon'(\omega)$ describing the energy storage and an imaginary part $\varepsilon''(\omega)$ accounting for energy losses [4]. Accordingly, a capacitor-based sensor exposed to the MUT and excited by a signal at the sensing frequency (f_s) can be used to detect the MUT's complex permittivity at f_s. As shown in Fig. 2.1(a), the sensing capacitor has an interdigitated structure and is implemented using the uppermost metal layer of CMOS process. The passivation layer on top of the metals is removed in order to make a direct contact with the sensor's electrodes and maximize its sensitivity. As illustrated in Fig. 2.1(b), the fringing

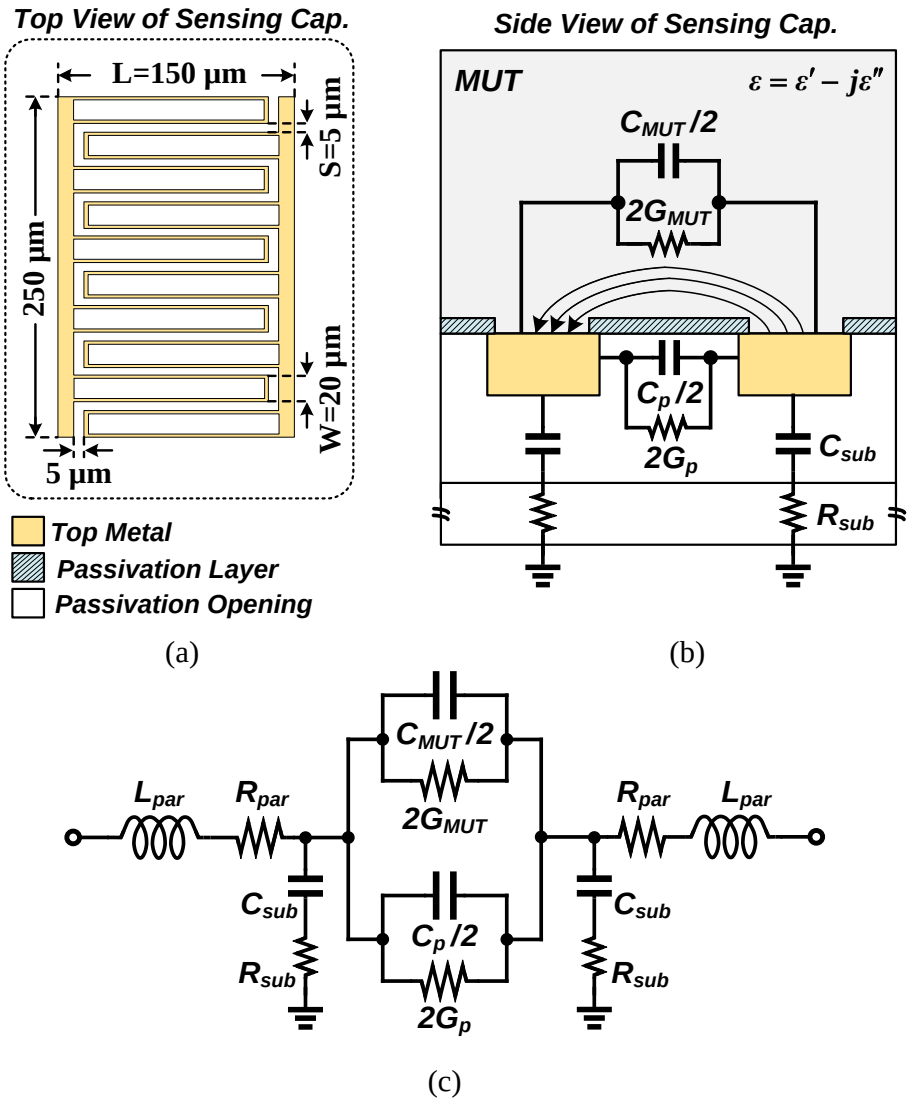

Fig. 2.1: (a) Layout of the interdigitated sensing capacitor, (b) side view of the sensing capacitor for two adjacent electrodes with a simple equivalent circuit model [1], (c) a more accurate model for the interdigitated capacitor including the series parasitic resistance and inductance of the electrodes.

electric fields above the interdigital electrodes pass through the MUT; therefore, the capacitance and conductance between the two adjacent electrodes become a function of the material permittivity. From Fig. 2.1(b), the admittance of the sensor (Y_s)

at a certain frequency can be decomposed into two parts; 1) a material-dependent part (Y_{MUT}) which varies depending on the complex permittivity of MUT and can be modeled with a parallel combination of a capacitor (C_{MUT}) and a conductor (G_{MUT}). C_{MUT} provides a measure of the total energy storage in the MUT and is only a function of ε' while G_{MUT} represents the total energy loss in the MUT and only depends on ε'', 2) a material-independent part (Y_{fixed}) which is fixed for different MUTs and only depends on the sensing element geometry. Y_{fixed} includes the parasitic capacitance and resistance to the substrate (C_{sub}, R_{sub}) and between the adjacent electrodes (C_p, R_p).

Consequently, Y_s can be written as

$$\begin{aligned} Y_s &= G_s + j\omega C_s = Y_{fixed} + Y_{MUT} \\ &= Y_{fixed} + (G_{MUT} + j\omega C_{MUT}) = f(\varepsilon'') + jg(\varepsilon'). \end{aligned} \tag{2.1}$$

where $f(.)$ and $g(.)$ are ideally linear functions. Equation (2.1) shows that the real (imaginary) part of Y_s is only a function of ε'' (ε') and is independent of ε' (ε''). As will be discussed in more detail in Section 2.5.2, this property results in a simple calibration procedure for the system and makes it possible to detect ε' and ε'' independently. However, it should be noted that at very high frequencies, the simple equivalent model in Fig. 2.1(b) might not be accurate as the series parasitic inductance and resistance (R_{par} and L_{par}) of the electrodes become more significant and neglecting their effects can degrade the accuracy of permittivity detection. A more detailed expression for total admittance of the sensor Y_t can be obtained using the equivalent model shown in Fig. 2.1(c) as follows

$$Y_t = \frac{G_s + j\omega C_s}{(1 + G_s R_{par} - L_{par} C_s \omega^2) + j\omega \left(R_{par} C_s + L_{par} G_s\right)}. \tag{2.2}$$

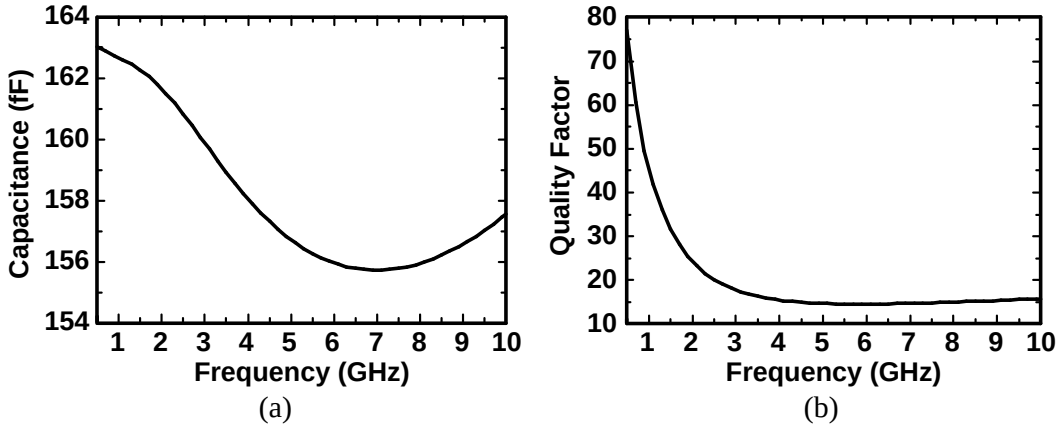

Fig. 2.2: Simulated (a) capacitance and (b) quality factor of the sensing capacitor in the frequency range of 0.5-10 GHz when exposed to air ($\varepsilon' = 1$, $\varepsilon'' = 0$).

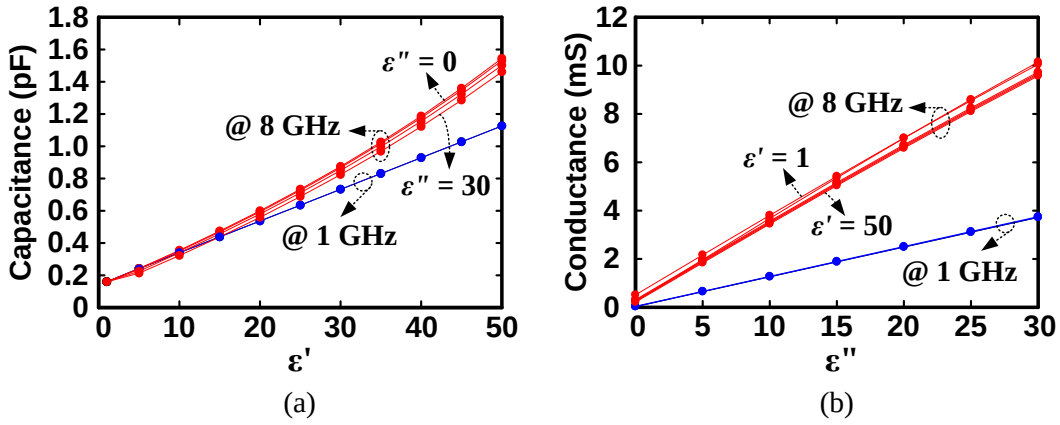

Fig. 2.3: Simulated capacitance of the sensing capacitor versus ε' at frequencies of 1 GHz and 8 GHz for different values of ε'' ($0 \leq \varepsilon'' \leq 30$), (b) simulated conductance of the sensing capacitor versus ε'' at frequencies of 1 GHz and 8 GHz for different values of ε' ($1 \leq \varepsilon' \leq 50$).

Due to the presence of R_{par} and L_{par}, the real and imaginary parts of Y_t become a function of both ε' and ε''. Therefore, for frequencies that R_{par} and L_{par} values are not negligible, considering real and imaginary parts of Y_t as functions of only ε'' and ε', respectively, may lead to an increase in the detection error.

From the above discussion, the geometry of the sensor including the number of fingers (n), their width (W), their length (L) and the spacing between them (S), shown in Fig. 2.1(a), must be chosen based on two important considerations: 1) making R_{par} and L_{par} negligible at the maximum desired sensing frequency and 2) maximizing the sensor sensitivity. For example, by increasing W, the parasitic resistance and inductance can be minimized but at the cost of an increase in the parasitic capacitance to the substrate or equivalently a degradation in sensitivity. Also, while increasing the number of fingers can result in better sensitivity, it lowers the self-resonance frequency of the interdigitated capacitors, limiting its maximum operating frequency. Therefore, depending on the frequency band of operation, there are optimum values for the sensor dimensions resulting in the maximum sensitivity and also a simple model for the sensor. Several EM simulations were carried out using the EM simulator Sonnet to find the optimum values for n, W, L and S. Fig. 2.2 shows the simulated capacitance and quality factor of the designed sensing capacitor in the frequency range of 0.5-10 GHz when exposed to air ($\varepsilon' = 1$, $\varepsilon'' = 0$). It can be seen that the simulated capacitance of the unloaded sensor has very small variations and shows a quality factor of higher than 15 over the entire bandwidth. The self-resonance frequency of the designed sensor was found to be around 60 GHz which is much higher than the maximum sensing frequency of interest (10 GHz). To show the dependence of the real and imaginary parts of Y_s on the complex permittivity, EM simulations are performed for the complex permittivities in the range of $1 \leq \varepsilon' \leq 50$, $0 \leq \varepsilon'' \leq 30$ and at frequencies of 1 GHz and 8 GHz. Fig. 2.3(a) and (b) show that the simulated sensor capacitance (conductance) at 1 GHz is a function of only ε' (ε'') and is almost independent of ε'' (ε'). However, at a higher frequency of 8 GHz, capacitance and conductance also show slight variations with ε'' and ε', respectively, verifying the aforementioned discussion.

2.1.2 Basic System Architecture

From the previous section, the admittance of the sensor ($Y_s(j\omega)$) changes depending on the complex permittivity of MUT. Therefore, the goal of the dielectric spectroscopy system is to accurately measure the sensor admittance over a wide frequency range. To do so, the sensing capacitor is first embedded inside a voltage divider topology with a fixed capacitor C_f, as shown in Fig. 2.4 [27,28]. The circuit is then excited at node A with a sinusoidal signal at the desired sensing frequency (f_s). For this configuration, the admittance of the sensor can be related to the voltages at node A (V_A) and node B (V_B) based on the following equation

$$Y_s(j\omega) = j\omega C_f \left(\frac{V_A}{V_B} - 1\right). \tag{2.3}$$

At any given frequency ωC_f is fixed and does not change for different MUTs. Accordingly, the sensor admittance which is a representation of the complex permittivity of MUT can be found by measuring the relative magnitude and phase shift of V_B with respect to V_A. In order to obtain the magnitude and phase information of V_A and V_B, nodes A and B are applied to two separate quadrature direct-conversion architectures, as shown in Fig. 2.4. Each quadrature direct-conversion architecture consists of two mixers driven by in-phase (I) and quadrature-phase (Q) LO signals at frequency of f_s, and two low-pass filters (LPFs) which are employed to remove the high frequency components at the output of mixers. The RF signals V_A and V_B are therefore decomposed into real and imaginary parts at the output of I and Q channels, respectively. Subsequently, the ratio between V_A and V_B can be found using the dc signals V_{IA}, V_{QA}, V_{IB} and V_{QB} generated at the output of LPFs as

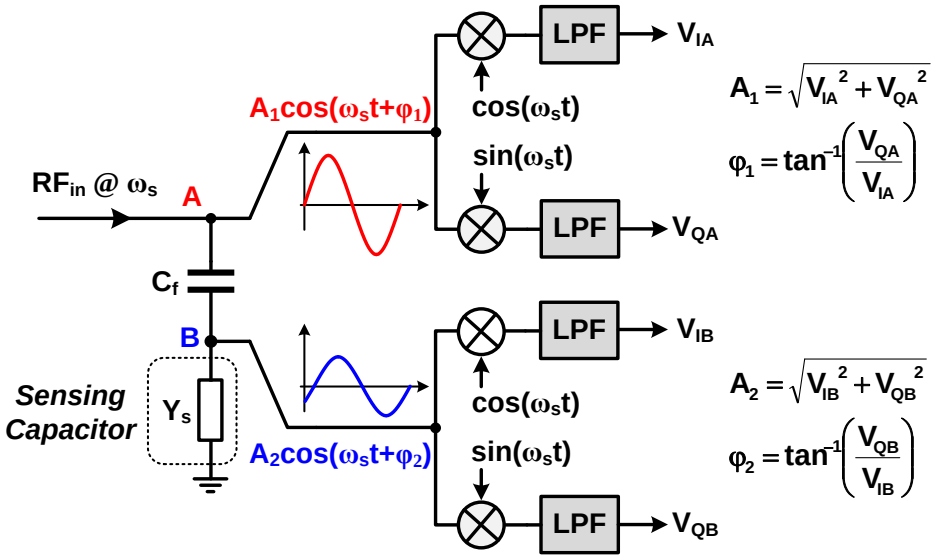

Fig. 2.4: A conceptual block diagram of the proposed dielectric spectroscopy system.

follows

$$\frac{V_A}{V_B} = \frac{V_{IA} + jV_{QA}}{V_{IB} + jV_{QB}}. \tag{2.4}$$

Substituting (2.4) into (2.3), the complex admittance of the sensor or equivalently the complex permittivity of MUT can be found as

$$Y_s(j\omega) = f(\varepsilon'') + jg(\varepsilon') = j\omega C_f \left(\frac{V_{IA} + jV_{QA}}{V_{IB} + jV_{QB}} - 1\right). \tag{2.5}$$

Using two separate direct-conversion branches for detecting magnitude and phase information of V_A and V_B has two major drawbacks: 1) it significantly increases the area and power consumption, and 2) any mismatch between the two downconversion paths can lead to inaccurate permittivity detection. To overcome these issues, Either V_A or V_B is selected to be applied to the mixers through two identical switchable LNAs, as depicted in Fig. 2.5. At any time only one of the LNAs is active and passes

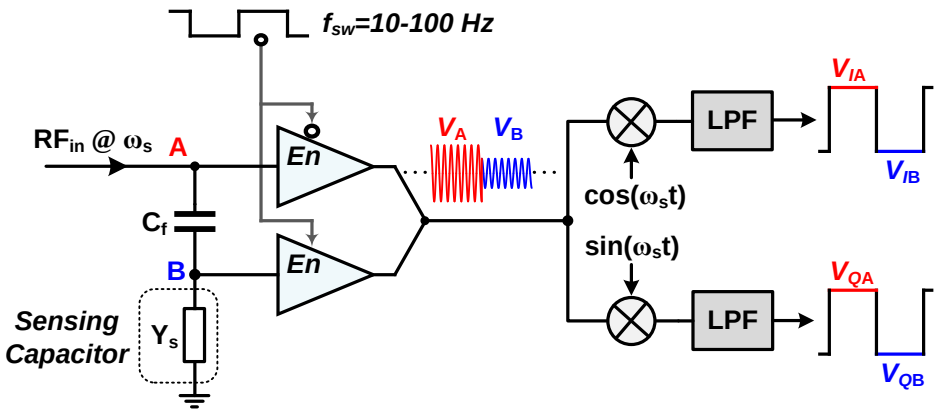

Fig. 2.5: Using two switchable LNAs to eliminate the need for two independent downconversion paths.

the signal at its input to the I-Q mixers. The switching frequency (f_{sw}) of the LNAs must be chosen low enough to ensure that the dc signals at the output of system are settled down to their final values. In other words, f_{sw} is selected based on the settling time of the system or the cut-off frequency of LPFs (f_c). Assuming the use of off-chip LPFs with cut-off frequency of around 1 kHz, f_{sw} is chosen to be within 10-100 Hz.

2.2 System Non-Idealities

This section analyzes the effects of different non-idealities of a direct-conversion architecture such as harmonic mixing, noise, gain compression and dc offset on the spectroscopy system performance.

2.2.1 Harmonic Mixing

In the previous section, it was assumed that the sensor is excited with a single-tone sinusoid at the targeted sensing frequency f_s, and consequently the sensor admittance at f_s can be easily related to the output dc voltages of the system as in (2.5). However, when the system input signal (RF_{in}) is generated on-chip, it cannot

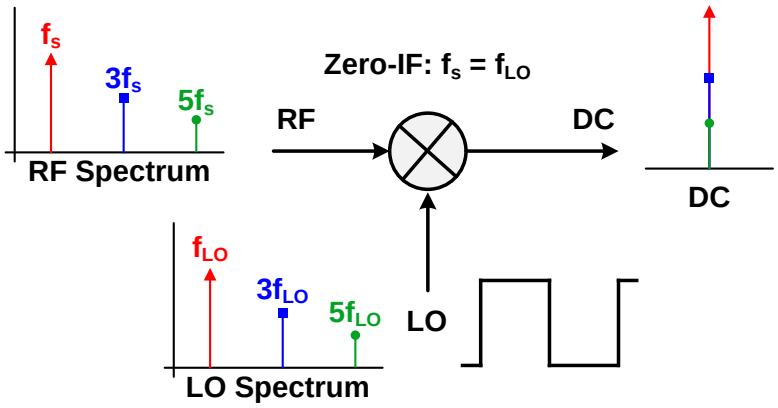

Fig. 2.6: Harmonic mixing problem.

be purely sinusoidal and besides the fundamental frequency at f_s, it also contains frequency components at odd harmonics of f_s ($3f_s$, $5f_s$, ...). The even harmonics are assumed to be negligible as all the circuits in the system are differential. On the other hand, due to the hard switching phenomenon in the mixers, the effective LO signal is more like a square wave. Therefore, as illustrated in Fig. 2.6, along with fundamental component of RF_{in}, its odd harmonics are also translated to dc after mixing with the corresponding odd harmonics of LO. As a result, the dc voltages at the output of I-Q channels also contain information about the sensor admittance at odd harmonics of f_s, meaning the detection of permittivity at f_s is distorted. For a wideband spectroscopy system, this issue is especially more problematic at lower frequencies where the system input signal generated by frequency dividers is rich of harmonics, all residing in the input frequency range of the sensor. In the following, it is analytically shown how the presence of input harmonics influences the system performance and degrades the accuracy of permittivity detection.

Considering a double-balanced mixer, the Fourier series representation of the

square wave LO illustrated in Fig. 2.6 is given by

$$v_{LO}(t) = \frac{4}{\pi} \sum_{\substack{n=1 \\ n\ odd}}^{\infty} \frac{1}{n} cos\left(n\omega_s t\right) \tag{2.6}$$

Now assume that the applied RF signal to the system at node A in Fig. 2.4 has frequency content at not only the fundamental frequency f_s, but also all odd harmonics of f_s as follows

$$v_A(t) = \sum_{\substack{n=1 \\ n\ odd}}^{\infty} A_n cos\left(n\omega_s t + \varphi_n\right) \tag{2.7}$$

where A_n and φ_n $(n = 1, 3, 5, ...)$ are the amplitude and phase of the n^{th}-order harmonic, respectively. Therefore, using superposition the voltage at node B can be simply found as

$$v_B(t) = \sum_{\substack{n=1 \\ n\ odd}}^{\infty} A'_n cos\left(n\omega_s t + \varphi'_n\right) \tag{2.8}$$

where

$$A'_n = \frac{A_n}{\left|1 + \dfrac{Y_s\left(jn\omega_s\right)}{jn\omega_s C_f}\right|}. \tag{2.9}$$

$$\varphi'_n = \varphi_n - \angle\left(1 + \frac{Y_s\left(jn\omega_s\right)}{jn\omega_s C_f}\right). \tag{2.10}$$

After multiplying $v_A(t)$ and $v_B(t)$ with $v_{LO}(t)$ and neglecting the high frequency

Table 2.1: Calculated DF and the resulting admittance detection error for five different MUTs.

MUT	$f_s = 1$ GHz		$f_s = 3$ GHz	
	DF	error%	DF	error%
Air	$0.966 - j0.003$	1.15	$0.982 - j0.002$	0.35
Butan-1-ol	$0.985 + j0.017$	4.27	$0.992 + j0.008$	1.35
DMSO	$0.984 - j0.045$	5.80	$0.991 - j0.038$	1.9
Methanol	$0.94 - j0.04$	9.28	$0.955 - j0.032$	2.78
Ethanediol	$0.902 - j0.023$	12.76	$0.962 - j0.017$	3.36

components, the dc voltages V_{IA}, V_{QA}, V_{IB} and V_{QB} can be obtained as follows

$$V_{IA} + jV_{QA} = \frac{4}{\pi} \sum_{\substack{n=1 \\ n\ odd}}^{\infty} \frac{A_n}{n} e^{j\varphi_n} \tag{2.11}$$

$$V_{IB} + jV_{QB} = \frac{4}{\pi} \sum_{\substack{n=1 \\ n\ odd}}^{\infty} \left(\frac{A_n}{n} e^{j\varphi_n} \frac{1}{1 + \dfrac{Y_s\left(jn\omega_s\right)}{jn\omega_s C_f}} \right) \tag{2.12}$$

As discussed earlier, the sensor admittance is detected based on the measured values of V_{IA}, V_{QA}, V_{IB} and V_{QB} using

$$Y_{s,detected}(j\omega_s) = j\omega_s C_f \left(\frac{V_{IA} + jV_{QA}}{V_{IB} + jV_{QB}} - 1 \right) \tag{2.13}$$

By substituting (2.11) and (2.12) in (2.13), the detected admittance $Y_{s,detected}$ is found as a function of the actual admittance value Y_s as follows

$$Y_{s,detected}(j\omega_s) = DF.Y_s(j\omega_s) + (DF - 1)\,.j\omega_s C_f \tag{2.14}$$

DF is called distortion factor and is given by

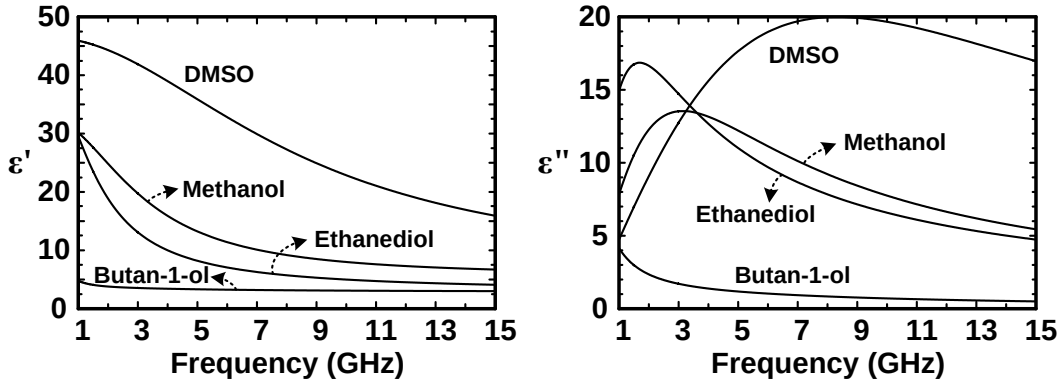

Fig. 2.7: ε' and ε'' curves over the frequency range of 1-15 GHz for butan-1-ol, DMSO, ethanediol and methanol [2].

$$DF = \frac{1 + \sum\limits_{\substack{n=3 \\ n\ odd}}^{\infty} \frac{A_n}{nA_1} e^{j(\varphi_n - \varphi_1)}}{1 + \sum\limits_{\substack{n=3 \\ n\ odd}}^{\infty} \left(\frac{A_n}{nA_1} e^{j(\varphi_n - \varphi_1)} \frac{1 + \frac{Y_s(j\omega_s)}{j\omega_s C_f}}{1 + \frac{Y_s(jn\omega_s)}{jn\omega_s C_f}} \right)} \tag{2.15}$$

Ideally, when the excitation signal is a sinusoid ($A_3 = A_5 = \ \cdots = 0$), $DF = 1$ and as expected $Y_{s,detected} = Y_s$. However, upon the presence of input harmonics, there will be an error in the detected admittance given by

$$\begin{aligned} error\% &= 100 \times \left| \frac{Y_{s,detected}(j\omega_s) - Y_s(j\omega_s)}{Y_s(j\omega_s)} \right| \\ &= 100 \times \left| (DF - 1) \left(1 + \frac{j\omega_s C_f}{Y_s(j\omega_s)} \right) \right| \end{aligned} \tag{2.16}$$

As it is clear from (2.15) and (2.16), the error in the detected admittance is highly a function of the sensor admittance (or equivalently the values of ε' and ε'' at f_s and its odd harmonics). In other words, the permittivity detection error caused by harmonic mixing is material-dependent. In order to gain an idea of how large this

error can be, assume the worst case scenario where V_A is also a square wave as the LO signal with a Fourier series representation as in (2.6) and f_s is a low sensing frequency. Therefore, DF can be written as

$$DF = \frac{1 + \sum\limits_{\substack{n=3 \\ n\ odd}}^{\infty} \frac{1}{n^2}}{1 + \sum\limits_{\substack{n=3 \\ n\ odd}}^{\infty} \left(\frac{1}{n^2} \frac{1 + \frac{Y_s(j\omega_s)}{j\omega_s C_f}}{1 + \frac{Y_s(jn\omega_s)}{jn\omega_s C_f}} \right)} \tag{2.17}$$

To calculate DF, only harmonics below 15 GHz are considered and higher order harmonics are assumed to be zero as they are highly attenuated and have minimal effect on the value of DF. Now, assuming $f_s = 1$ GHz, the sensor admittance is simulated over the frequency range of 1-15 GHz using Sonnet for five different MUTs including air, butan-1-ol, DMSO, ethanediol and methanol. The simulated admittance values are then substituted in (2.16) and (2.17) to find the overall admittance detection error. Table 2.1 shows the calculated DF and the resulting admittance detection error for the considered MUTs for $f_s = 1$ GHz and 3 GHz. In order to provide more insight, the values of ε' and ε'' of each MUT over the frequency range of 1-15 GHz are shown in Fig. 2.7 [2]. By comparing Fig. 2.7 with the calculated detection errors in Table 2.1, it can be concluded that MUTs showing small variations in ε' and ε'' with respect to frequency, result in a lower error. This can be also deduced from (2.15). For example, consider an especial case when $Y_s(j\omega) = jC_s\omega$, in which C_s is always fixed. In this case, the numerator and denominator of DF in (2.15) become equal, thereby, $DF = 1$ or equivalently $Y_{s,detected} = Y_s$ ($error = 0$). It is worth mentioning that although ε' and ε'' of air are constant ($\varepsilon' = 1, \varepsilon'' = 0$), the sensor admittance itself shows some variation with frequency (see Fig. 2.2), resulting

a small detection error even for air.

2.2.2 DC Offsets

One of the inherent problems affecting a direct-conversion architecture is the presence of dc offsets at the output of I and Q channels [29]. In the proposed system, dc offsets can substantially corrupt the desired output dc signals, hence degrading the system performance. DC offsets can be mainly generated by two mechanisms in the system; 1) passive or active device mismatches between the positive and negative branches of the differential circuits along the signal path, and 2) self-mixing of LO signals leaking into the RF port of the mixers. The dc offsets generated by these mechanisms can be considered as static, because their values are constant and do not change for different MUTs. This is in contrast to the unwanted dc signals caused by harmonic mixing phenomenon which are material-dependent, as discussed in previous section. It is important to note that any LO signal leaking into the input of the LNA in the proposed system will play the same role as the input RF excitation signal and thereby does not generate dc offset. This is in contrast to what happens in direct-conversion radios where the LO leakage component at the input of LNA can produce much larger dc offset as it is amplified by the LNA before self-mixing [29].

The foregoing discussion implies that the system must incorporate some means of offset cancellation to prevent degradation in permittivity detection. Since the overall gain of the system is around 30-40 dB, the generated dc offset at the output of I and Q paths are not that large to cause saturation in the baseband circuits. Because of this fact and since dc offsets are static, a simple calibration procedure can be employed to cancel out the dc offset. First, prior to the experiments, the two LNAs in Fig. 2.5 are switched off and the dc levels at the outputs of I and Q channels are measured which are in fact equal to the dc offsets of the corresponding channel.

The measured dc offsets are then subtracted from the final composite signals, leaving only the desired dc terms at the end.

2.2.3 Noise

Noise performance of the system determines its admittance sensitivity, or equivalently the minimum admittance level that it can detect. Assuming the system is noiseless, and neglecting any other non-ideality, the system can accurately measure V_A and V_B, thereby, the sensor admittance can be precisely found as

$$Y_s = Y_f \left(\frac{V_A}{V_B} - 1 \right). \tag{2.18}$$

When the system is noisy, there is an uncertainty in the measured values of V_A and V_B, leading to uncertainty in the calculated admittance using (2.18). By referring the output voltage noises of the system back to the inputs, (2.18) can be rewritten as

$$Y_s + \Delta Y_s = Y_f \left(\frac{V_A + v_{n,A}}{V_B + v_{n,B}} - 1 \right). \tag{2.19}$$

where $v_{n,A}$ and $v_{n,B}$ denote the input referred noise voltages at nodes A and B, respectively and ΔY_s is the uncertainty in the calculated admittance. By subtracting (2.18) from (2.19), ΔY_s is derived as

$$\Delta Y_s = Y_f \frac{V_A}{V_B} \left(\frac{\frac{v_{n,A}}{V_A} - \frac{v_{n,B}}{V_B}}{1 + \frac{v_{n,B}}{V_B}} \right). \tag{2.20}$$

Since $\frac{v_{n,B}}{V_B} \ll 1$, (2.20) reduces to

$$\Delta Y_s = Y_f \frac{V_A}{V_B} \left(\frac{v_{n,A}}{V_A} - \frac{v_{n,B}}{V_B} \right). \tag{2.21}$$

After writing V_B as a function of V_A using (2.18) and substituting into (2.21), ΔY_s can be expressed as

$$\Delta Y_s = \frac{Y_s + Y_f}{V_A}\left(v_{n,A} - \frac{Y_s + Y_f}{Y_f} v_{n,B}\right). \tag{2.22}$$

Now, in order to evaluate the admittance sensitivity of the system, the input referred voltage noise PSDs are integrated over a particular bandwidth to calculate their rms values. The integration bandwidth is determined by the cutoff frequency of the low pass filter (f_c). The rms values of the input-referred noise voltages at node A and B are approximately equal, i.e., $v_{n,A,rms} \approx v_{n,B,rms} = v_{n,in,rms}$. Thus, the minimum detection level (MDL) of the system can be written as

$$MDL = |\Delta Y_s| \approx \frac{|Y_s + Y_f|}{|V_A|}\sqrt{\left(1 + \left|\frac{Y_s + Y_f}{Y_f}\right|^2\right)} v_{n,in,rms}. \tag{2.23}$$

Two important observations can be made from (2.23). 1) As expected, MDL can be minimized by maximizing the amplitude of the input voltage excitation signal ($|V_A|$) and minimizing $v_{n,in,rms}$. As will be discussed in the next section, the maximum acceptable value of $|V_A|$ is determined by the linearity of the system. 2) By increasing $|Y_s|$, MDL increases, meaning the system is less sensitive for larger admittance values. Therefore, depending on the required sensitivity and the noise performance of the system, the maximum acceptable value of $|Y_s|$ can be found using (2.23).

2.2.4 Gain Compression

As the input signal of the downconversion chain increases, the output signal level calculated by $V_o = \sqrt{{V_I}^2 + {V_Q}^2}$ increases linearly until the system enters a nonlinear region where the gain is no longer constant. At 1-dB compression point (1-dB CP),

the system can experience substantial detection error as will be explained in the following.

Since the sensor admittance is capacitive, the amplitude of V_A is always higher than the amplitude of V_B. Consequently, as the input excitation current to the system increases, V_A enters into the gain compression region before V_B. Therefore, V_A and V_B might experience different gains when reaching to the output, causing an error in the detected admittance using (2.18). To quantify this effect, assume the gain of the system for V_A and V_B to be G_A and G_B, respectively. Thus, the detected admittance can be written as

$$Y_{s,detected} = Y_f \left(\frac{G_A}{G_B} \frac{V_A}{V_B} - 1 \right). \tag{2.24}$$

Therefore, from (2.18) and (2.24), the detection error is found as

$$error\% = 100 \times \left| \frac{Y_{s,detected} - Y_s}{Y_s} \right| = 100 \times \left| 1 + \frac{Y_f}{Y_s} \right| \left| \frac{G_A}{G_B} - 1 \right| \tag{2.25}$$

To gain more insight, consider a special case when $Y_s = Y_f$. For this case, assuming a gain mismatch of 1 dB between G_A and G_B, the error is calculated to be as large as 21.7% while for a gain mismatch of 0.1 dB the detection error reduces to 2.3%.

The foregoing study implies that $|V_A|$ must be chosen very carefully to ensure operation in the linear region for all values of Y_s. This can be done by sufficiently backing off from the 1-dB CP.

2.3 Overall System Architecture and Operation

As discussed earlier, one of the critical concerns in the proposed BDS system is harmonic mixing phenomenon within mixers which can cause severe permittivity detection error especially at the lower frequency end of the operating band. In order

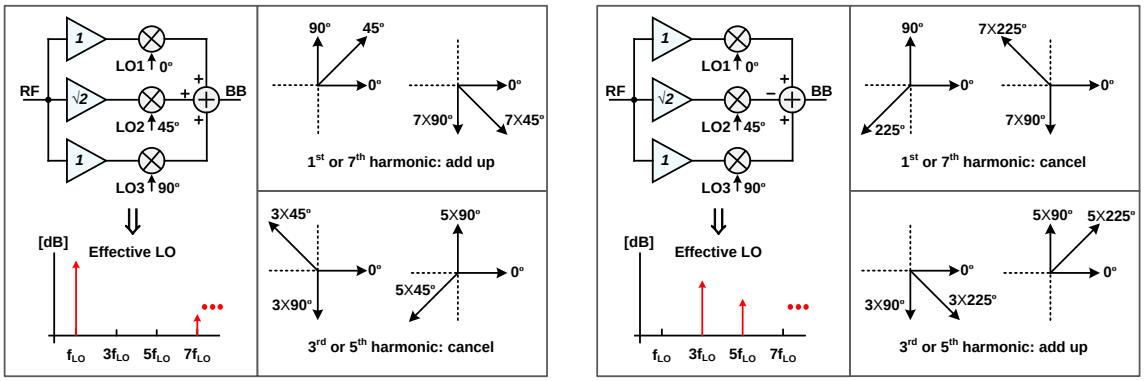

Fig. 2.8: The conceptual block diagram, the effective LO spectrum and the vector diagram for (a) an HRM, and (b) an SHM.

to reduce the effects of harmonic mixing, harmonic rejection mixers (HRM) are employed in this design as in wideband radio receivers [30–32]. The key concept in an HRM is to emulate a sine wave LO by amplitude weighting and adding phase shifted square-wave LOs. Fig. 2.8(a) shows an example, where the combination of an amplitude scaling of $1 : \sqrt{2} : 1$ and three 45° phase shifted LOs results in third and fifth harmonics rejection. However, the seventh and ninth harmonics are still remained at the output. By exploiting more LO phases, one can reject more harmonics but at the expense of higher power consumption and considerable complexity in the LO generation circuitry.

The third and fifth harmonic rejection ratios (HRR) of the HRM in Fig. 2.8(a) are usually limited to 30 to 40 dBc due to phase and gain mismatch between the three mixing paths [31,32]. Also, as mentioned above, this HRM is not able to reject the seventh and ninth harmonics. In order to see the effects of these limitations on the overall system accuracy, the detection error due to harmonic mixing is calculated as in Section 2.2.1 when $f_s = 1$ GHz and for two different cases; 1) Assuming an ideal HRM with complete suppression at $3^{\text{rd}}, 5^{\text{th}}, 11^{\text{th}}, 13^{\text{th}}, \ldots$ harmonics, and 2)

Table 2.2: Calculated DF and the resulting admittance detection error at 1 GHz for two different cases of 1) assuming an ideal HRM, and 2) assuming an actual HRM with 30 dBc HRR at all third, fifth, ... harmonics.

MUT	Case 1		Case 2	
	DF	error%	DF	error%
Air	$0.9994 - j0.0004$	0.26	$0.9993 - j0.0004$	0.29
Butan-1-ol	$0.9974 + j0.0031$	1.1	$0.9971 + j0.0035$	1.21
DMSO	$0.9935 - j0.0141$	2.21	$0.9932 - j0.0149$	2.34
Methanol	$0.9821 - j0.0063$	2.99	$0.981 - j0.0071$	3.2
Ethanediol	$0.9756 - j0.0006$	3.76	$0.9737 - j0.0001$	4.05

Assuming an actual HRM with HRR of only 30 dBc at all $3^{\text{rd}}, 5^{\text{th}}, 11^{\text{th}}, 13^{\text{th}}, \ldots$ harmonics. The calculated errors for different MUTs are summarized in Table 2.2. By comparing the results in Table 2.1 and 2.2, it can be observed that the use of an HRM can significantly mitigate the problem of harmonic mixing. Also, from Table 2.2, there is no that much difference between the calculated detection errors in the two considered cases. This implies that any extra efforts to improve HRR might only increase the power consumption and complexity with minimal improvement on the overall performance.

The HRM in Fig. 2.8(a) can be also configured to synthesize an effective LO frequency of greater than f_{LO} by simply flipping the polarity of the middle mixing path (Fig. 2.8(b)) [33]. In this case, as can be seen from the vector diagram of Fig. 2.8(b), the fundamental and seventh harmonics are rejected while the third and fifth mixing components remained at the output. To not be confused with the HRM in Fig. 2.8(a), this configuration is called sub-harmonic mixer (SHM) as it requires an LO signal that is a fraction of the desired downconversion frequency. The SHM is used in the proposed BDS system to reduce the required frequency tuning range of the master clock, as will be explained later in this section. Note that compared to the

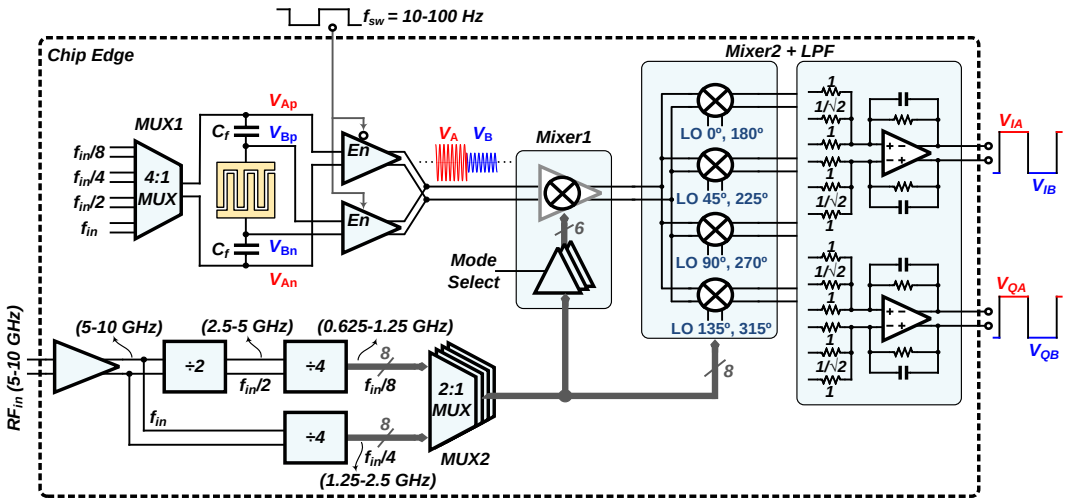

Fig. 2.9: Complete block diagram of the proposed dielectric spectroscopy system.

HRM, the conversion gain of the SHM is reduced by 9 dB due to the lower amplitude of the third harmonic in the square wave LO. This attenuation, if required, can be easily compensated in the preceding RF stages or baseband amplifiers.

The generation of multiple LO phases is essential for the operation of an HRM. One of the most common approaches to generate these phases is to use frequency dividers. A divider-by-four, for example, can provide eight 45° phase shifted LO signals required for the HRM in Fig. 2.8(a). The main drawback of this technique is the necessity of a master clock running at four times higher than the required LO frequency by HRM, which significantly increases the power consumption and complicates the design of frequency generation circuits. However, the HRM is mainly required only at the lower frequency end of the spectrum where LO harmonics lie in-band. At the higher frequency end, due to the limited bandwidth of frequency dividers and the RF blocks in downconversion path, the effects of harmonic mixing are negligible and the HRM becomes surplus.

Fig. 2.9 shows the complete block diagram of the BDS system. The system is

capable of covering the entire sensing frequency of 0.625-10 GHz using an external input differential signal of 5-10 GHz. The operation bandwidth from 0.625-10 GHz is divided into four sub-bands (SB1-SB4), each covering an octave of frequency range. The sensing signals in SB4 with frequency of 5-10 GHz (f_{in}) are provided externally; while a set of frequency dividers are used to generate the sensing frequencies in SB1, SB2 and SB3 equivalent to $f_{in}/8$, $f_{in}/4$ and $f_{in}/2$, respectively. The divide-by-4 circuits provide the required eight LO phases for mixers. An analog multiplexer (MUX1) is used to select the appropriate RF excitation signal according to the targeted sensing frequency. MUX1 also attenuates the high amplitude signals present at its inputs to a level sufficiently below the 1-dB CP of the proceeding stages to ensure operation in the linear region and mitigate the problem of gain compression (Section 2.2.4).

The downconversion chain is comprised of two cascaded mixers to alleviate the problem of harmonic mixing at the lower frequency end of spectrum while reducing the required input clock frequency span using the idea of SHM discussed earlier. Mixer1 has two operating modes and can be configured to act as 1) a buffer or 2) an SHM with effective LO frequency of $3f_{LO}$ and $5f_{LO}$. Mixer2 is a standard quadrature HRM with third and fifth harmonic suppression exploiting eight LO phases. As will be further explained later, the gain scaling is accomplished in the baseband instead of in the RF domain to minimize the probability of gain mismatch and thereby improve harmonic rejection performance. For SB1 and SB2 which are vulnerable to harmonic mixing, Mixer1 operates as buffer without doing any frequency translation. Mixer2 then downconverts its RF input signal to dc while rejecting the third and fifth harmonic mixing components. As a result, the system is equivalent to a direct-conversion architecture with third and fifth harmonic suppression as illustrated in Fig. 2.10(a). On the other hand, in SB3 and SB4 where the harmonic rejection requirement be-

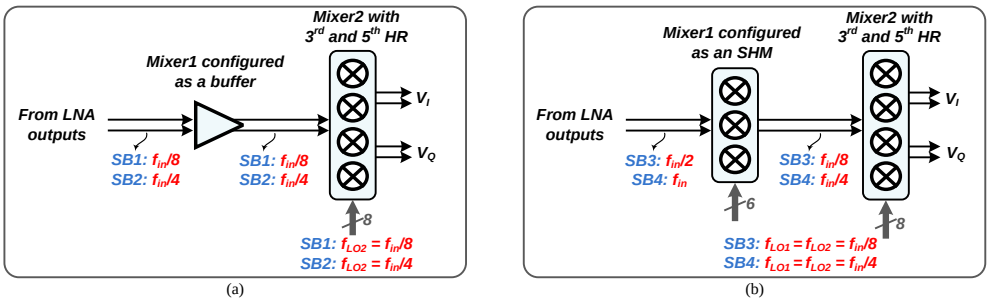

Fig. 2.10: System configuration when operating in (a) SB1 and SB2, (b) SB3 and SB4.

comes more relaxed, the system works as a dual-downconversion architecture. As shown in Fig. 2.10(b), Mixer1 is configured to work as an SHM with effective LO frequency of $3f_{LO}$ and $5f_{LO}$. Consequently, the signal at the RF port of Mixer1 is downconverted to an IF signal with a frequency of $f_{in}/8$ and $f_{in}/4$ in SB3 and SB4, respectively which is then translated into dc at the output of Mixer2. Therefore, the entire downconversion frequency range of 0.625-10 GHz can be synthesized using eight phases of an LO with frequency of 0.625-2.5 GHz.

Table 2.3 shows the different bands for sensing frequencies and the corresponding frequency ranges applied to the sensing capacitor, Mixer1 and Mixer2. As an example, to perform the permittivity detection in SB3, MUX1 is set to apply $f_{in}/2$ to the sensing capacitor. Either V_A or V_B is then selected to be applied to Mixer1 through switchable LNAs. MUX2 selects the LO signal frequency of Mixer1 to be $f_{in}/8$. The effective LO frequency of Mixer1 is therefore at $3f_{in}/8$ and $5f_{in}/8$, both producing an IF signal with frequency of $f_{in}/8$. This IF signal is finally translated to dc at the output of Mixer2 with an LO frequency of $f_{in}/8$.

Table 2.3: The different bands for sensing frequencies and the corresponding frequency ranges applied to the sensing capacitor, Mixer1 and Mixer2.

Freq. sub-band	**SB1**	**SB2**	**SB3**	**SB4**
Freq. range applied to the sensing cap.	$f_{in}/8$	$f_{in}/4$	$f_{in}/2$	f_{in}
Freq. range applied to Mixer1	-	-	$f_{in}/8$	$f_{in}/4$
Effective LO freq. of Mixer1	no freq. translation	no freq. translation	$3f_{in}/8, 5f_{in}/8$	$3f_{in}/4, 5f_{in}/4$
Freq. range applied to Mixer2	$f_{in}/8$	$f_{in}/4$	$f_{in}/8$	$f_{in}/4$

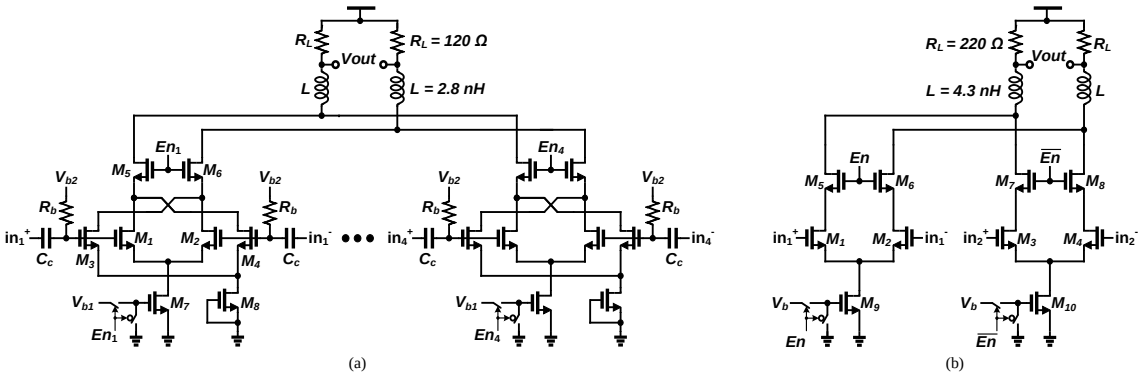

Fig. 2.11: Circuit schematic of (a) MUX1, and (b) switchable LNA.

2.4 Circuit Implementation

This section describes the architecture and circuit implementation of the main building blocks of the BDS system including MUX1, switchable LNA, Mixer1, Mixer2 and frequency dividers. The simulation results for the entire system will be presented at the end of this section.

2.4.1 4:1 Analog Multiplexer (MUX1)

Fig. 2.11(a) demonstrates the circuit schematic of MUX1 implemented in this design consisting of four NMOS differential pairs with a shared output load. The desired input is selected by enabling the bias current of the corresponding differential pair and connecting the gates of cascode devices to V_{DD}. The cross-connected

transistors (M_3, M_4) have the same dimension as the main transistors (M_1, M_2) in each differential pair and are used to neutralize the effect of the parasitic gate-drain capacitances of M_1 and M_2, resulting in more isolation between the input and output ports. Also, cascode transistors (M_5, M_6) are added to further improve the isolation. Inductive peacking technique is exploited at the output load to achieve the required high frequency and wideband operation. The signal amplitude at the output of MUX1 can be controlled by adjusting the bias current of the active differential pair. The dividers' outputs with relatively large swings, if directly connected to MUX1, can cause hard switching and substantial non-linearity, producing strong harmonics at the outputs. In order to avoid this issue, the outputs of dividers are capacitively coupled to the MUX1's inputs and the value of the ac coupling capacitors C_c's are chosen to be about 10 times smaller than the input capacitance of each differential pair ($C_c \approx 20$ fF). Therefore, the large swing signals are attenuated before reaching to the MUX1's inputs. The small coupling capacitors also help minimizing the load capacitance seen by the dividers.

2.4.2 LNA

As the first stage in the downconversion path, LNA play a critical role in the overall performance and need to be carefully designed. The noise performance, gain and input impedance are the essential constraints in the design of LNA. It is important to note that unlike the LNA in a radio receiver which is designed for a 50 Ω input impedance, here the LNA can be considered as a voltage amplifier and its input impedance must ideally be infinite not to load the sensing capacitor. As a result, the common-source (CS) topology seems to be the best candidate in this design as it will only contribute a fixed parasitic capacitance to the sensor.

Fig. 2.11(b) depicts the architecture of the switchable LNA. At any time, only

one of the differential CS stages is active and connected to the common output load. Cascode transistors are employed to increase the isolation between the input and output ports and to ensure LNA stability. It should be noted that although increasing the width of $M_1 - M_4$ can increase their transconductance and subsequently decrease the input-referred noise voltage of the LNA, wider transistors add more parasitic capacitances to the sensor, degrading its sensitivity.

The gain of the LNA is designed to be sufficiently large to minimize the noise contribution of the subsequent stages including the mixers and baseband amplifiers. Also, the same as MUX1, the LNA incorporate an inductive series peaking technique to achieve a relatively flat gain response over the desired frequency range of 0.6-10 GHz. In the implemented prototype, the LNA has a simulated average gain of 11 dB with less than 1 dB variation across the whole band while consuming 5.2 mA from 1.8 V supply. The total parasitic input capacitance of the LNA was found to be around 100 fF. The maximum simulated input referred noise voltage of the LNA over the frequency range of 0.6-10 GHz is 1.12 nV/$\sqrt{\text{Hz}}$.

2.4.3 Mixer1

Fig. 2.12 shows the schematic of Mixer1 which consists of three double-balanced Gilbert-cell sub-mixers connected to a common load. As discussed earlier, Mixer1 has two essential operating modes; 1) buffering mode, and 2) sub-harmonic mixing mode. Mode switching is accomplished by connecting the LO ports of the three sub-mixers to either a bias voltage or a specific phase of LO signal, as illustrated in Fig. 2.12. In SB1 and SB2, Mixer1 must be configured as a buffer and no frequency translation should take place at this stage. To do so, all the transistors in the LO switching pairs are turned off except transistors M_1 and M_2 whose gates are connected to V_{DD}. Consequently, Mixer1 is simply converted to a buffer stage with

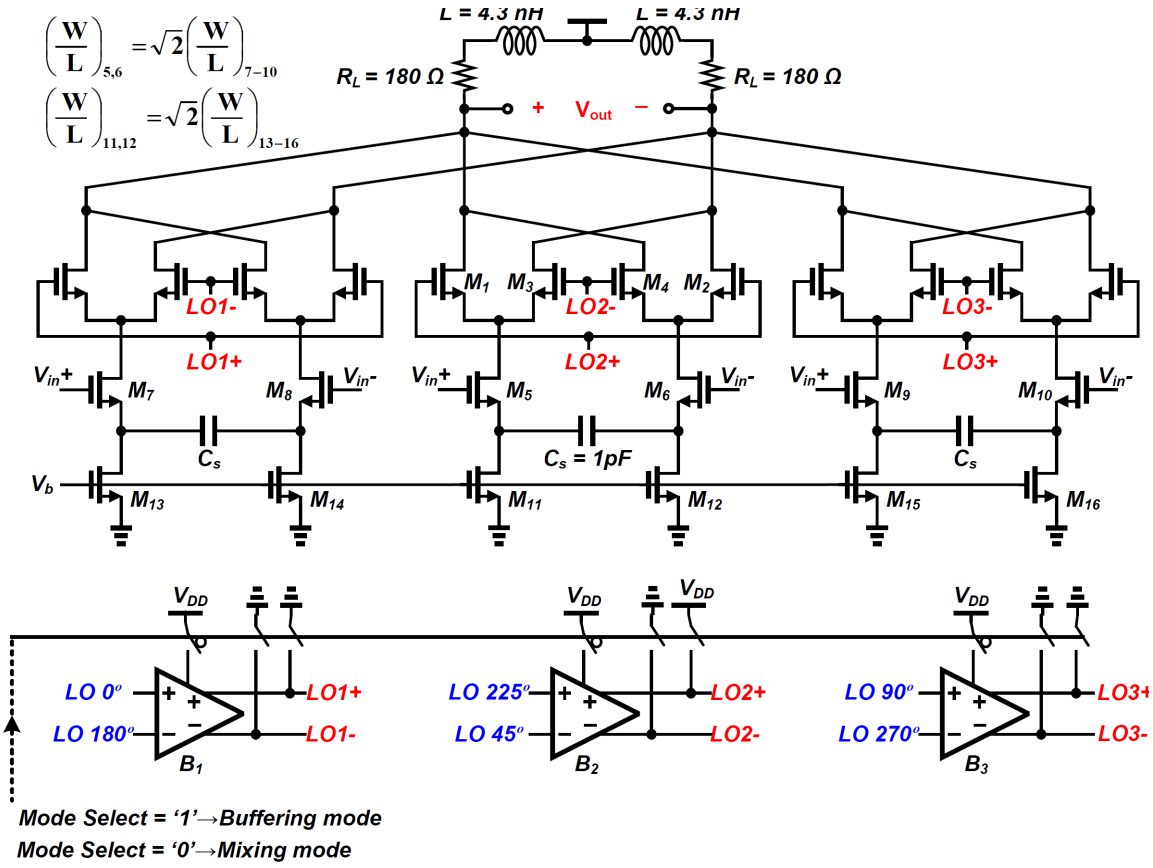

Fig. 2.12: Circuit topology of Mixer1.

transistors M_1 and M_2 acting as cascode devices for M_5 and M_6. On the other hand, in SB3 and SB4 where Mixer1 works as a SHM, each sub-mixer is driven with a different phase of the LO signal through the buffers B_1-B_3. Currents with different phases from the three sub-mixers are summed at the common load to generate the output voltage while canceling the first and seventh harmonic mixing components. Since the cancellation is performed in the current domain, the required amplitude weighting of $\sqrt{2}$ is implemented by scaling the gain of the transconductance stage of the middle sub-mixer through adjusting the bias current and sizes of M_5 and M_6 compared to M_7-M_{10}. Shunt peaking is exploited at the output load of Mixer1 to

achieve a flat conversion gain over the entire band of operation (0.6-2.5 GHz). In the implemented design, Mixer1 provides a voltage gain of about 6 dB in the buffering mode (f_{in} = 0.62-2.5 GHz) while it shows an average conversion gain of 2 dB in the mixing mode (f_{in} = 2.5-10 GHz). The current consumption in the buffering and mixing modes is 2.1 mA and 5 mA, respectively.

One of the main issues in the SHM of Fig. 2.12 is the flicker noise up-conversion of the transconductance devices M_5-M_{10}. Since the frequencies of the applied LO signal and the output IF signal are the same ($f_{LO} = f_{IF}$), the $1/f$ noise of M_5-M_{10} will appear at the output after mixing with f_{LO} in each sub-mixer. Note that the flicker noise up-conversion is done through the fundamental harmonic of LO (f_{LO}) while the RF input is downconverted through the third harmonic ($3f_{LO}$) which has around 9 dB less amplitude. Also, the $1/f$ noise of M_5-M_{10} is typically very large because these transistors are relatively small due to bandwidth constraints. As a result, the SHM can suffer from substantial flicker noise at its output. In order to alleviate this problem, capacitive degeneration is employed for the transconductor transistors, as shown in Fig. 2.12. For the high frequency input RF signal, C_s shows very small impedance and thereby has negligible effect on the conversion gain of the SHM. However, at very low frequencies, C_s is open circuit and the flicker noise up-conversion of M_5-M_{10} is highly attenuated due to very large impedance at the source of these transistors. The sizes of the bias transistors M_{11}-M_{16} are chosen to be very large to minimize their flicker noise contribution at the output. Increasing the length of M_{11}-M_{16} also increases the impedance at the sources of M_5-M_{10} at very low frequencies, further attenuating the flicker noise up-conversion of these devices.

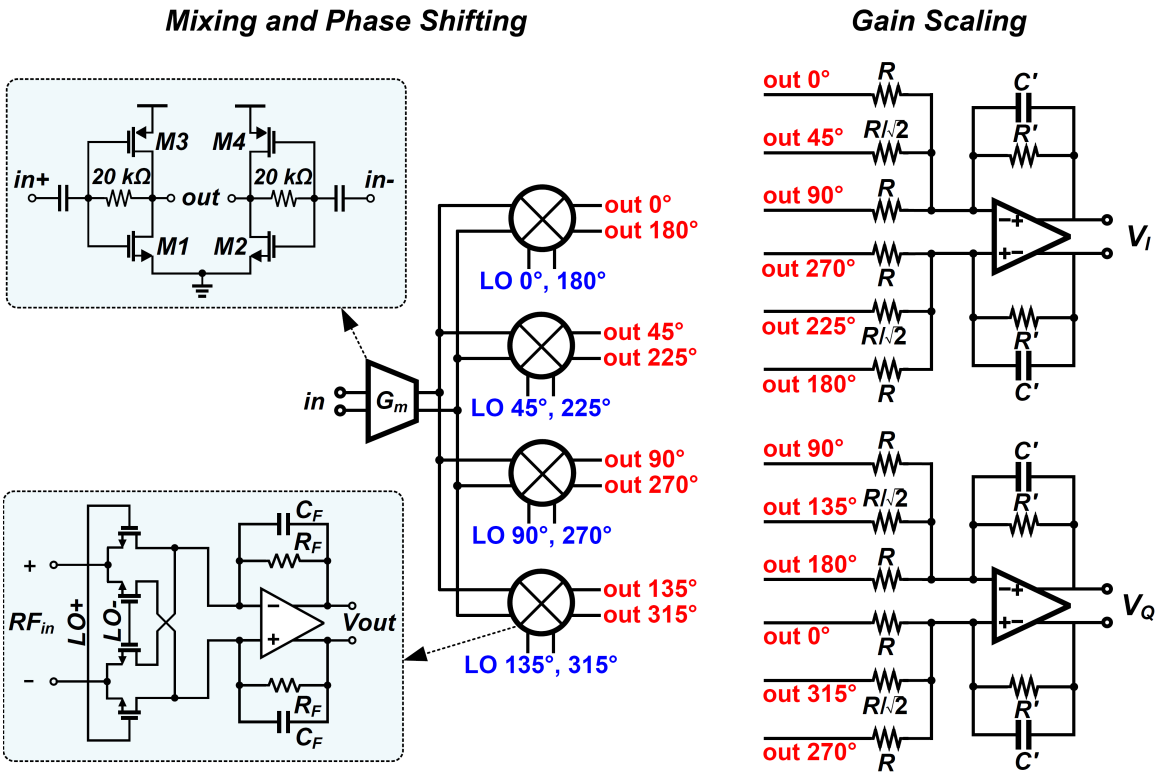

Fig. 2.13: Schematic of Mixer2 with third and fifth harmonics rejection.

2.4.4 Mixer2

The circuit schematic of Mixer2 is shown in Fig. 2.13 which is composed of a G_m cell, four current-driven passive mixers, transimpedance amplifiers (TIA) and a gain scaling stage. Current-driven passive mixers are used due to their low flicker noise and high linearity. Ideally, since no DC current passes through the switches in a passive mixer they will not contribute any flicker noise to the system. The input G_m cell incorporates self-biased inverter-based structure due to its high linearity and larger gain. The four mixers are driven by 45° phase shifted LO signals to generate the output I and Q signals while suppressing the third and fifth harmonics. The TIAs with RC feedback are utilized for current to voltage conversion and low pass

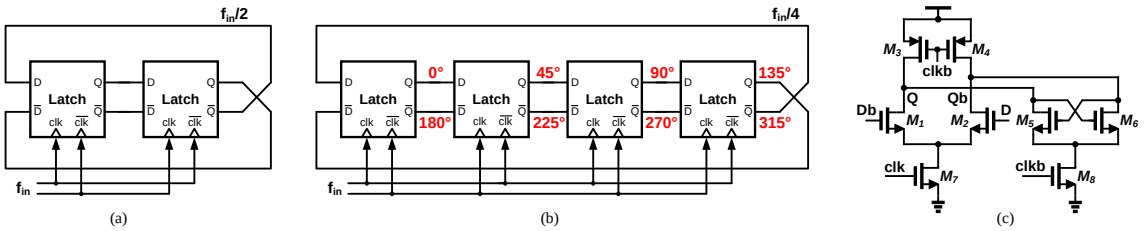

Fig. 2.14: CML frequency divider (a) divider-by-2, (b) divider-by-4 and (c) dynamic-loading D-latch.

filtering. Each R_F resistor is composed of a 5-bit binary-weighted switched resistor bank for gain adjustment. The required gain scaling and voltage summation for third and fifth harmonics rejection is simply realized by employing an opamp-based analog adder as illustrated in Fig. 2.13. Doing the gain scaling in the baseband instead of in the RF domain minimizes the probability of gain mismatch [30]. The harmonic rejection performance of the system can be improved by choosing larger values for the resistors in the gain scaling stage for better matching but at the expense of more thermal noise at the output of the opamps.

Both the TIAs and opamps employ a standard two-stage miller-compensated amplifier structure with common-mode feedback to ensure biasing at $V_{DD}/2$. A class-AB topology is used for the output stage to maximize the output swing.

2.4.5 Frequency Dividers

Since the frequency dividers need to work at a frequency as high as 10 GHz and because of the speed limitations of the 0.18-μm CMOS technology, all of the dividers are implemented using current-mode logic (CML) to achieve a faster dividing operation. As shown in Fig. 2.14(a), the divide-by-2 circuit is implemented by cascading two D-latches with the output of the second latch cross-coupled to the input of the first one. Similarly, the divide-by-4 circuits are realized by cascading four D-latches

to generate the required eight clock phases for both HRM and SHM (Fig. 2.14(b)). To achieve maximum speed with minimum power consumption, dynamic-loading D-latch shown in Fig. 2.14(c) is used in this design [34, 35]. As opposed to the conventional latches where the load is constant, the load in this topology is dynamically controlled using the clock signal based on the operation mode of the latch. In the sensing mode when *clk* is high and *clkb* is low, the two PMOS devices (M_3, M_4) provide low resistance at the load minimizing the RC time constant for faster transitions. On the other hand, in the storing mode, the loading resistance is maximized by connecting the gate of PMOS devices to a high voltage to achieve maximum gain for good latching. The self-oscillating frequency of each divider was intentionally designed to happen at about the high frequency end of the operation bandwidth to reduce the required power consumption of the buffer stages preceding the dividers.

2.4.6 Transistor-level Simulation Results of the Overall System

The simulated linearity performance of the downconversion path (i.e. from the LNA input to the system output) is depicted in Fig. 2.15. With $f_s = 1$ GHz and 8 GHz, the 1-dB CP occurs at an input signal level of about 53 mV and 59 mV, respectively. Note that at $f_s = 1$ GHz, Mixer1 is configured as a buffer while at $f_s =$ 8 GHz, it works as an SHM. Backing off sufficiently from the 1-dB CP, the maximum acceptable input signal level is chosen to be 30 mV. For input signal amplitudes smaller than 30 mV, the response is linear with constant slope of 30.8 dBV/V and 28.5 dBV/V at 1 GHz and 8 GHz, respectively.

Fig. 2.16(a) and (b) show the rms input referred noise voltage of the system ($V_{n,in,rms}$) at all four sub-bands. As can be seen, the system has superior noise performance in SB1 and SB2 mainly due to the higher gain of Mixer1 in the buffering mode and its flicker noise contribution in the mixing mode.

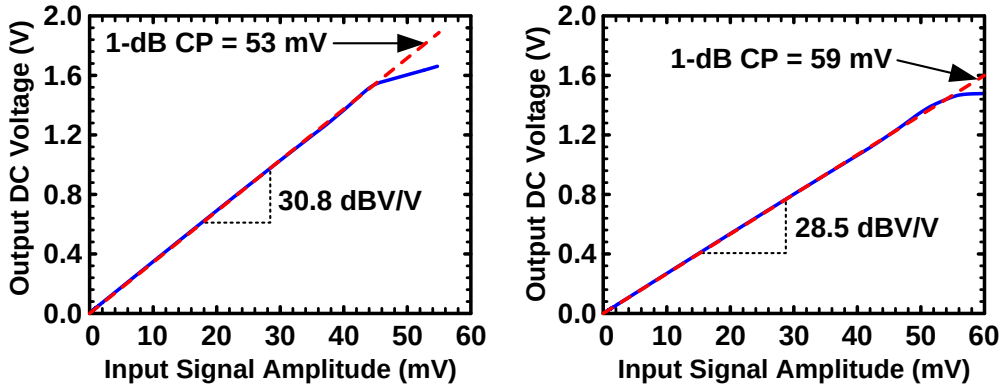

Fig. 2.15: Simulated linearity performance of the downconversion path when (a) $f_s = 1$ GHz, and (b) $f_s = 8$ GHz.

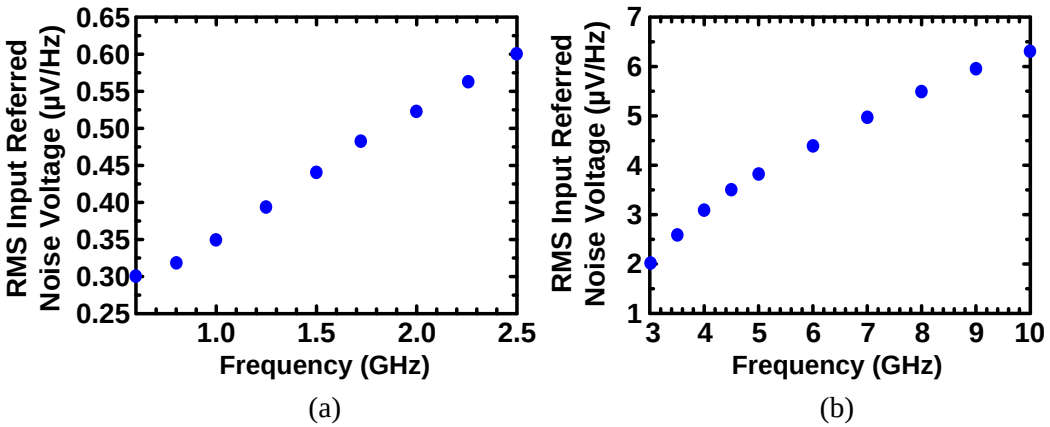

Fig. 2.16: Simulated rms input referred noise of the downconversion path (BW = 10 kHz) at (a) SB1 and SB2, (b) SB3 and SB4.

Having the values of $V_{n,in,rms}$, the system sensitivity at any frequency can be found using (2.23). Fig. 2.17 shows the calculated MDL for different values of $|Y_s + Y_f|$ and at two RF excitation frequencies of 1 GHz (SB1) and 8 GHz (SB4). Assuming $C_f = 200$ fF, the minimum and maximum values of $|Y_s + Y_f|$ at 1 GHz and 8 GHz were calculated based on Fig. 2.3 for $1 \leq \varepsilon' \leq 50$ and $0 \leq \varepsilon'' \leq 30$. From Fig. 2.17, At

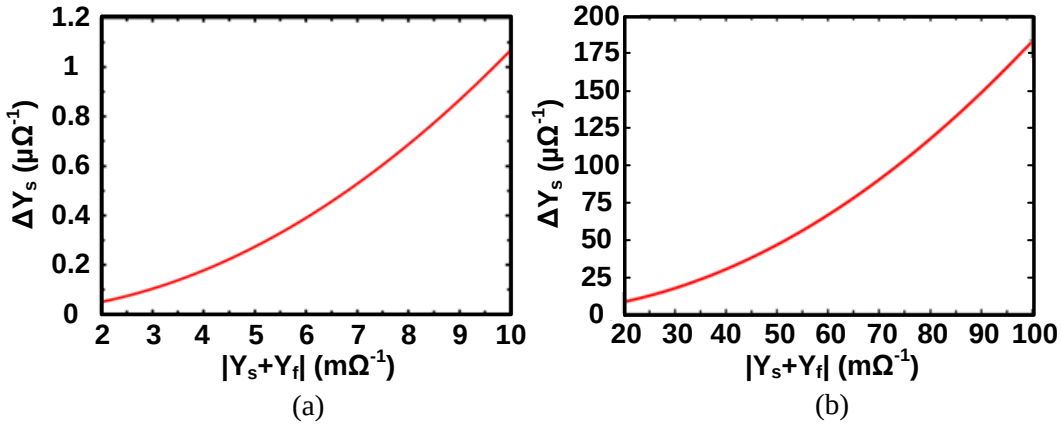

Fig. 2.17: Calculated MDL for different values of $|Y_s + Y_f|$ and at two RF excitation frequencies of (a) 1 GHz and (b) 8 GHz.

$f_s = 1$ GHz (8 GHz), the system is capable of detecting $|\Delta Y_s|$ of 1.05 μS (183.2 μS) for $|Y_s + Y_f|$ as large as 10 mS (100 mS). To gain a better understanding about these numbers, consider the case where Y_s is purely capacitive with a nominal capacitance value of $C_s = 1$ pF. Based on Fig. 2.17, the MDL (ΔC_s) at 1 GHz and 8 GHz for this value of Y_s ($= 2\pi f_s C_s$) is found to be about 0.1 fF and 1.3 fF, respectively. This means that the system is able to detect capacitance variations of as small as 0.1 fF and 1.3 fF at 1 GHz and 8 GHz, respectively, for a sensor with nominal capacitance of 1 pF.

2.5 Measurements

Fig. 2.18(a) shows the chip microphotograph of the BDS system, which was fabricated in an IBM 0.18-μm CMOS process. The total chip area is 3 mm×3 mm with an active core area of 2.3 mm^2. The chip consumes an overall power of 65-72 mW from a 1.8 V supply. The chip was assembled in a 8 mm×8 mm 56-pin, wirebonded QFN package. In order to protect the bondwires during the experiments, the package was partially encapsulated with epoxy such that only the die is open to air (Fig. 2.18(b)).

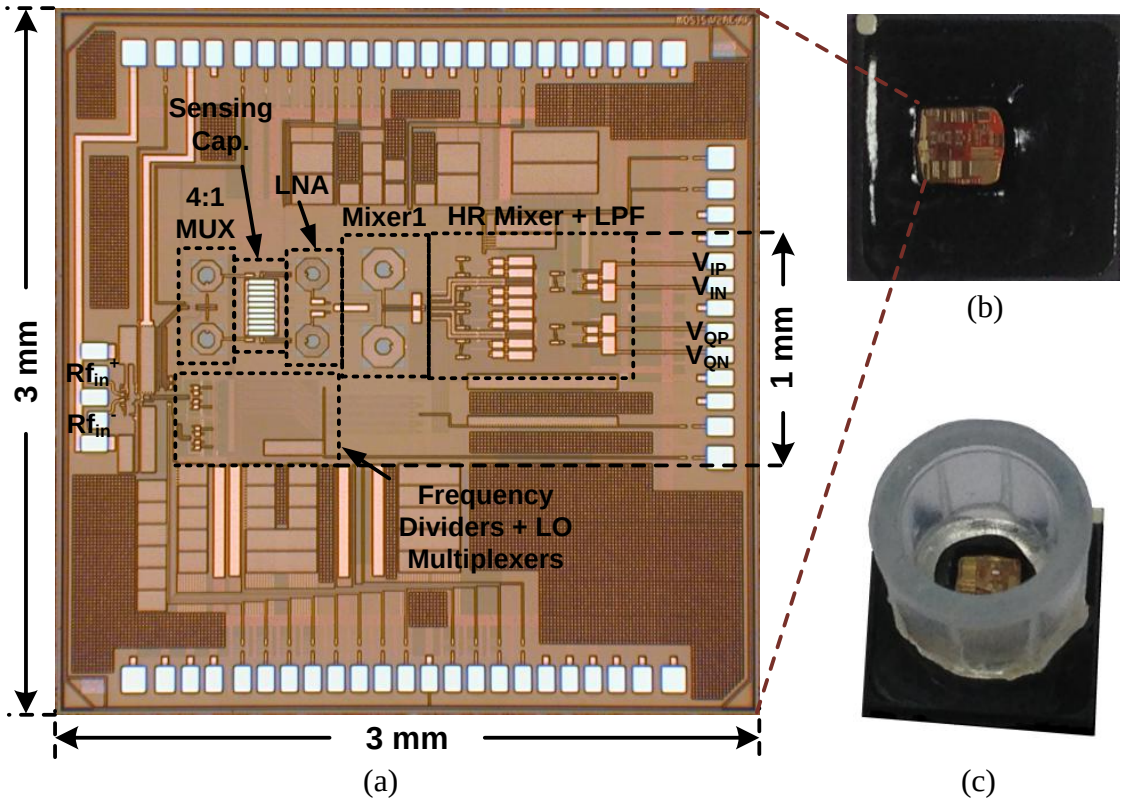

Fig. 2.18: (a) Microphotograph of the fabricated BDS system, (b) packaged chip, (c) plastic tube glued on top of chip.

2.5.1 Test Setup

As shown in Fig. 2.18(c), a cylindrical plastic tube is placed and glued on top of the die to hold the liquid under test. To prevent liquid evaporation, the tube is capped after MUT insertion. A Finnpipette single-channel micropipette is used to inject an accurate volume of the test liquid into the tube. To ensure that the measured results are independent of the sample volume, all measurements were performed with volumes of around 20 μL which was found to be sufficiently higher than the sensor saturation volume [23]. After material characterization, the liquid is first removed

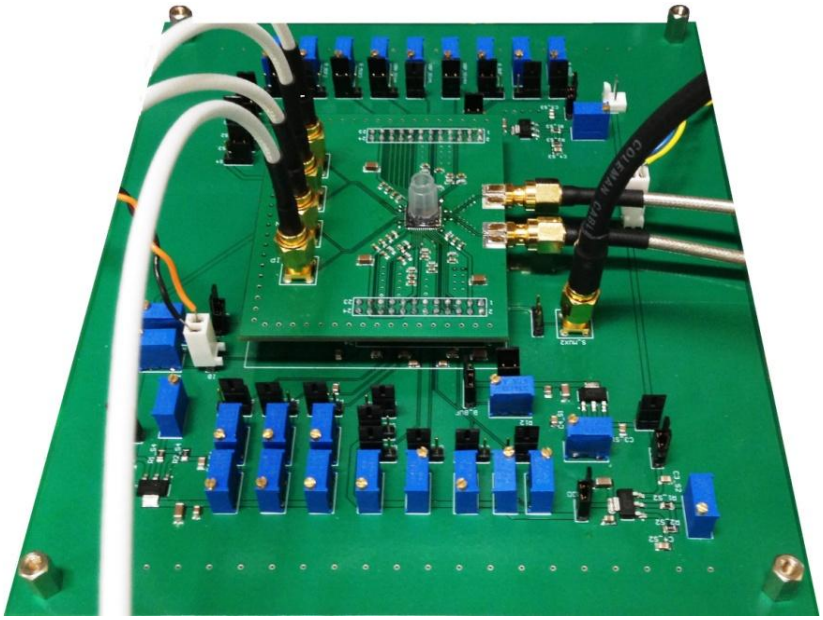

Fig. 2.19: Photograph of the PCB.

using the micropipette and then compressed gas dusters are utilized to completely dry the tube and clean the sensor from any material residue, preparing the system for the next MUT sensing.

The sensor chip in Fig. 2.18(c) is mounted on a printed circuit board (PCB) as shown in Fig. 2.19. The two differential output of the system (i.e. V_I and V_Q) are applied to off-chip LPFs to further filter out the high frequency noise and improve system sensitivity. Before calculating V_A/V_B using (2.4), a simple calibration procedure is utilized to cancel out dc offsets at the system outputs, as discussed in Section 2.2.2. Note that since the output dc offsets are frequency-dependent, they must be measured separately at each frequency.

As a proof of concept, organic chemical liquids including methanol, ethanol, propan-1-ol, butan-1-ol, ethyl acetate, xylene, ethanediol and dimethyl sulfoxide (DMSO) are applied to the sensor for characterization. The measured dc voltages at

the output of I and Q channels after dc offset cancellation are substituted into (2.4) to find V_A/V_B. From (2.3), V_A/V_B is proportional to the sensor admittance at any certain frequency. Fig. 2.20 shows the calculated real and imaginary parts of V_A/V_B based on the measured I and Q outputs as a function of ε' and ε'', respectively for the sensing frequencies of 1 GHz and 8 GHz. The ε' and ε'' values in this plot are extracted from the reported dispersion equations and parameters in [2, 3]. It is clear that the integrated BDS system successfully differentiates among all the MUTs. Interestingly, although ε' and ε'' values of xylene and air are very similar ($\varepsilon'_{xylene} \approx 2$ and $\varepsilon''_{xylene} \approx 0$), the system is still capable of discriminating between the two MUTs. The dashed line in each plot in Fig. 2.20 corresponds to the best fitted linear curve to the measured data. It is seen that the real (imaginary) part of V_A/V_B shows an approximately linear behavior with respect to ε' (ε'') at each frequency, which was predictable from (2.5), thereby, verifying the overall system functionality.

2.5.2 Sensor Calibration

In order to relate the measured V_A/V_B to the complex permittivity of the MUT, the sensor needs to be first calibrated. The sensor calibration must be performed separately at each sensing frequency. This is because of the fact that the admittance of the unloaded sensing capacitor and also the input impedance of the LNA are frequency-dependent, which means that even for an MUT with fixed permittivity over all frequencies, the measured V_A/V_B will vary with frequency. The calibration procedure is based on fitting the output response of the sensor (i.e. V_A/V_B characteristics) as a function of the complex permittivity of reference materials which are assumed to be known based on the previously reported numbers in [2, 3]. Air, methanol, ethanediol, butan-1-ol and DMSO are chosen as calibration materials because they cover a broad range of ε' and ε'' values in the desired frequency range, as

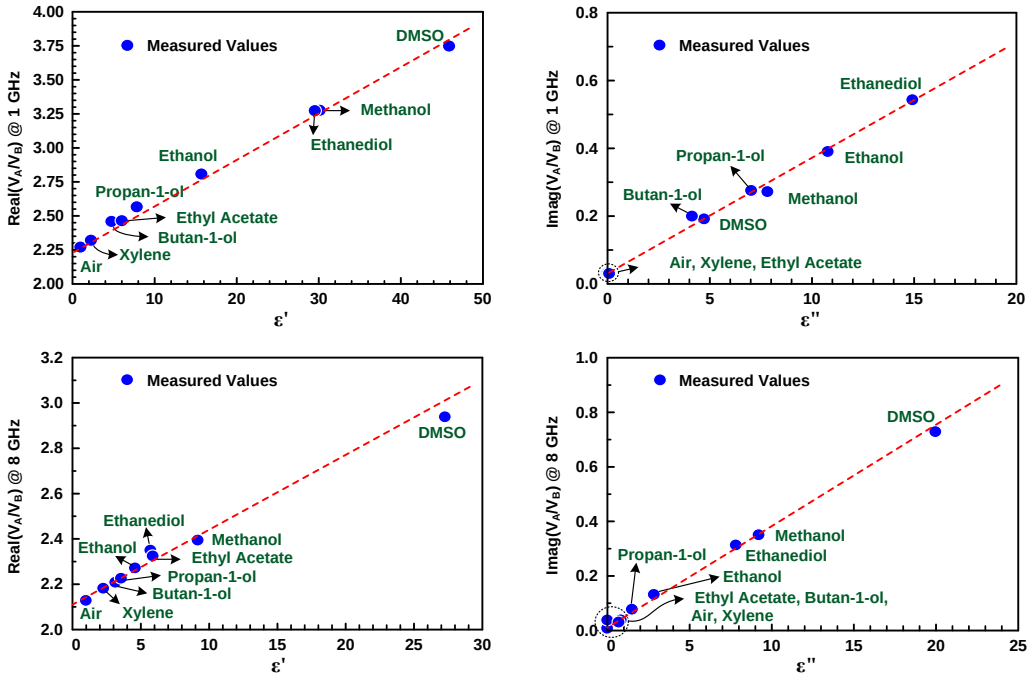

Fig. 2.20: Measured real and imaginary parts of V_A/V_B as a function of ε' and ε'', respectively at 1 and 8 GHz.

can be seen in Fig. 2.20. To perform calibration at f_s, the sensor is first loaded with each calibration material and I and Q outputs are read out. These values are then substituted in (2.4) to find the corresponding V_A/V_B for each calibration material at f_s. In the next step, the calculated real and imaginary parts of V_A/V_B for the reference liquids are least-square fitted to quadratic polynomial functions of ε' and ε'', respectively, using the following equations:

$$\mathrm{Re}\,(V_A/V_B) = \alpha_1 \varepsilon'^2 + \alpha_2 \varepsilon' + \alpha_3. \tag{2.26}$$

$$\mathrm{Im}\,(V_A/V_B) = \alpha_4 \varepsilon''^2 + \alpha_5 \varepsilon'' + \alpha_6. \tag{2.27}$$

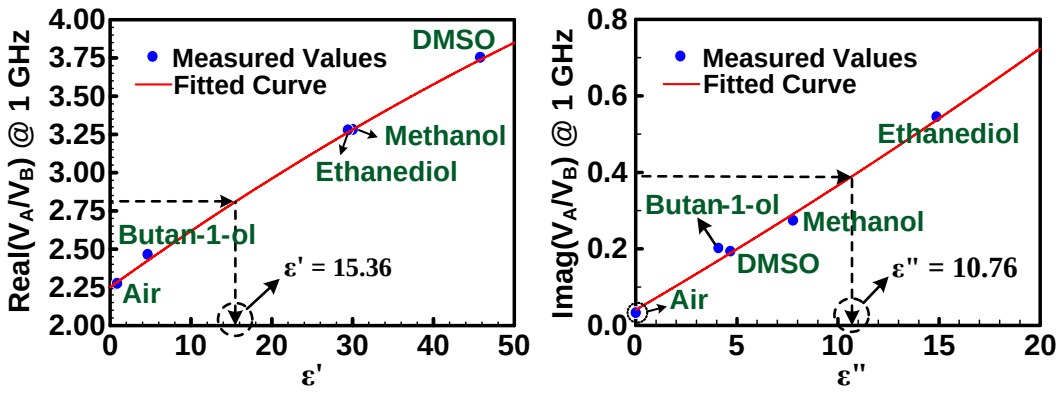

Fig. 2.21: Measured real and imaginary parts of V_A/V_B for the reference material as a function of ε' and ε'', respectively at 1 GHz, along with the quadratic polynomial fitted curve.

where α_i, $1 \leq i \leq 6$ are the frequency-dependent fit parameters. Although only three materials with known ε' and ε'' values are sufficient to determine α_i values in (2.26) and (2.27), using more reference materials and employing least-squares fitting method help minimizing the errors that might encounter in sensing process of these liquids. After finding the fit parameters, the complex permittivity of an unknown MUT at f_s can be detected by substituting the measured real and imaginary parts of V_A/V_B for that material in (2.26) and (2.27). As an example, the detection procedure for the permittivity of ethanol at 1 GHz is performed as follows: 1) The measured values of $\mathrm{Re}(V_A/V_B)$ and $\mathrm{Im}(V_A/V_B)$ for reference materials are least-squares fitted to a quadratic functions of ε' and ε'', respectively, as illustrated in Fig. 2.21. The characteristic equations are given by

$$\mathrm{Re}\,(V_A/V_B) = -0.00012\varepsilon'^2 + 0.0382\varepsilon' + 2.251. \tag{2.28}$$

$$\mathrm{Im}\,(V_A/V_B) = 0.0002\varepsilon''^2 + 0.0302\varepsilon'' + 0.042. \tag{2.29}$$

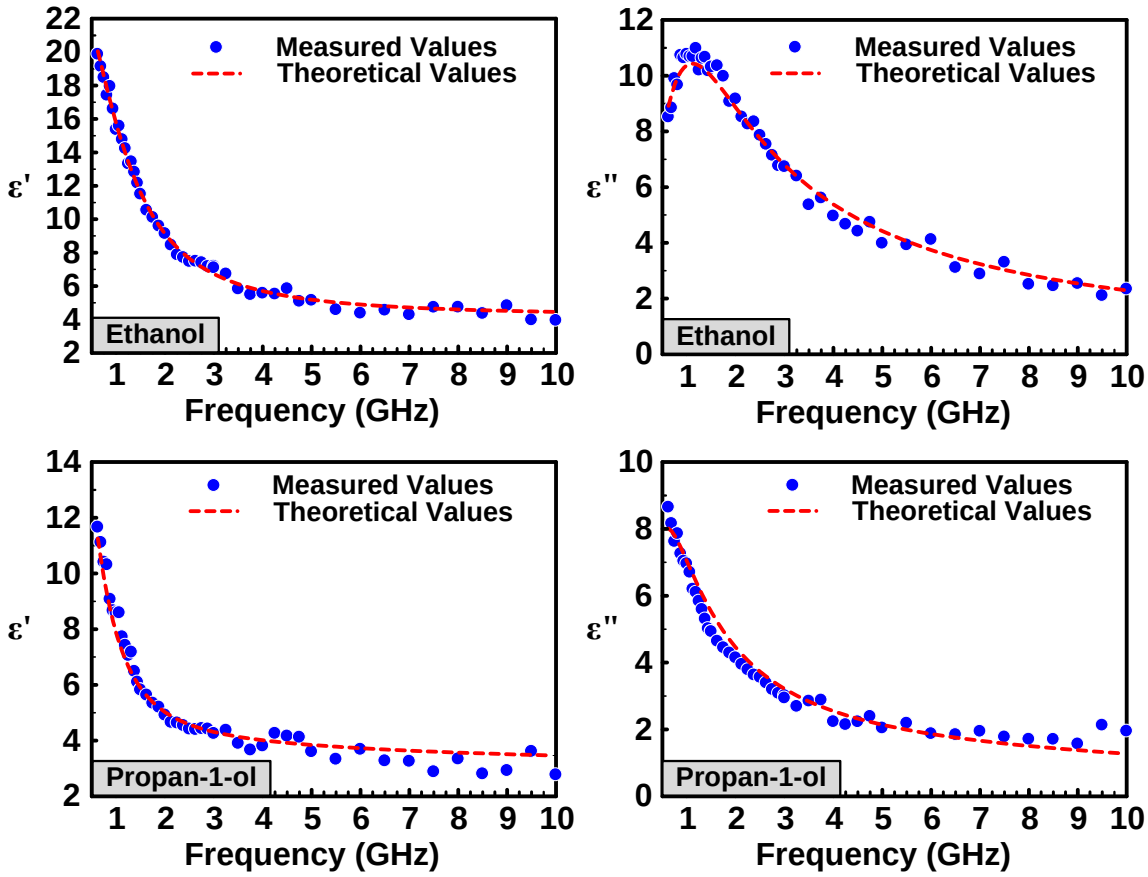

Fig. 2.22: Measured permittivities versus frequency for ethanol and propan-1-ol. The results are compared with theoretical values from [2, 3].

2) The values of $\mathrm{Re}(V_A/V_B)$ and $\mathrm{Im}(V_A/V_B)$ when the sensor is exposed to ethanol are measured to be 2.81 and 0.39, respectively; and 3) The detected values in step 2 are mapped to an ε' of 15.36 and ε'' of 10.76 using the characteristic equations which are very close to the theoretical values of 15.73 and 10.38, respectively. Fig. 2.22 shows the measured complex permittivity of ethanol and propan-1-ol following the above procedure for the sensing frequencies in the range of 0.625-10 GHz. As can be seen, the detected complex permittivities are in very good agreement with the theoretical values. The rms permittivity error of the sensor is less than 1% over the entire

operating range. The increase in the absolute error at higher frequencies, especially in SB3 and SB4, is mainly because of two reasons; 1) as discussed in Section 2.4.6, the system has inferior noise performance at these frequency bands, and 2) although considering real and imaginary parts of V_A/V_B as functions of only ε' and ε'' results in a simple calibration procedure for the sensor and makes it possible to detect ε' and ε'' independently, it degrades the system accuracy at high frequencies where the sensor admittance becomes a function of both ε' and ε'' (Section 2.1.1).

Table 2.4 summarizes the specifications of the sensor and compares it with the prior published works. In contrast to the PLL-based sensing systems in [23, 24], the proposed sensor covers a wider frequency range. Also, compared to the design in [25], this work achieves a higher level of integration by incorporating an on-chip sensing capacitor. Moreover, both of the designs in [25] and [26] employ a heterodyne downconversion architecture and thereby need two separate signal sources for the input RF excitation signal and the high frequency LO of mixer with a frequency span equal to the desired sensing range. In contrast, by employing a sub-harmonic mixing technique, this work only needs a signal source with a frequency span of 5-10 GHz to cover the 0.625-10 GHz sensing range. Note that the required RF input signal can be easily generated using an on-chip frequency synthesizer, enabling a fully-integrated self-sustained broadband dielectric spectroscopy system.

2.6 Summary

An integrated complex dielectric spectroscopy system was presented using O.l8μm CMOS technology for characterization of chemicals and bio-materials. The sensor achieves an rms permittivity measurement error of less than 1% over the entire O.62-10 GHz operating range.

Table 2.4: Performance Summary and Comparison to Reported Integrated Dielectric Sensors.

	[23]	[24]	[25]	[26]	This Work
CMOS Process	90 nm	90 nm	0.35 μm	65 nm	0.18 μm
Operating Freq.	7-9 GHz	10.4 GHz	0.05-3 GHz	1-50 GHz	0.62-10 GHz
Detection Capability	only ε'	only ε'	only ε'	ε' and ε''	ε' and ε''
Required Freq. Range of the Input Signal Source	Self-sustained	Self-sustained	RF: 0.05-3 GHz LO: 0.05-3 GHz $\lvert f_{RF} - f_{LO} \rvert = 1$ MHz	RF: 1-50 GHz LO: 1-50 GHz $\lvert f_{RF} - f_{LO} \rvert = 100$ MHz	5-10 GHz
Sensing Element	Interdigitated capacitor	Interdigitated capacitor	off-chip center-gapped μstrip line	CPW transmission-line	Interdigitated capacitor
Permittivity error	$< 3.5\%$	$< 1.5\%$	$< 1\%$ (0.05-2 GHz)	$< 1\%$ @ 20 GHz	rms error $< 1\%$
Power	16.5 mW	22 mW	4-9 mW	114 mW	65-72 mW
Area	6.25 mm^2	2.15 mm^2	9 mm^2	1.2 mm^2	9 mm^2

3. A 5.12-12.95 GHZ TRIPLE-RESONANCE LOW PHASE NOISE CMOS VCO*

As discussed in the first section, a single-tank LC VCO relying on only switched capacitor technique can hardly achieve tuning range above 40% while satisfying moderate phase noise requirements. In order to achieve wider tunning range, multiple VCOs can be employed. However, this technique requires large silicon area and therefore increases the cost. Other techniques have been reported to widen the oscillator tuning range including VCOs exploiting switched inductors [36] and coupled inductors [37–40]. The VCOs based on switched inductors suffer from poor phase noise performance due to the loss of the switches inside the tank. On the other hand, in the VCOs with coupled inductors, the multi-oscillation modes of the resonator are employed to make a multi-band oscillator without using lossy switches to achieve better phase noise performance and more compact layout.

In a dual-band VCO with a 4th-order resonator (two coupled LC tanks) in [37], to cover one octave of frequency range, the required tuning range in each band needs to be 40-50%. However, such a tuning range is still very difficult to achieve, especially at higher frequencies because of the trade-offs between phase noise, tuning range and power dissipation. In this work, another oscillation mode is added to a 4th-order resonator by properly placing an inductor between the two coils of the transformer to realize a triple-band VCO. This extra mode is employed to alleviate the aforementioned trade-offs and to improve the phase noise performance by reducing the required capacitance variations in each band. The modified resonator still maintains two potential resonant modes at each port. This property results in a

*

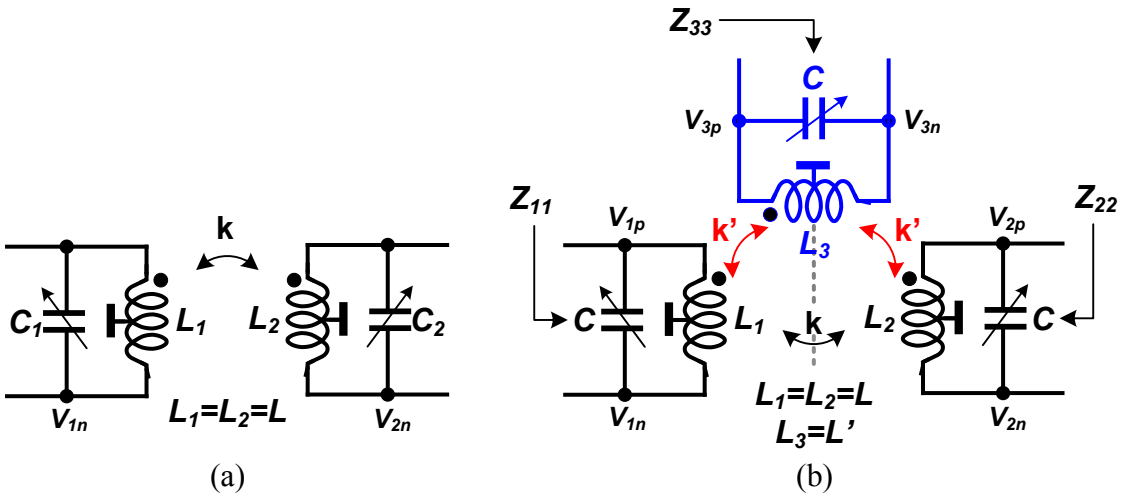

Fig. 3.1: (a) A dual-mode resonator, and (b) the proposed resonator.

simple method of switching between the three resonance frequencies which is robust to process, voltage and temperature (PVT) variations.

3.1 VCO Architecture

3.1.1 Proposed Resonator

Fig. 3.1(a) shows a dual-mode resonator composed of two magnetically coupled LC tanks. For this structure, assuming $L_1 = L_2 = L$ and $C_1 = C_2 = C$, the two oscillation frequencies can be found as [39]

$$\omega_{even}^2 = \frac{\omega_o^2}{1+k}, \qquad \omega_{odd}^2 = \frac{\omega_o^2}{1-k} \tag{3.1}$$

where $\omega_o = 1/\sqrt{LC}$ is the resonance frequency of the un-coupled tanks. In an attempt to add one more oscillation mode to this structure, another inductor (L_3) is placed at the line of symmetry where it has the same mutual coupling to L_1 and L_2 (Fig. 3.1(b)). The value of L_3 (L') is chosen such that together with C it has an individual resonance frequency of $\omega_o' = 1/\sqrt{L'C}$ higher than ω_{odd}. As will be shown,

the new resonator provides three resonant modes while only two of them appear at each port.

Assuming high-Q components, the input impedance at each port of the resonator can be derived as

$$Z_{11}(s) = Z_{22}(s) = \frac{N(s)}{D(s)}, \qquad Z_{33}(s) = \frac{N'(s)}{D(s)} \tag{3.2}$$

where

$$\begin{aligned}
N(s) &= \frac{s}{C}\left[(1-k)\left(1+k-2k'^2\right)s^4 + \left(\omega_o^2\left(1-k'^2\right) + \omega_o'^2\left(1-k^2\right)\right)s^2 + \omega_o^2\omega_o'^2\right], \\
N'(s) &= \frac{s}{C}\left[(1-k)\,s^2 + \omega_o^2\right]\left[\left(1+k-2k'^2\right)s^2 + \omega_o^2\right], \\
D(s) &= \left[(1-k)\,s^2 + \omega_o^2\right]\left[\left(1+k-2k'^2\right)s^4 + \left(\omega_o^2 + \omega_o'^2\,(1+k)\right)s^2 + \omega_o^2\omega_o'^2\right]. \qquad (3.3)
\end{aligned}$$

Therefore, the resonator has three possible oscillation frequencies. The roots of the first term in $D(s)$ determine the middle-frequency resonance (ω_M) of the system while the roots of the last term correspond to the lower and higher-frequency resonances (ω_L and ω_H).

Interestingly, ω_M is equal to ω_{odd} which implies that the addition of L_3 does not affect the operation of the 4th-order resonator in its odd mode. Moreover, one of the notch frequencies in Z_{33} is located exactly at ω_M, hence, looking into port-3, the system potentially has only two resonance frequencies at ω_L and ω_H. Similarly, it can be easily shown that the high frequency notch of Z_{11} (Z_{22}) in (3.3) is located at a frequency very close to ω_H so by looking into port-1 (port-2), effectively two possible oscillation frequencies at ω_L and ω_M can be seen (Fig. 3.2(a)). Fig. 3.2(b) shows the ratio between ω_H and the high frequency notch in Z_{11} for different values of k, k and ζ where ζ is the ratio between the resonance frequencies of un-coupled

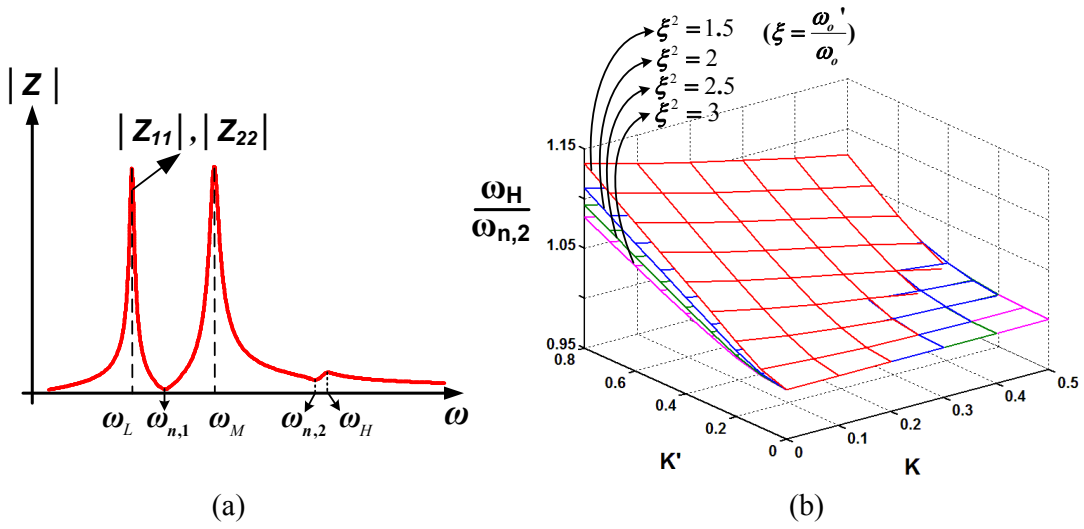

Fig. 3.2: (a) Magnitude of Z_{11} and Z_{22} , and (b) ratio between ω_H and the high frequency notch in Z_{11} for different values of k, k' and ζ.

tanks ($\zeta = \omega_o'/\omega_o$). As it is clear, the ratio between these two frequencies is always close to one such that no oscillation can occur at ω_H.

These results could be also deduced in an intuitive way. As an example, when the resonator is working at ω_M, the currents flowing through L_1 and L_2 have the same amplitude and are 180° out of phase. As a result, since $k_{13} = k_{23} = k'$, the two induced currents in L_3 will cancel out each other and it is like that this inductor does not exist in the system (see Fig. 3.3). Consequently, the resonance frequency of this mode (ω_M) will be equal to ω_{odd} and looking into port-3, no oscillation can occur at ω_M.

Based on the same analysis, only two dominant resonance peaks exist in the amplitude responses of Z_{12}, Z_{13} and Z_{23}. The peak frequencies of Z_{12} are located at ω_L and ω_M while the peaks of Z_{13} and Z_{23} are at ω_L and ω_H.

In summary, by placing an LC tank at the line of symmetry of a 4th-order resonator, another resonant mode is added to the system. However, this extra mode can

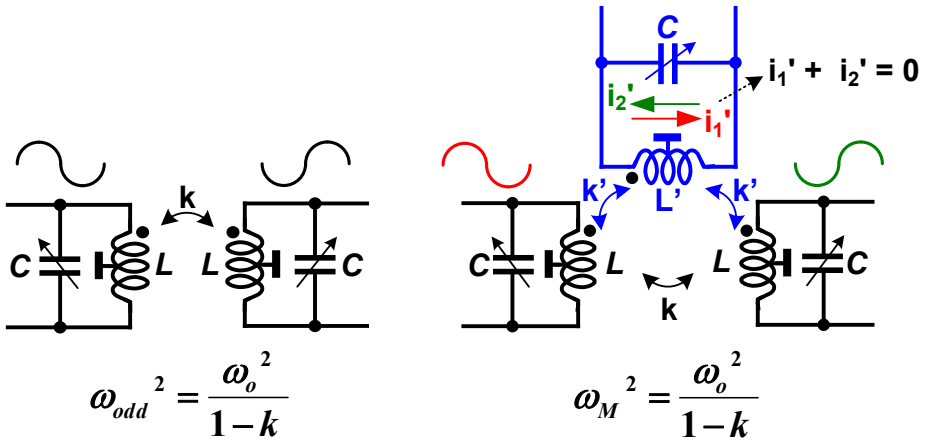

Fig. 3.3: Illustration of why $\omega_M = \omega_{odd}$ for the proposed resonator.

be only seen at port-3 and looking into port-1 and port-2, the resonator still maintains its dual-mode operation. This property of the resonator results in a simple and yet robust method for selecting the desired mode of oscillation.

3.1.2 Mode Switching

Fig. 3.4 shows the detailed schematic of the proposed triple-band VCO. The G_m-cells in this figure are employed to excite the desired mode of operation.

As shown in Fig. 3.5(a), there are only two dominant peaks in the amplitude response of Z_{12} located at ω_L and ω_M. Furthermore, the phase shift of Z_{12} is 0° at ω_L while it becomes -180° at ω_M. As a result, by placing a sufficiently positive or negative transconductance between L_1 and L_2, the oscillation condition at either ω_L or ω_M can be satisfied, respectively. Consequently, as illustrated in Fig. 3.4, to make the oscillator work at $\omega_L(\omega_M)$, $G_{m12}(G_{m21})$ is turned on while the other G_m-cells are remained off. Moreover, in order to ensure the start-up of the oscillation, the values of G_{m12} and G_{m21} must satisfy the following conditions

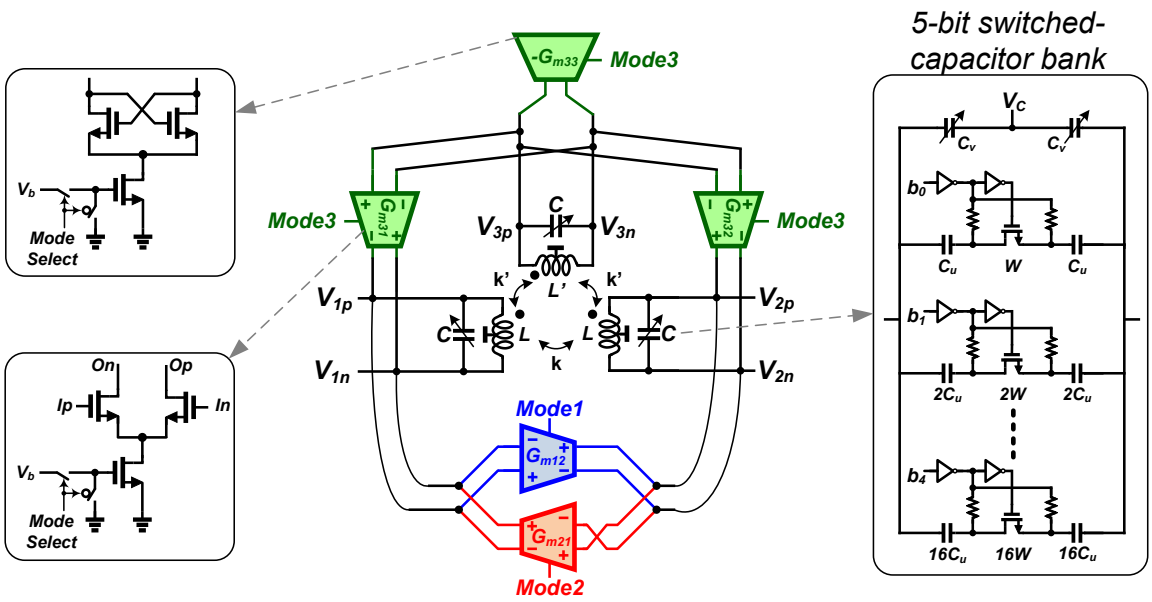

Fig. 3.4: Detailed schematic of the triple-mode VCO (modes 1, 2 and 3 correspond to oscillation frequencies at ω_L, ω_M and ω_H, respectively).

$$G_{m12} > \frac{1}{|Z_{12}|}\bigg|_{\omega=\omega_L}, \qquad G_{m21} > \frac{1}{|Z_{21}|}\bigg|_{\omega=\omega_M} \tag{3.4}$$

Looking into port-3, the system can oscillate at either ω_L or ω_H. However, the amplitude of Z_{33} at these frequencies highly depends on the coupling factors k and k'. The values of k and k' cannot be chosen independently. For example, if the inductors L_1 and L_2 are located closer to L_3 to increase k', the value of k would also be increased. Fig. 3(b) illustrates the amplitude of Z_{33} for different values of k and k' (the other resonator parameters are kept constant). By decreasing the coupling between the inductors, the separation of the two resonance peaks decreases and the amplitude of Z_{33} becomes more dominant at ω_H. As a result, by properly setting the negative conductance G_{m33} in Fig. 3.4, one can make the oscillator work at ω_H. For a sufficiently large value of G_{m33}, the high-loss mode at ω_L can be also stimulated resulting in simultaneous oscillation at both frequencies. In order to avoid such a

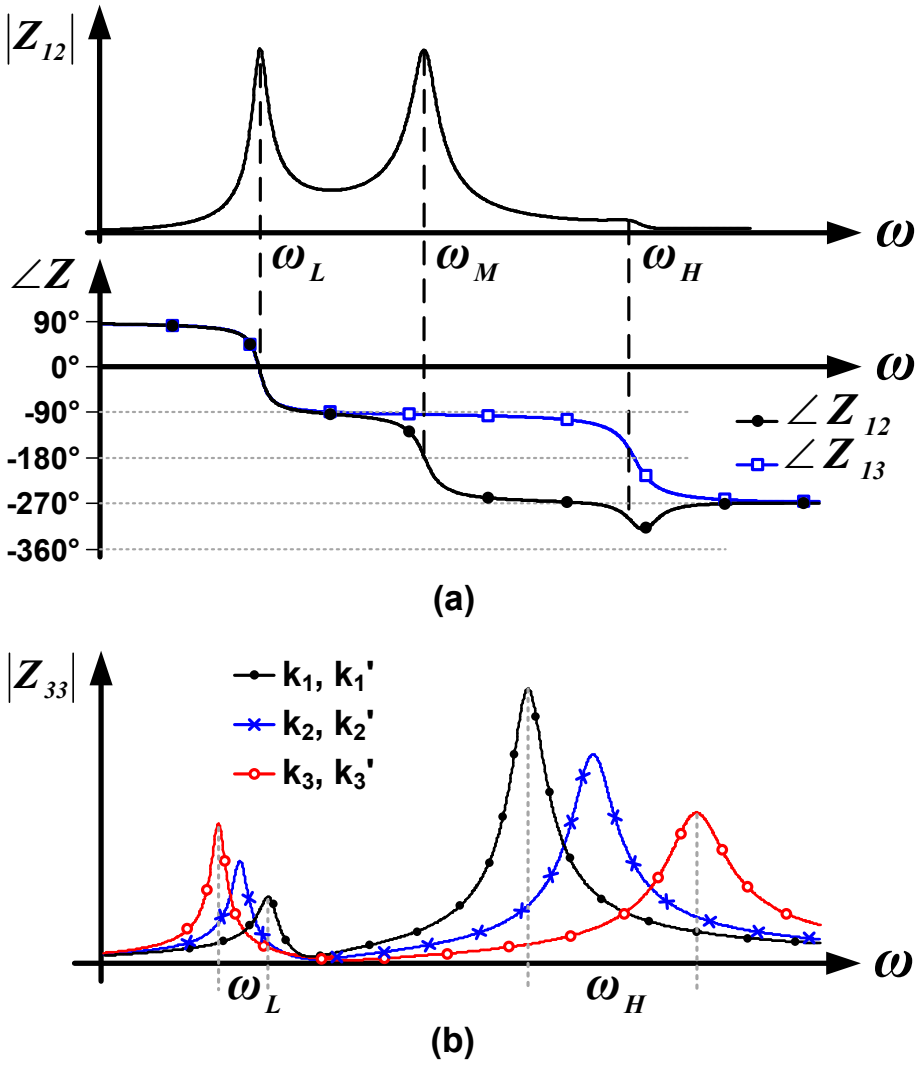

Fig. 3.5: (a) $|Z_{12}|$ and $\angle Z_{12}$, $\angle Z_{13}$ vs. frequency, and (b) $|Z_{33}|$ vs. frequency for different values of k and k' ($k_1 < k_2 < k_3$, $k_1' < k_2' < k_3'$).

behavior, G_{m33} must be chosen such that

$$G_{m33} < \frac{1}{|Z_{33}|}\bigg|_{\omega=\omega_L}, \quad \textit{and} \quad G_{m33} > \frac{1}{|Z_{33}|}\bigg|_{\omega=\omega_H} \tag{3.5}$$

On the other hand, for large values of k and k', the lower-frequency peak of Z_{33}

becomes comparable to its peak at ω_H, hence, the use of only $-G_{m33}$ would result in unstable or even concurrent dual-mode oscillation. However, as previously discussed, the impedance Z_{13} has the same resonance peaks as Z_{33}. Also, the phase response of Z_{33} in Fig. 3.5(a) shows phase shift of 0° and -180° at ω_L and ω_H, respectively. Thus, by adding two negative transconductances like G_{m31} and G_{m32} in Fig. 3.4, one can satisfy the oscillation conditions at only ω_H.

Although strongly-coupled inductors are more desirable in terms of chip area, the amplitude of Z_{33} drops for larger values of k and k' (Fig. 3.5(b)). Thus, the VCO needs to consume more power to achieve the same phase noise performance. In the implemented prototype, to achieve an approximately balanced performance in the three modes, the values of k and k' were chosen to be 0.2 and 0.35, respectively. For the designed resonator, simulations verify that the amplitude of Z_{33} is around 10 dB larger at ω_H compared to its amplitude at ω_L which was found sufficient to ensure the operation of VCO by using only $-G_{m33}$ even in the presence of worst case PVT variations.

3.1.3 Circuit Implementation

As depicted in Fig. 3.4, the cross-coupled NMOS transistors are used for $-G_{m33}$ while the other G_m-cells are implemented using NMOS differential pairs. A low supply voltage of 1-V was chosen to minimize the voltage stress on transistors. In this way, minimum-length transistors can be used in each G_m-cell which results in less parasitic capacacitance at the outputs of LC tanks. Both coarse and fine tuning are adopted to cover the required frequency range in each mode and to achieve a low VCO gain (K_{VCO}). A Low K_{VCO} reduces AM-PM noise conversion and therefore leads to a better phase noise performance. The coarse frequency tuning is achieved by a 5-bit binary-weighted switched-capacitor bank while the fine tuning is accomplished

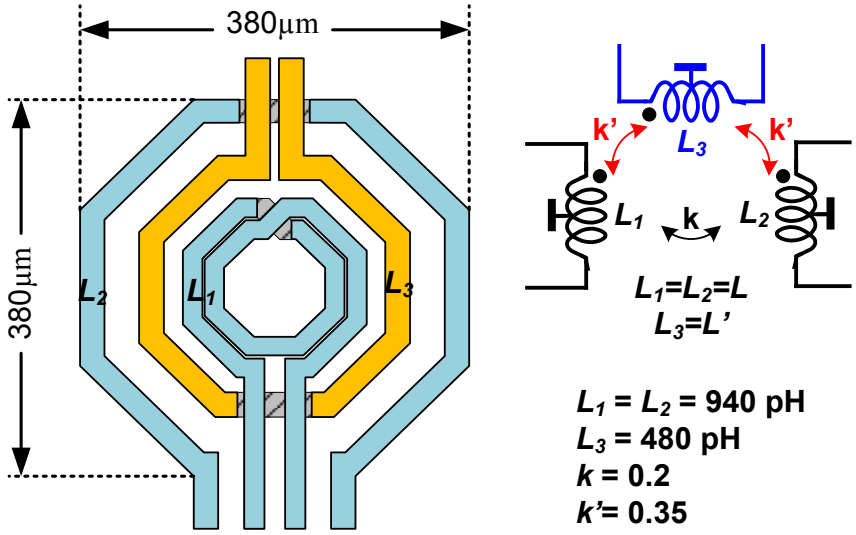

Fig. 3.6: Layout of coupled inductors.

by small NMOS varactors. The MOS switches are controlled through a 0/1.8 V bias and the VCO control voltage (V_C) is tuned from 0 to 1.8 V.

The inductive part of the resonator is designed using Sonnet EM simulator. To make $k_{13} = k_{23}$, inductor L_3 is placed between the other two coils (Fig. 3.6). All inductors are implemented using the top metal layer (M6) in the 0.18 μm CMOS process with a thickness of 2 μm.

3.2 Fabrication and Measurement Results

The VCO was fabricated in an IBM 0.18 μm CMOS technology with 6 metal layers. A die photo of the chip is shown in Fig. 3.7. The chip area is 1.3 mm$\times$1.5 mm with an active core area of 0.33 mm^2. The prototype was tested using a GSGSG RF probe and the measurements were conducted with an Agilent E4446A spectrum analyzer.

Fig. 3.8 shows the measured frequency tuning range of the VCO where $b < 4 : 0 >$

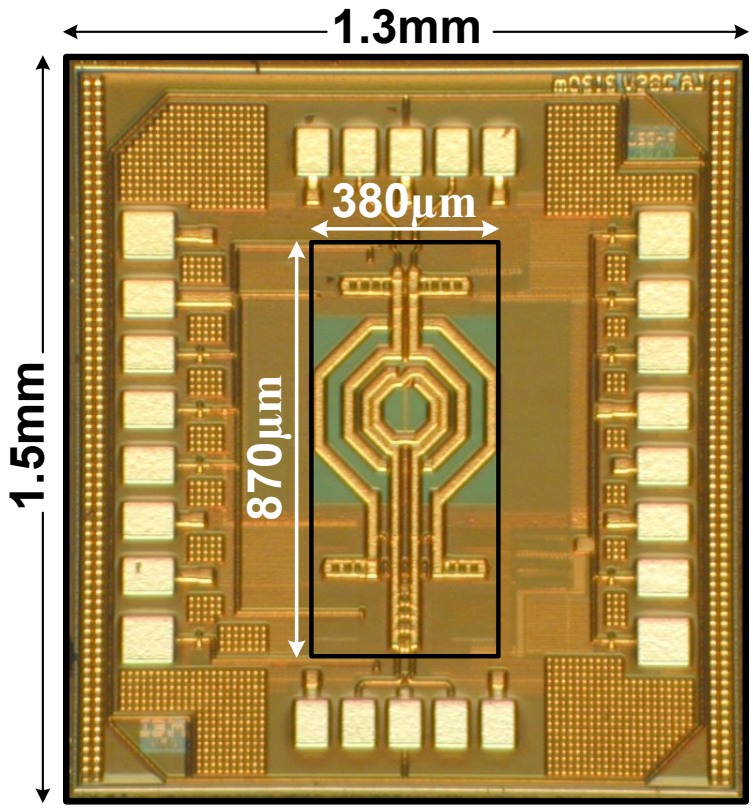

Fig. 3.7: Die photo of the triple-band VCO.

is the 5-bit control word of the switched-capacitor bank. The VCO is continuously tunable for 5.12-12.95 GHz. Also, there is significant overlap between consecutive modes which ensures the operation of VCO at the presence of PVT variations.

Fig. 3.9 shows the measured phase noise at 1 MHz offset frequency throughout the tuning range. Fig. 3.10 shows a sample of measured phase noise curve at 9.12 GHz. The current consumption of the VCO for different modes and across the tuning range has been shown in Fig. 3.11. With reducing frequency in each mode, the tank impedance magnitude drops and hence more current is needed to push the oscillator into the voltage-limited regime. Table 3.1 compares this work with recently published wide-tuning range VCOs. The proposed VCO achieves excellent phase

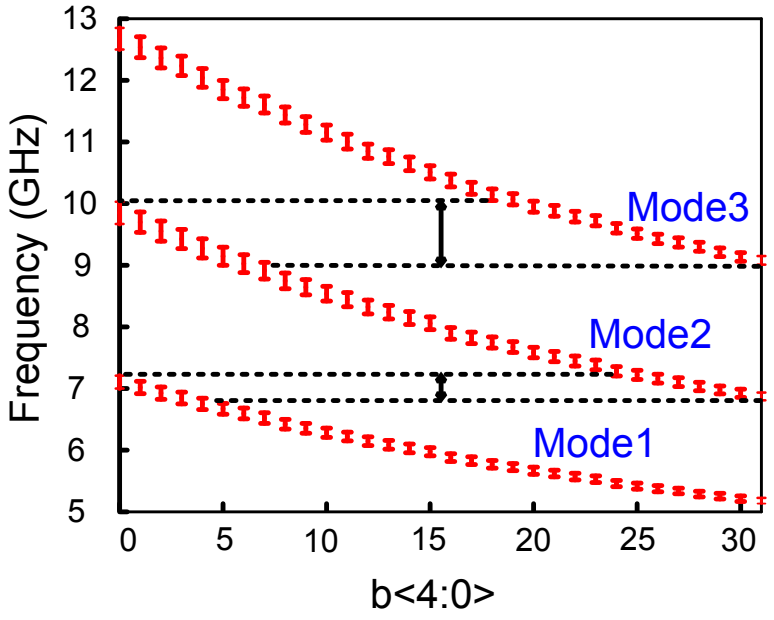

Fig. 3.8: Measured VCO tuning range.

noise performance as well as competitive FoM compared with the other state-of-the-art designs.

3.3 Summary

A low-phase-noise triple-band VCO is presented for based on a resonator with three possible oscillation frequencies. Implemented in 0.18 μm CMOS technology, the VCO prototype covers a frequency range of 5.12-12.95 GHz and achieves excellent phase noise performance across the whole band.

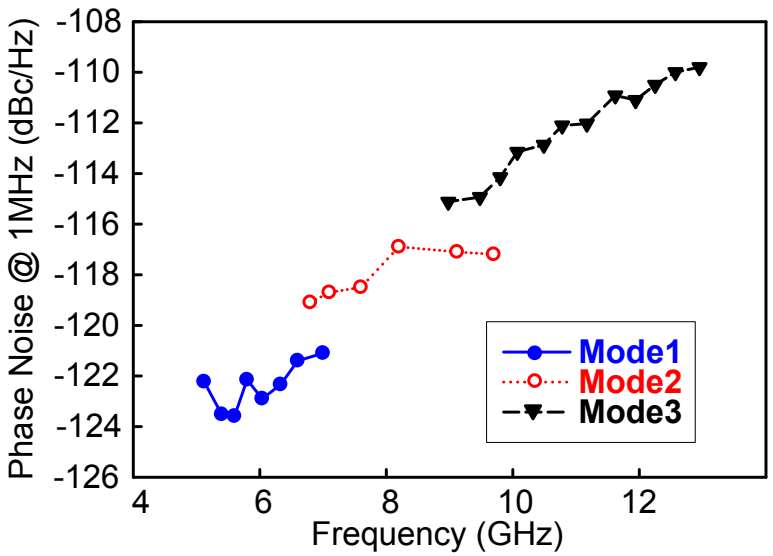

Fig. 3.9: Measured phase noise at 1 MHz offset frequency.

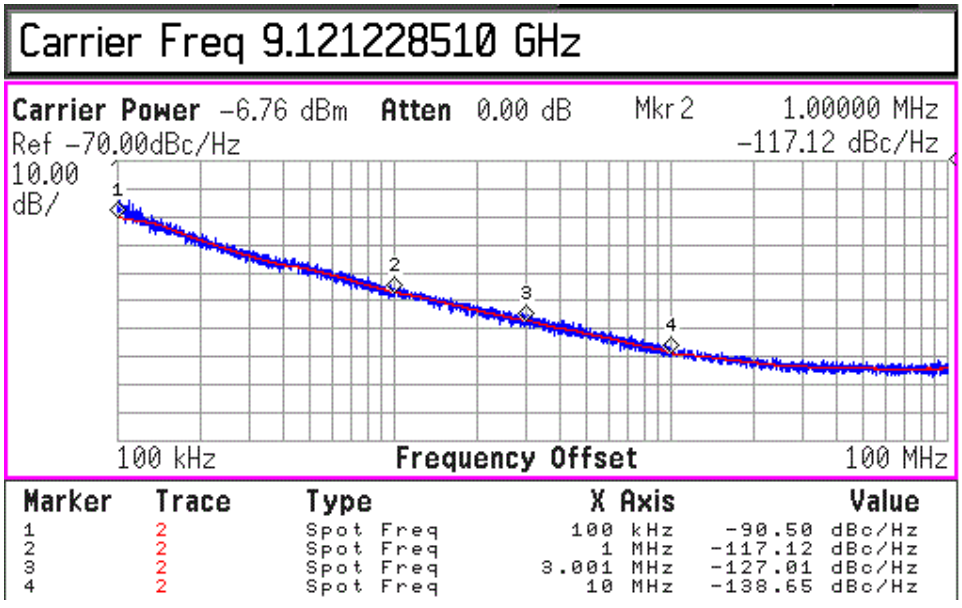

Fig. 3.10: Measured phase noise at 9.12 GHz

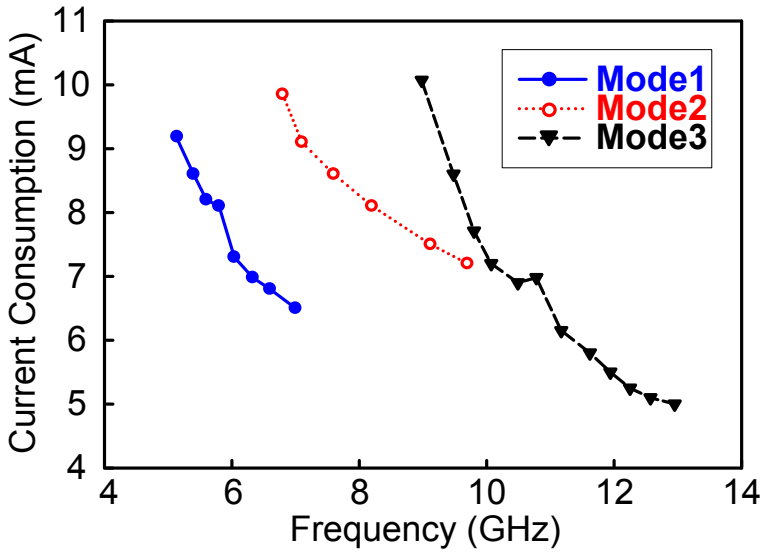

Fig. 3.11: VCO Current consumption across the tuning range.

Table 3.1: Comparison with Recently Published Multi-Band VCOs

	Type	Process	V_{DD} (V)	Power (mW)	Freq. (GHz)	Tuning Range	PN (dBc/Hz) @1MHz	FoM[2] (dB)	Area (mm^2)
Borremans, ISSCC 2008	Dual-Band	90nm CMOS	1.2	2.2~4.2 /6.7~10	3.1~3.9	23%	-122 @ 2.5MHz	181	0.034
					8.8~11.2	24%	-117 @ 2.5MHz	181.2	
Li, JSSC 2012	Dual-Band	65nm CMOS	0.6	9.8~14.2	2.48~3.93	77.5%	-128.3	189.5	0.294
					3.31~5.62		-124.8	186.8	
Safarian, TCAS I, 2009	Triple-Band	0.13µm CMOS	1.5	4.35~9.15	1.28~2.27	130.2%	-120	177.4	1[1]
					2.34~4.03		-119	181	
					3.65~6.06		-117	181.5	
This Work	Triple-Band	0.18µm CMOS	1	5~10	5.12~7.21	86.7%	-122.9	189.7	0.33
					6.8~10.03		-117	187.5	
					9~12.95		-112	185	

[1] Area including pads

[2] $FoM = 10\log_{10}\left[\frac{1}{P_{diss|mW}}\left(\frac{f_o}{\Delta f}\right)^2 - L(\Delta f)\right]$

4. A LOW-PHASE-NOISE WIDE-TUNING-RANGE QUADRATURE OSCILLATOR USING A TRANSFORMER-BASED DUAL-RESONANCE LC-RING*

4.1 Introduction

In-phase and quadrature-phase (I/Q) signal generation is an essential task in various RF transceivers for orthogonal down-conversion and up-conversion. Several different techniques can be employed to generate I/Q signals. In the most commonly used approach, a voltage-controlled oscillator working at twice the desired frequency is followed by a flip-flop based divide-by-two circuit to generate quadrature phases. In another technique, a QVCO directly produces I/Q signals without the need for doubling the frequency.

Fig. 4.1(a) shows the topology of the conventional QVCO made of two transistor-coupled LC oscillators [41]. There are several drawbacks with this architecture which restrict its use in many applications. To gain some insight into the limitations of this topology, the phasor diagram of the tank voltages and currents is shown in Fig. 4.1(b). As can be seen, the total current flowing through the tank (I_{tank}) is the result of summation of two orthogonal phasors $I_m = G_m V_I$ and $I_c = G_{mc} V_Q$, thereby, I_{tank} shows a phase shift of $\theta = \tan^{-1}(I_c/I_m)$ with respect to tank voltage.

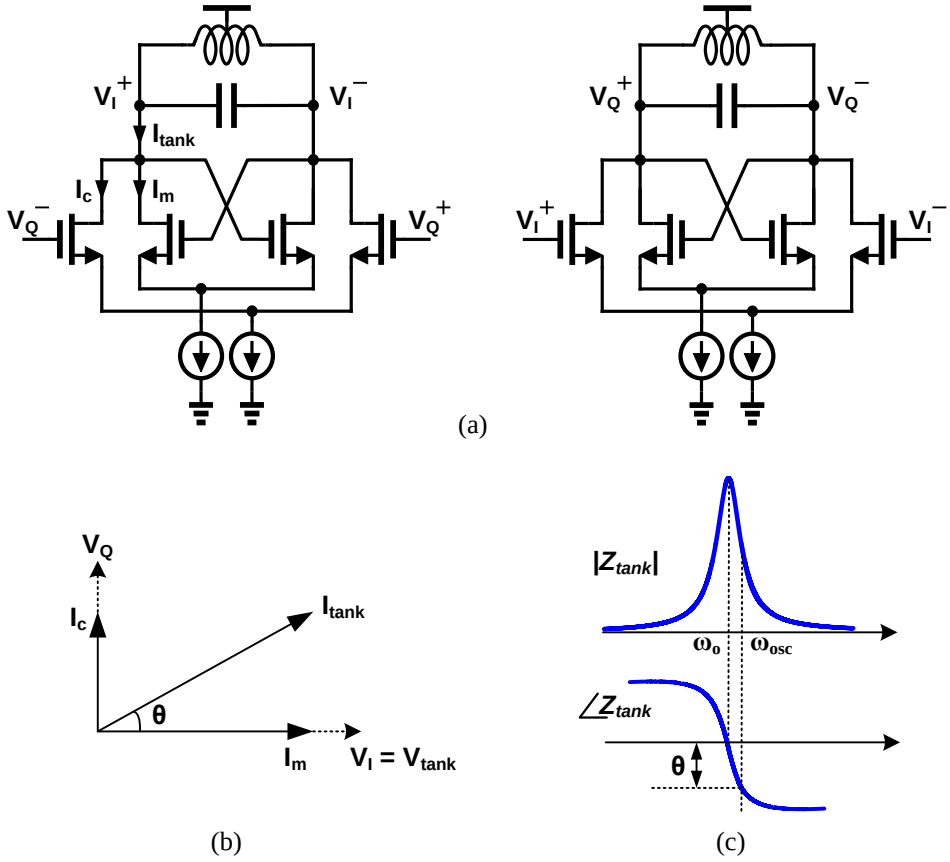

Fig. 4.1: (a) Schematic of the conventional QVCO, (b) phasor diagram, (c) amplitude and phase of the tank impedance.

As illustrated in Fig. 4.1(c), in order to provide this phase rotation, the oscillator needs to operate off-resonance. By equating the phase response of the tank near resonance to θ, the oscillation frequency can be found as [42]

$$\omega_{osc} = \omega_o \left(1 \pm \Delta\omega\right) \approx \omega_o \left(1 \pm \frac{1}{2Q_{tank}} \frac{I_c}{I_m}\right). \tag{4.1}$$

where $\omega_o = 1/\sqrt{LC}$ and Q_{tank} is the tank quality factor.

The above equation explains the main issues encountered with the QVCO architecture in Fig. 4.1(a) as will be discussed in the following. First, there are two

possible oscillation frequencies depending on if there is $+90^\circ$ or -90° phase shift between the outputs of two VCOs. This bimodal oscillation property has been proven to be problematic in reality [43] and several techniques have been proposed to avoid this behavior [43–45]. Second, while coupling transistors provide no loss compensation, they cause the LC tank to work away from the resonance where quality factor is lower than the optimal value, thus, deteriorating the phase noise performance [46]. Also, since the oscillation frequency becomes a function of coupling strength ($=I_c/I_m$) between two VCOs, flicker noise in currents I_m and I_c directly modulates ω_{osc} and translates into phase noise [47–49]. Due to these reasons, the phase noise performance of conventional QVCOs is typically 5 to 10 dB inferior to their single-tank counterparts. Third, while small coupling factor is more desirable for low phase noise and low power consumption, it makes the QVCO more susceptible to unavoidable component mismatches, thereby, degrading the quadrature phase accuracy [50]. Therefore, there is a strong trade-off between phase noise, power consumption and phase accuracy.

A number of QVCO topologies have been proposed in literature to alleviate the aforementioned issues [26, 51–59]. From the above discussion it can be concluded that if the coupling of LC tanks could be accomplished through passive devices instead of noisy transistors, then the phase noise performance would be substantially improved. Considering this fact, several QVCOs using passive-coupling have been previously proposed to reduce the phase noise or phase error. For instance, [58] couples two differential oscillators through capacitors to completely eliminate noise from the coupling transistors. As has been extensively discussed in [55], an LC-ring composed of two capacitive-coupled LC tanks similar to what is shown in [58] cannot achieve quadrature operation, and active coupling devices are necessary to generate quadrature signals. This is also indicated in [58] that the quadrature locking

is actually achieved due to second-harmonic coupling. However, because of low-level harmonic contents at the oscillator's outputs, it is difficult to achieve a strong coupling between the two individual oscillators, resulting in undesirable high phase error ($\sim 3^\circ$ calculated from the reported SSB rejection ratio).

As another example of passive coupling, [59] uses transformers that provide coupling between the sources of one stage and the drains of the other stage. Therefore, coupling transistors are eliminated together with their noise effects. Moreover, the use of transformer at the source of transistors allows operation at lower-supply voltages. However, the operating frequency of this QVCO is away from the tank free-running oscillation frequency and depends on the coupling strength between the two differential oscillators which causes phase noise degradation similar to the conventional QVCOs. This problem has been addressed in [54] that relies on a ring of two magnetically coupled VCOs, where the resonance frequency is a function of passive components only, showing low noise and accurate quadrature phases. However, both of the QVCO structures in [59] and [54] have very limited tuning range.

It has been shown in [55] that by using a ring of N(>2) capacitive coupled LC tanks, it is possible to realize a high-accuracy multi-phase VCO with a FoM competitive to single-tank oscillators. Such a high-order LC-ring also provides multi-oscillation modes which can be exploited to realize a wide-tuning-range QVCO as in [56]. However, the quadrature oscillator in [56] requires four separate symmetrical inductors which are very area-consuming and significantly complicate the routing of signal paths. Another QVCO based on a transformer-based ring resonator was briefly reported in [60]. Due to use of transformers, it achieves considerable area saving while still maintaining the advantages of the topology in [56]. Moreover, in contrary to the left-handed LC ring resonator of [56] which always has higher loss in its lower resonance frequency, the proposed resonator can be designed to have

the same energy loss in both modes, reducing the variations in FoM throughout the whole tuning range. Compared to the conventional QVCO, the proposed oscillator employs passive components for quadrature signal generation and active devices are only required for loss compensation and switching between the two oscillation modes. As a result, it achieves a phase noise FoM comparable to single-tank VCOs. Moreover, by taking the advantage of its dual-resonance property, it covers more than of one octave frequency range.

This chapter provides an in-depth analysis of the proposed dual-band QVCO. It also offers more insight into the design and circuit implementation of the oscillator and shows how different parameters in the LC ring affect the phase noise performance and quadrature accuracy of the QVCO.

4.2 Proposed QVCO Architecture

4.2.1 Principle of Operation

Fig. 4.2(a) shows the proposed LC-ring resonator which is composed of two transformers coupled together through C_c capacitors [60]. Each transformer consists of two magnetically coupled coils with similar inductance of L ($L_1 = L_2 = L$), and coupling coefficient k ($=M/L$), loaded by capacitors C_1 and C_2 in its both sides ($C_1 = C_2 = C_p$). The total loss at each port of the resonator is modeled using a parallel resistor R_p. According to the Barkhausen criterion, the resonator oscillates when the total phase delay around the ring is an integer multiple of 2π. Moreover, because of the symmetry of the structure, $\Delta\varphi_1 = \Delta\varphi_3 = \theta_1$ and $\Delta\varphi_2 = \Delta\varphi_4 = \theta_2$. Therefore, considering the fact that the resonator operates differentially, it follows that $2\,(\theta_1 + \theta_2)$ must be an odd integer multiple of π or equivalently $(\theta_1 + \theta_2) = (2n+1)\pi/2$, where n is an integer number. Therefore, it can be concluded that irrespective of the values of θ_1 and θ_2, the total phase delay between V_1 and

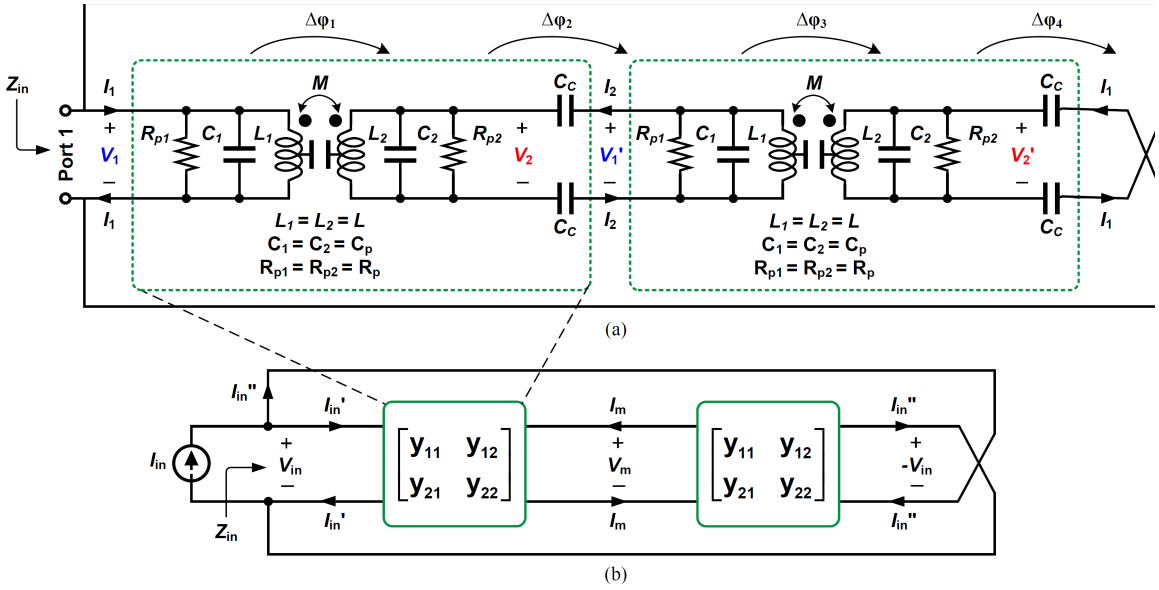

Fig. 4.2: (a) The proposed ring resonator, (b) a simplified model for calculating the input impedance looking into each port of the resonator.

V_1' (and also between V_2 and V_2') is always an odd integer multiple of $\pi/2$. In other words, upon compensating the losses in the system, the resonator produces two sets of quadrature signals (V_1, V_1') and (V_2, V_2') without requiring noisy coupling transistors. It should be noted that in general, inductors L_1 and L_2 can have different values without affecting the quadrature operation of the resonator. However, as it has been shown in [39] for a 4^{th}-order resonator, the symmetric case of $L_1 = L_2$ and $C_1 = C_2$ maximizes the voltage swing on both sides of the transformers, resulting in best phase noise performance. In the following, it will be shown that the resonator has two possible oscillation frequencies.

The resonance frequencies of the ring can be found from the input impedance looking into each port (Z_{in}). To determine Z_{in}, each half-circuit indicated in the

dashed box in Fig. 4.2(a) is replaced by its admittance matrix Y (see Fig. 4.2(b)).

$$Y = \begin{bmatrix} y_{11} & y_{12} \\ y_{21} & y_{22} \end{bmatrix}. \tag{4.2}$$

The expressions for y_{11}, y_{12}, y_{21} and y_{22} are found as

$$\begin{aligned}
y_{11}(s) &= \frac{N_{11}(s)}{D_{11}(s)}, \\
N_{11}(s) &= \left(L^2 - M^2\right) C_p \left(C_c + 2C_p\right) s^4 + \frac{1}{R_p}\left(L^2 - M^2\right)\left(C_c + 4C_p\right) s^3 \\
&\quad + \left[L\left(C_c + 4C_p\right) + \frac{2}{R_p^2}\left(L^2 - M^2\right)\right] s^2 + \frac{4}{R_p} L s + 2, \\
D_{11}(s) &= s\left[\left(L^2 - M^2\right)\left(C_c + 2C_p\right) s^2 + \frac{2}{R_p}\left(L^2 - M^2\right) s + 2L\right]; \\
y_{12}(s) &= y_{21}(s) = \frac{-MC_c s}{\left(L^2 - M^2\right)\left(C_c + 2C_p\right) s^2 + \frac{2}{R_p}\left(L^2 - M^2\right) s + 2L}; \\
y_{22}(s) &= \frac{C_c s\left[\left(L^2 - M^2\right) C_p s^2 + \frac{1}{R_p}\left(L^2 - M^2\right) s + L\right]}{\left(L^2 - M^2\right)\left(C_c + 2C_p\right) s^2 + \frac{2}{R_p}\left(L^2 - M^2\right) s + 2L}.
\end{aligned} \tag{4.3}$$

Referring to Fig. 4.2(b), the following equations can be derived

$$I'_{in} = y_{11} V_{in} + y_{12} V_m. \tag{4.4}$$

$$-I''_{in} = -y_{22} V_{in} + y_{21} V_m. \tag{4.5}$$

Subtracting (4.5) from (4.4) and considering the fact that $y_{12} = y_{21}$, results in

$$I'_{in} + I''_{in} = I_{in} = \left(y_{11} + y_{22}\right) V_{in}. \tag{4.6}$$

Thereby

$$Z_{in} = \frac{V_{in}}{I_{in}} = \frac{1}{y_{11} + y_{22}}. \tag{4.7}$$

By substituting y_{11} and y_{22} with their values from (4.3), the expression of the input impedance Z_{in} for $s = j\omega$ is obtained as follows

$$\begin{aligned}
Z_{in}(j\omega) &= \frac{N_{in}(j\omega)}{D_{in}(j\omega)}, \\
N_{in}(j\omega) &= \frac{j\omega}{2}\left[\left[2L - \left(L^2 - M^2\right)\left(C_c + 2C_p\right)\omega^2\right] + j\omega\frac{2\left(L^2 - M^2\right)}{R_p}\right], \\
D_{in}(j\omega) &= \left[\left(L^2 - M^2\right)C_p\left(C_c + C_p\right)\omega^4 - \left[L\left(C_c + 2C_p\right) + \frac{\left(L^2 - M^2\right)}{R_p^2}\right]\omega^2 + 1\right] \\
&\quad + \frac{j\omega}{R_p}\left[2L - \left(L^2 - M^2\right)\left(C_c + 2C_p\right)\omega^2\right]. \qquad (4.8)
\end{aligned}$$

Assuming the resonator is loss-less (i.e. $R_p \to \infty$), the oscillation frequencies can be obtained by setting the denominator of Z_{in} to zero, and are given by

$$\omega_{L,H}^2 = \frac{\alpha + 2 \pm \sqrt{\alpha^2 + 4k^2\left(\alpha + 1\right)}}{2\left(1 - k^2\right)\left(\alpha + 1\right)}\omega_o^2. \qquad (4.9)$$

where $\alpha = C_c/C_p$, and $\omega_o^2 = 1/(LC_p)$. Also, it can be seen from (4.8) that Z_{in} has a notch frequency located at

$$\omega_z^2 = \frac{2}{\left(1 - k^2\right)\left(\alpha + 2\right)}\omega_o^2. \qquad (4.10)$$

It is important to note that the value of R_p is generally different at the two resonance frequencies. As shown in Appendix, assuming the series resistance of the inductors (R_s) dominates in the resonator's loss, the values of R_p at ω_L and ω_H can be approximated as

$$R_{p,\omega_L} \approx \frac{2L}{R_s\left(C_c + 2C_p\right)}\frac{1 - \dfrac{\omega_L^2}{\omega_z^2}}{1 - \dfrac{2\left(\alpha + 1\right)}{\left(\alpha + 2\right)}\dfrac{\omega_L^2}{\omega_o^2}}. \qquad (4.11)$$

$$R_{p,\omega_H} \approx \frac{2L}{R_s\left(C_c+2C_p\right)}\frac{1-\dfrac{\omega_H^2}{\omega_z^2}}{1-\dfrac{2\left(\alpha+1\right)}{\left(\alpha+2\right)}\dfrac{\omega_H^2}{\omega_o^2}}. \tag{4.12}$$

As an illustration, the resonator is simulated with $L = 1.5$ nH, $C_p = 0.5$ pF, and assuming a quality factor Q of 15 for the inductors at 5 GHz ($R_s \approx 3.1\ \Omega$). The amplitude of Z_{in} is plotted in Fig. 4.3(a) and (b). In Fig. 4.3(a), $k = 0.3$ and α is tuned from 0.5 to 2 while in Fig. 4.3(b), $\alpha = 1$ and k is swept from 0.1 to 0.4. As expected, two resonance peaks and one zero appear in the amplitude response of Z_{in} with frequencies as predicted by (4.9) and (4.10), respectively. Note that the magnitude of Z_{in} at ω_L and ω_H corresponds to the value of R_p at these frequencies, i.e. R_{p,ω_L} and R_{p,ω_H}, respectively. As it is clear from Fig. 4.3(a) and (b), increasing both k and α makes the two peaks to become farther apart. However, k and α have opposite effects on R_{p,ω_L} and R_{p,ω_H}. While increasing k makes the lower resonance peak to be more dominant, increasing α causes the lower peak to go down and slightly pushes up the higher peak.

When designing a dual-mode oscillator, it is highly desirable to have the same energy loss in both bands. Otherwise, the oscillator will need to consume more power in the higher loss mode to maintain similar phase noise performance, leading to an imbalance operation in the two bands [39]. From the above discussion, by properly adjusting k and α, it is possible to make R_{p,ω_L} and R_{p,ω_H} to be equal and thereby achieve the same phase noise performance in both modes. Based on (4.11) and (4.12), the required condition for $R_{p,\omega_L} = R_{p,\omega_H}$ can be easily derived as

$$\omega_z^2 = \frac{2\left(\alpha+1\right)}{\left(\alpha+2\right)}\omega_o^2. \tag{4.13}$$

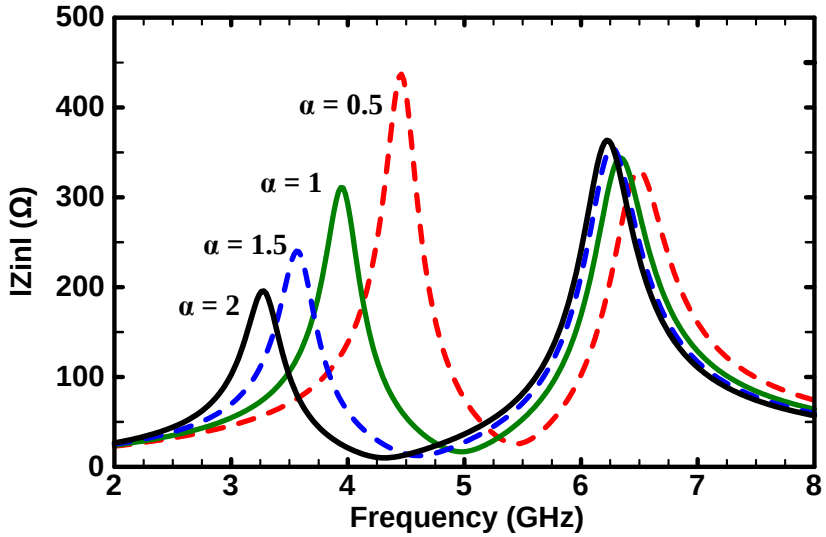

(a)

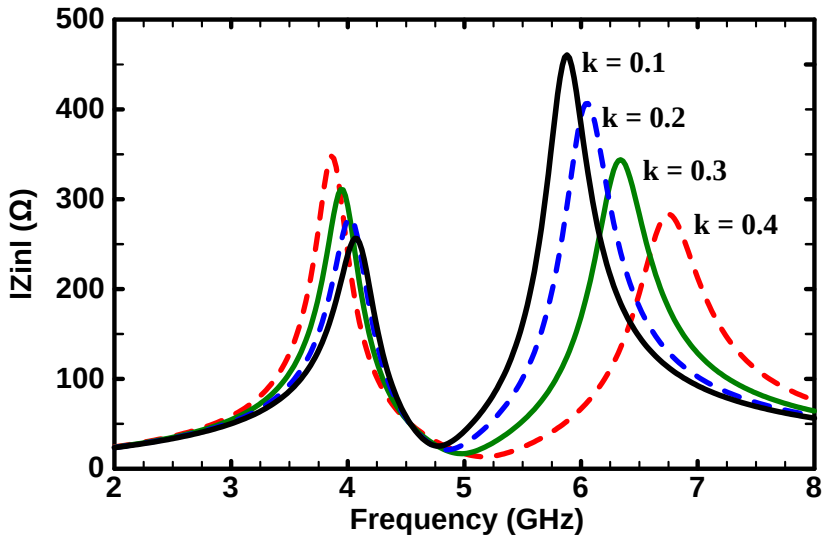

(b)

Fig. 4.3: Simulated resonator's input impedance when (a) $k = 0.3$ and α is swept from 0.5 to 2, and (b) $\alpha = 1$ and k is swept from 0.1 to 0.4 ($L = 1.5$ nH, $C_p = 0.5$ pF, $Q_{ind} = 15$ @ 5 GHz).

Substituting for ω_z from (4.10) yields

$$k = \frac{\alpha}{\alpha + 2} \tag{4.14}$$

Equation (4.14) reveals the required relation between k and α to obtain the same energy loss in both modes.

It is important to note that by making $R_{p,\omega_L} = R_{p,\omega_H}$, one can actually achieve the same quality factor for the resonator at the two oscillation frequencies. To verify this, the Q of the resonator at the two oscillation modes is derived in the following. The Q of an oscillator is defined as

$$Q = \frac{\omega_{osc}}{2} \frac{d\phi}{d\omega} \tag{4.15}$$

where ω_{osc} is the resonance frequency and $\phi(\omega)$ is the phase response of the resonator's input impedance. From the expression of Z_{in} in (4.39) in Appendix and for $L\omega_{osc}/R_s \gg 1$ and $1/(R_s C_p \omega_{osc}) \gg 1$, the quality factor of the resonator at ω_L and ω_H can be found as

$$Q_L \approx \frac{1}{R_s C_p \omega_L} \frac{1 - \dfrac{\omega_L^2}{\omega_H^2}}{(\alpha+2) - 2(\alpha+1)\dfrac{\omega_L^2}{\omega_o^2}}. \tag{4.16}$$

$$Q_H \approx \frac{1}{R_s C_p \omega_H} \frac{1 - \dfrac{\omega_H^2}{\omega_L^2}}{(\alpha+2) - 2(\alpha+1)\dfrac{\omega_H^2}{\omega_o^2}}. \tag{4.17}$$

By equating equations (4.16) and (4.17), and substituting for ω_L and ω_H with their values from (4.9), it is found that k and α must follow similar relation as in (4.14) to achieve the same Q in both bands.

In order to gain more insight into the resonator's operation, it is helpful to construct the phasor diagram of the circuit's voltages at the two resonant frequencies. As discussed earlier, when the resonator oscillates, $(\theta_1 + \theta_2)$ is an odd integer mul-

tiple of $\pi/2$ or equivalently, voltage pairs (V_1, V_1') and (V_2, V_2') run in quadrature. However, as will be shown in the following, θ_1 and θ_2 are highly a function of k and α values and play a very important role in the overall oscillator's performance. By inspection of Fig. 4.2(a), the ratio between V_1 and V_2 can be derived as

$$\frac{V_2}{V_1} = \frac{MI_1 + (L + (L^2 - M^2)\, C_p s^2)\, I_2}{(L + (L^2 - M^2)\, C_p s^2)\, I_1 + MI_2}. \tag{4.18}$$

Referring to Fig. 4.2(a), the following equation can be derived

$$\begin{bmatrix} I_1 \\ I_2 \end{bmatrix} = \begin{bmatrix} y_{11} & y_{12} \\ y_{21} & y_{22} \end{bmatrix} \begin{bmatrix} V_1 \\ V_1' \end{bmatrix}. \tag{4.19}$$

Based on (4.7), $y_{11} + y_{22} = 0$ at resonance, and due to the reciprocity of the circuit $y_{12} = y_{21}$. Therefore, (4.19) can be rewritten as

$$\begin{bmatrix} I_1 \\ I_2 \end{bmatrix} = \begin{bmatrix} y_{11} & y_{12} \\ y_{12} & -y_{11} \end{bmatrix} \begin{bmatrix} V_1 \\ V_1' \end{bmatrix}. \tag{4.20}$$

At steady state, the voltages across the four LC tanks tend to have the same amplitude, hence, $V_1' = \pm jV_1$ and $V_2' = \pm jV_2$. By substituting $V_1' = \pm jV_1$ into (4.20), it can be easily found that $I_2 = \mp jI_1$. Replacing $I_2 = \mp jI_1$ and $s = j\omega$ in (4.18) yields

$$\frac{V_2}{V_1} = \frac{M \mp j\,(L - (L^2 - M^2)\, C_p \omega^2)}{(L - (L^2 - M^2)\, C_p \omega^2) \mp jM}. \tag{4.21}$$

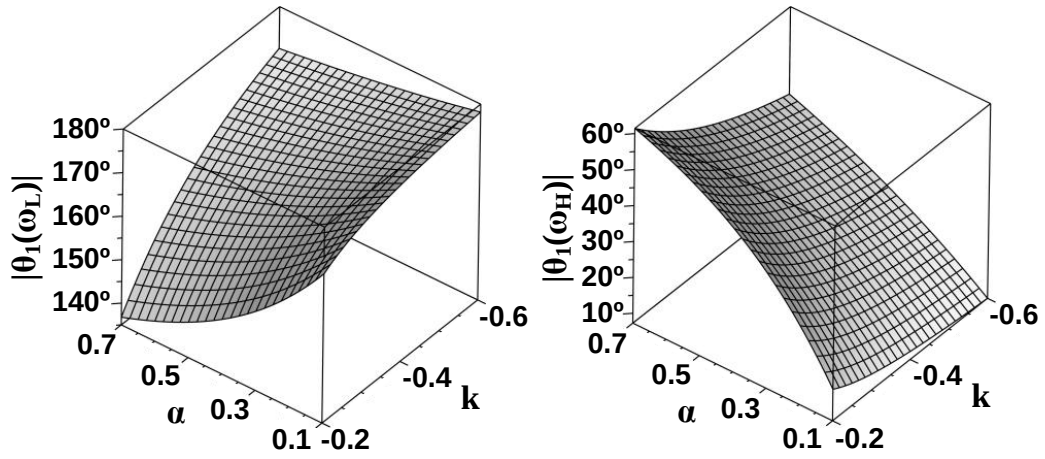

Fig. 4.4: Phase shift between V_1 and V_2 (θ_1) as a function of k and α at (a) ω_L and (b) ω_H ($k < 0$).

Therefore

$$\angle\frac{V_2}{V_1} = \theta_1 = \mp\tan^{-1}\left(\frac{1-(1-k^2)\,\omega^2/\omega_o^2}{k}\right) \pm \tan^{-1}\left(\frac{k}{1-(1-k^2)\,\omega^2/\omega_o^2}\right). \tag{4.22}$$

By substituting ω_L and ω_H values from (4.9) in (4.22), θ_1 can be found as a function of k and α which is graphically shown in Fig. 4.4. Interestingly, it can be seen that always $\pi/2 < \theta_1(\omega_L) < \pi$ and $0 < \theta_1(\omega_H) < \pi/2$. As will be discussed in the next section, the switching between the two oscillation modes is accomplished by taking advantage of this property. Now that the phase relationship between all the voltages across the LC tanks is known, the resonator phasor diagrams at ω_L and ω_H can be drawn as depicted in Fig. 4.5. Note that because of the symmetry, signals can propagate either clockwise or counter-clockwise along the ring, resulting in two different possible phase patterns in each oscillation frequency.

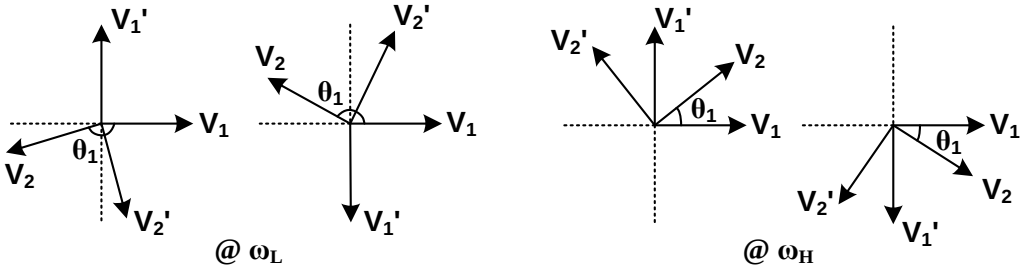

Fig. 4.5: Phasor diagrams of resonator's voltages at the two oscillation frequencies.

4.2.2 Mode Selection

As in any oscillator circuit, the losses need to be compensated by the energy provided by the active devices. This can be simply done by placing a negative transconductor $-G_m$ at each port of the resonator, as illustrated in Fig. 4.6. In order to ensure the start-up of the oscillation, the value of G_m must be chosen to satisfy $G_m R_p \geq 1$. As explained in the previous section, the input impedance looking into each port has two potential resonant frequencies ω_L and ω_H, and the resonator is designed to show approximately the same losses at these frequencies to maintain the same FoM in two modes. In such a scenario, the negative transconductors are not able to discriminate between two resonant frequencies and might satisfy oscillation conditions at both ω_L and ω_H. In other words, the resonator can potentially oscillate at either ω_L or ω_H, or even simultaneously oscillate at both frequencies. In the following it will be shown how to make the oscillator operate stably at the desired mode.

First, suppose injecting a current into each side of the transformers with a value proportional to the voltage on the other side, as illustrated in Fig. 4.6. Taking port 1 as an illustration, a current of $I_{inj1} = G_{mc} V_2$ is injected into this port. The phasor diagram can be thereby constructed as shown in Fig. 4.7. The injected

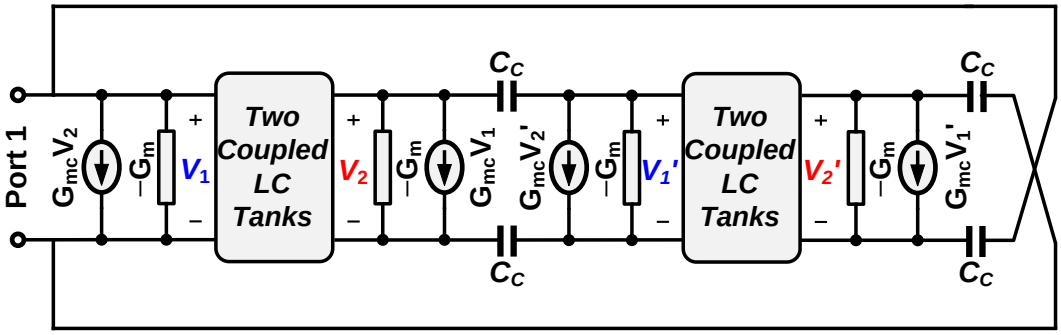

Fig. 4.6: Addition of transconductors to the resonator for stimulating the desired oscillation mode.

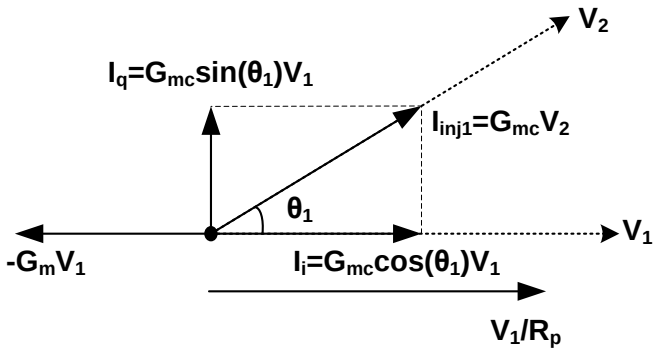

Fig. 4.7: Phasor diagram.

current can be decomposed into two orthogonal components: $I_q = G_{mc}\sin(\theta_1)V_1$ and $I_i = G_{mc}\cos(\theta_1)V_1$. I_q which is in quadrature with the current $I_L = V_1/R_p$ does not provide any loss compensation and as will be discussed later causes phase noise degradation. On the other hand, I_i can be in-phase or 180° out-of-phase with I_L depending on the polarities of G_{mc} and $\cos(\theta_1)$. In other words, this components can inject or dissipate energy depending on if the product of $G_{mc}\cos(\theta_1)$ is negative or positive, respectively. The value of $\cos(\theta_1)$ can be easily derived from (4.22) as

follows

$$\cos(\theta_1) = \frac{2k}{(1-k^2)(\alpha+2)\dfrac{\omega^2}{\omega_o^2} - 2} \tag{4.23}$$

Based on (4.10), equation (4.23) can be rewritten as

$$\cos(\theta_1) = \frac{2k}{1-\omega^2/\omega_z^2} \tag{4.24}$$

Since $\omega_L < \omega_z < \omega_H$, it can be concluded from (4.24) that $\cos(\theta_1)$ is negative when the resonator works at ω_L while it becomes positive at ω_H. This result is also evident in Fig. 4.4. Consequently, when $G_{mc} < 0$, I_i will add extra losses to the LC tanks at ω_L, making the effective transconductance ($G_{m,eff}$) at each port to be $-G_m + |G_{mc}\cos(\theta_1)|$. On the other hand, I_i will appear as a negative transconductance at ω_H, making $G_{m,eff}$ to be $-G_m - |G_{mc}\cos(\theta_1)|$. To ensure start-up of the oscillation at ω_H and damp any undesired oscillation at ω_L, the following conditions must be satisfied

$$\begin{aligned} &(G_m - |G_{mc}\cos(\theta_1)|)\, R_{p,\omega_L} < 1, \\ &(G_m + |G_{mc}\cos(\theta_1)|)\, R_{p,\omega_H} > 1. \end{aligned} \tag{4.25}$$

Therefore, a sufficiently negative G_{mc} can ensure stable oscillation at ω_H. Similarly, it is easy to check that a sufficiently positive G_{mc} that satisfies the following two conditions can guarantee sustainable oscillation at ω_L.

$$\begin{aligned} &(G_m + |G_{mc}\cos(\theta_1)|)\, R_{p,\omega_L} > 1, \\ &(G_m - |G_{mc}\cos(\theta_1)|)\, R_{p,\omega_H} < 1. \end{aligned} \tag{4.26}$$

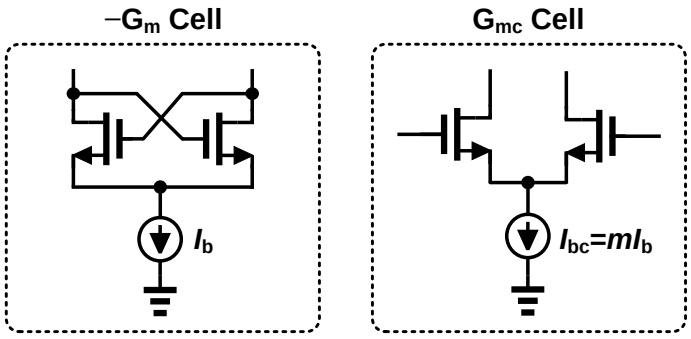

Fig. 4.8: Implementation of $-G_m$ and G_{mc} cells using NMOS cross-coupled transistors and NMOS differential pairs, respectively.

To summarize the above discussion, the switching between two resonant modes can be simply accomplished by only flipping the polarity of G_{mc}. A similar mode switching scheme have been also used in some other recently published multi-band oscillators such as [39, 57, 61–63] .

4.2.3 Oscillation Amplitude

Consider that each of $-G_m$ and G_{mc} cells in Fig. 4.6 to be implemented respectively using NMOS cross-coupled transistors and NMOS differential pairs as illustrated in Fig. 4.8. At relatively high oscillation amplitudes, the transconductor cells essentially act as hard limiters, nearly injecting square-wave currents into the LC tanks. Due to the bandpass filtering response of the resonator, only the fundamental harmonics of currents are retained, which are equal to $2I_b/\pi$, $2I_{bc}/\pi$ $(= 2mI_b/\pi)$ for $-G_m$ and G_{mc} cells, respectively. Parameter m is defined as the ratio between the tail currents of the $-G_m$ and G_{mc} cells ($m = I_{bc}/I_b$). As discussed in previous section, the current component of G_{mc} which is in quadrature with the output voltage (for example $G_{mc}\sin(\theta_1)V_1$ in Fig. 4.7) provides no loss compensation. Therefore,

the voltage amplitude across each LC tank can be expressed as

$$V_0 = \frac{2}{\pi} R_p I_b \left(1 + m \left|\cos(\theta_1)\right|\right). \tag{4.27}$$

while the oscillator consumes a total current of $4(1 + m)I_b$. As a result, compared to a single-tank oscillator, the proposed QVCO will need to consume $4(1 + m)/\left(1 + m \left|\cos(\theta_1)\right|\right)$ times more power to achieve the same voltage amplitude.

4.2.4 Phase Noise

In order to find the optimum values for different parameters in the proposed resonator, a solid understanding of their effects on phase noise performance proves essential. Several different methods exist for the analysis of phase noise in LC-oscillators. In the most general analysis technique, introduced by Hajimiri [64], the oscillator is characterized using the impulse sensitivity function (ISF) which provides a complete description of the noise sensitivity of the oscillator. This time-variant-linear approach will be used in the following to calculate the phase noise of the QVCO.

The phase noise $L(\Delta\omega)$ at an offset frequency $\Delta\omega$ from the carrier can be expressed as [54, 64, 65]

$$L(\Delta\omega) = 10 \log \left(\frac{\Sigma_i N_{L,i}}{2 q_{max}^2 \Delta\omega^2} \right). \tag{4.28}$$

with q_{max} being the maximum charge displacement across the capacitor on the oscillation node, and $N_{L,i}$ the effective noise power which is converted to phase noise for ith source, and is given by

$$N_{L,i} = \frac{1}{T_0} \int_0^{T_0} \Gamma_i^2(t) \, \overline{i_{n,i}^2} \, dt \,. \tag{4.29}$$

where T_0 is the oscillation period, $\overline{i_{n,i}^2}$ is the power spectral density of the ith noise source, and Γ_i is the corresponding ISF. Because of the symmetry of the QVCO in Fig. 4.6, phase noise can be analyzed by considering only the thermal noise associated to one of the four coupled oscillators. The total phase noise can be then obtained by adding in power the phase noise generated by each of the four uncorrelated noise sources. It is well known that for a differential oscillator the ISF at a specific node is approximately a sinusoid in quadrature with the node voltage. Extensive simulations show that for the QVCO in Fig. 4.6, this approximation is only valid for very small values of $|G_{mc}|$. However, as $|G_{mc}|$ increases, the phase shift between the ISF at each port and the corresponding voltage deviates from ideal quadrature. Based on the analysis in [65], assuming the voltage at port-1 is $V_0 \sin(\omega_{osc}t)$, the ISF associated with this port can be well approximated as

$$\Gamma_i(\omega_{osc}t) = \frac{1}{N\cos\varphi}\cos\left(\omega_{osc}t + \varphi\right). \tag{4.30}$$

where $N(=4)$ is the number of coupled LC tanks, ω_{osc} is the oscillation frequency, and φ is the departure of ISF from ideal quadrature, given by

$$\varphi = \tan^{-1}\frac{m\sin(\theta_1)}{1+m\cos(\theta_1)}. \tag{4.31}$$

Now, taking port 1 for illustration, the phase noise contribution of R_p can be simply calculated using (4.29), (4.30) and (4.31) as [54]

$$\begin{aligned} N_{L,R_p} &= \frac{1}{T_0}\int_0^{T_0}\left(\frac{1}{N\cos\varphi}\cos\left(\omega_{osc}t+\varphi\right)\right)^2\frac{4KT}{R_p}\,dt \\ &= \frac{KT}{8R_p\cos^2(\varphi)} = \frac{KT}{8R_p}\eta. \end{aligned} \tag{4.32}$$

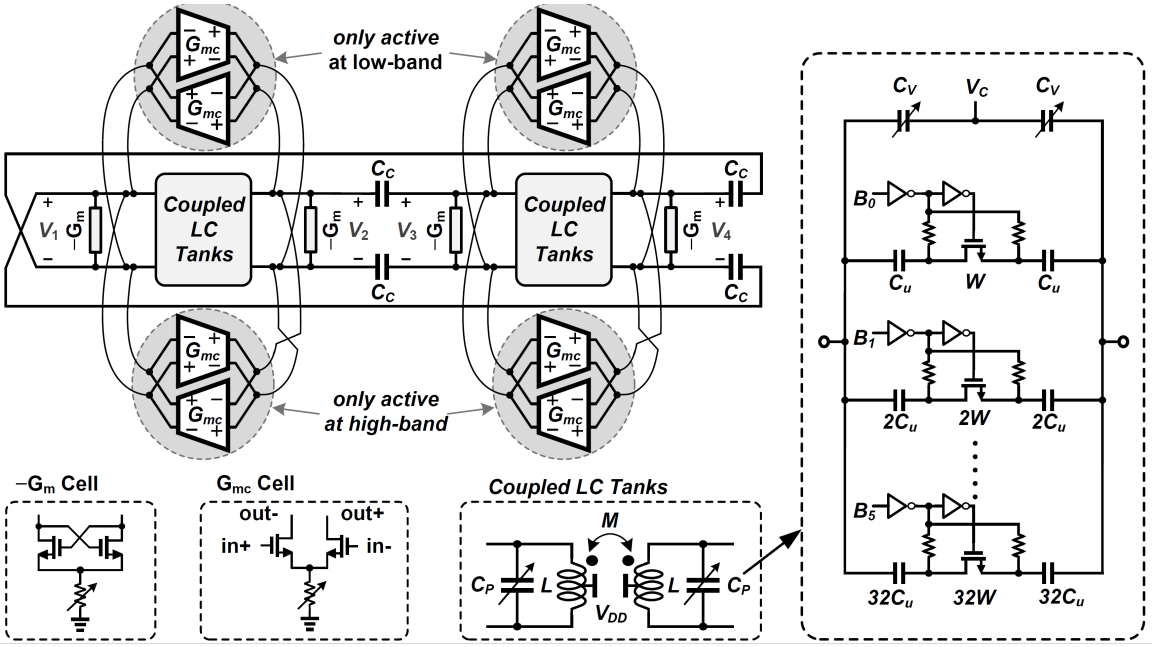

Fig. 4.9: Complete schematic of the realized dual-band QVCO.

where

$$\eta = \frac{1 + m^2 + 2m\cos(\theta_1)}{(1 + m\cos(\theta_1))^2}. \tag{4.33}$$

Expressing the noise contributions of the G_m and G_{mc} cells by the noise factor F_N [47, 66], the total phase noise can be calculated by means of (4.28) and (4.32) as

$$\begin{aligned} L(\Delta\omega) &= 10\log\left(\frac{1}{2q_{max}^2\Delta\omega^2}\frac{KT\eta\,(1+F_N)}{2R_p}\right) \\ &= 10\log\left(\frac{1}{C_p^2V_0^2\Delta\omega^2}\frac{KT\eta\,(1+F_N)}{4R_p}\right) \\ &= 10\log\left(\frac{1}{\omega_{osc}^2C_p^2R_p^2I_{rms}^2}\frac{\omega_{osc}^2}{\Delta\omega^2}\frac{KT\eta\,(1+F_N)}{4R_p}\right) \\ &= 10\log\left(\frac{1}{Q^2I_{rms}^2}\frac{\omega_{osc}^2}{\Delta\omega^2}\frac{KT\eta\,(1+F_N)}{4R_p}\right). \end{aligned} \tag{4.34}$$

where Q is defined to be $R_pC_p\omega_{osc}$.

In order to gain more insight, the phase noise of the QVCO is compared with phase noise of a single-tank oscillator $L_s(\Delta\omega)$. Following the above analysis, the expression for $L_s(\Delta\omega)$ can be easily obtained as

$$L_s(\Delta\omega) = 10\log\left(\frac{1}{Q_s^2 I_{rms}^2}\frac{\omega_o^2}{\Delta\omega^2}\frac{KT\,(1+F)}{R_p}\right). \tag{4.35}$$

Therefore, from (4.34) and (4.35), the phase noise difference between the proposed QVCO and a single-tank oscillator is derived as

$$L(\Delta\omega) - L_s(\Delta\omega) = 10\log\left(\frac{\eta}{4}\,\frac{1+F_N}{1+F}\right). \tag{4.36}$$

In a single-tank LC VCO, the phase noise caused by the negative transconductor is to a large extent due to the thermal noise ($= 4KT\gamma g_m$) of the cross-coupled transistors. However, in the QVCO of Fig. 4.6, G_{mc} cells with thermal noise of $4KT\gamma m g_m$ also contribute to the overall phase noise. Assuming the resonance frequencies and the voltage amplitudes for the two oscillators are the same, F_N can be written using (4.27) as follows

$$F_N = \frac{1+m}{1+m\,|\cos(\theta_1)|}F. \tag{4.37}$$

Equation (4.36) reveals that the phase noise is reduced by a factor of 4 due to the coupling of 4 LC tanks. This is, of course, achieved at the expense of $4(1+m)/\,(1+m\,|\cos(\theta_1)|)$ times higher power consumption, as discussed earlier. Moreover, based on (4.36) and (4.37), the coupling transconductors that are employed for selecting the desired oscillation mode, degrade the phase noise performance. It is clear that the phase noise degradation becomes more pronounced as m increases and $|\cos(\theta_1)|$ tends toward zero. These results provide important design insights for the QVCO as explained in the following: The phase noise performance can be improved

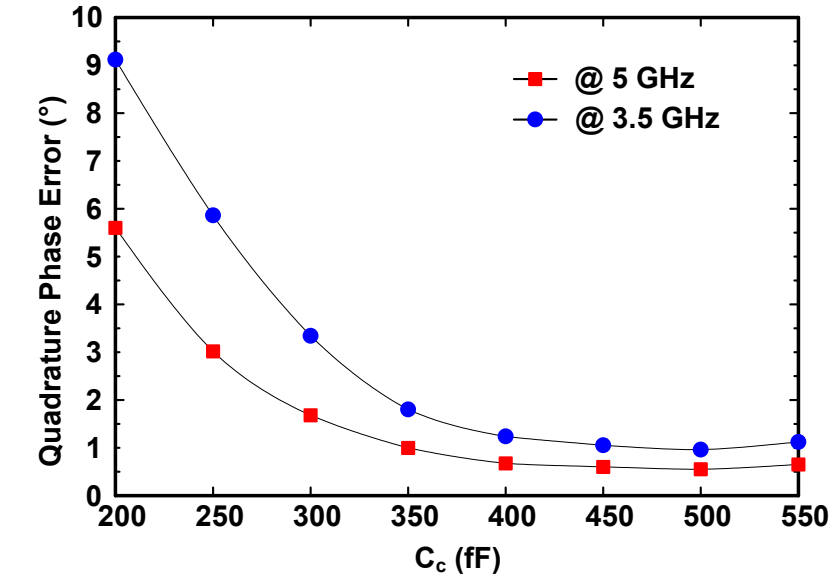

(a)

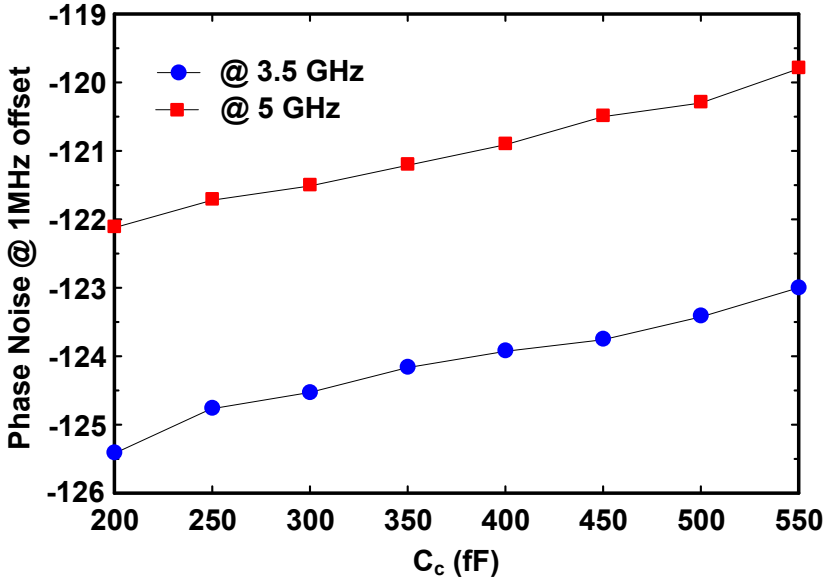

(b)

Fig. 4.10: Simulated (a) phase error and (b) phase noise at 1 MHz offset versus coupling capacitor C_c and for two different oscillation frequencies of 3.5 GHz (low-band) and 5 GHz (high band).

by (a) selecting m ($= |G_{mc}/G_m|$) to be as small as possible, or in other words $|G_{mc}|$ must be chosen to be only large enough to ensure oscillation at the desired mode

even at the presence of worst case process, voltage and temperature (PVT) variations, and (b) choosing larger value for $|k|$ and smaller value for α. From Fig. 4, as $|k|$ increases and α decreases, θ_1 tends towards 180° (0°) at ω_L (ω_H), which makes η and F_N go to one and F, respectively.

4.3 Circuit Design and Implementation

From the discussion so far, it is clear that the coupling parameters k and α play an important role in the overall performance of QVCO and must be chosen very carefully. There are two considerations in determining the value of these parameters. First, while larger coupling factor $|k|$ is more desirable for low phase noise performance, it drops the higher resonant peak and increases the separation between two oscillation frequencies. Therefore, the maximum acceptable value of $|k|$ is determined by the targeted frequency range (Fig. 4.3). After a few iterations, the value of k in the prototype was selected to be -0.28. Second, smaller α results in better phase noise performance but on the other hand it makes the QVCO more susceptible to the unavoidable component mismatches, thereby, degrading the quadrature phase accuracy. Accordingly, there is a lower bound on the value of α imposed by the required quadrature accuracy. It is important to note that when C_c is fixed, α becomes smaller by increasing C_p. As a result, better phase noise performance but with higher phase error is expected with reducing frequency in each band.

In order to see the sensitivity of the QVCO to the component mismatches, Fig. 4.10(a) shows the simulated phase error for different values of C_c assuming 1% mismatch between the loading capacitors (C_p) of the two coupled transformers (the value of C_p is equal to C for the left transformer, and $C + \Delta C$ for the right transformer in Fig. 4.9) at the two oscillation frequencies of 3.5 GHz (low-band) and 5 GHz (high-band). The simulated phase noise as a function of C_c is also shown in

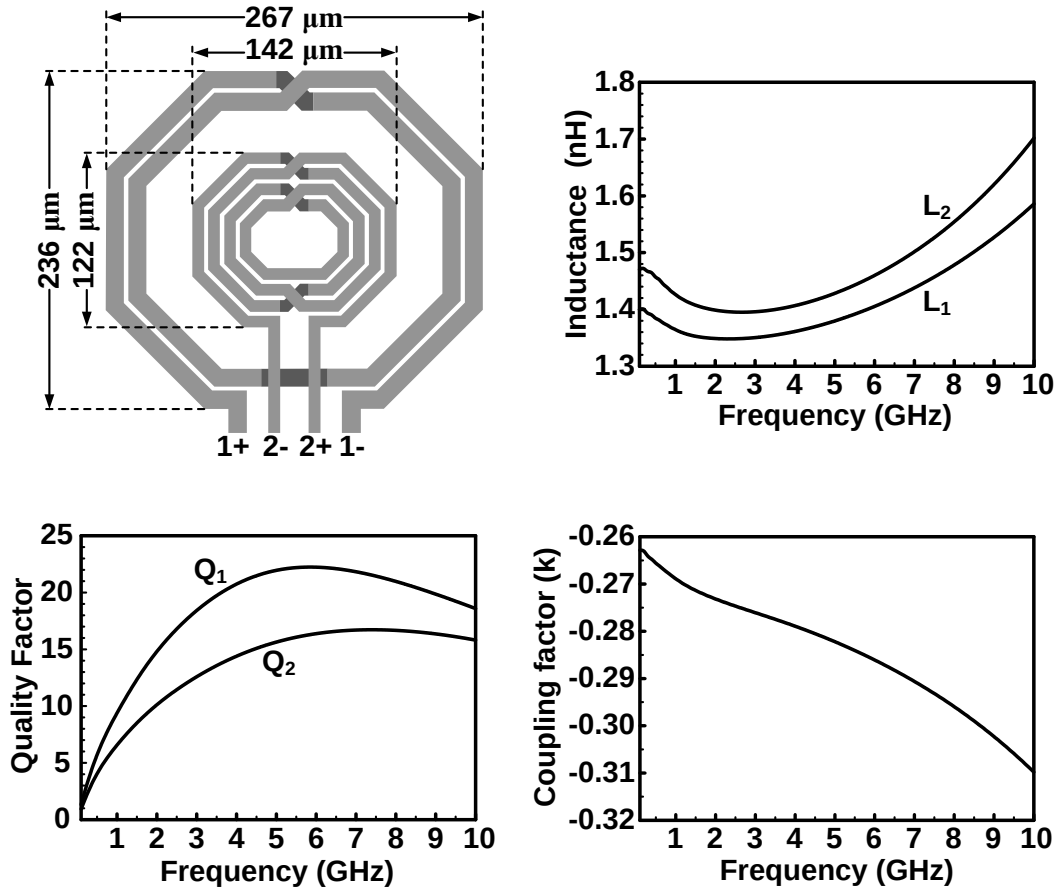

Fig. 4.11: Transformer layout, and its electromagnetic simulation results using Sonnet.

Fig. 4.10(b). In these simulations, the value of C_p is tuned accordingly to keep the oscillation frequency constant. As expected, the phase error is reduced by increasing C_c at both modes. Also, it is seen that the phase error is small and does not vary much for C_c >400 fF but it only degrades the phase noise performance. As a result, the optimum value of C_c is found to be 400 fF.

Fig. 4.9 shows the complete schematic of the dual-band QVCO. The voltage-controlled current sources in Fig. 4.6 are implemented using two sets of G_{mc} cells with opposite polarities. For the top G_{mc} cells, the effective transconductance is

positive ($G_{mc} > 0$) while in the bottom G_{mc} cells, the polarity of connections is reversed to have a negative transconductance ($G_{mc} < 0$). Therefore, in order to make the oscillator to work at the lower (higher) frequency band, the top (bottom) G_{mc} cells are turned on while the other G_{mc} cells are kept turned off. The negative transconductors ($-G_m$ cells) are always on at both resonant modes. Each of $-G_m$ and G_{mc} cells are realized using NMOS cross-coupled pairs and NMOS differential pairs, respectively. All of the transconductors are biased with digitally-controlled variable resistors to minimize the sources of flicker noise in the QVCO. Both coarse and fine tuning methods are adopted to cover the required tuning range in each band while achieving low VCO gain (K_{VCO}) for better phase noise performance. The coarse frequency tuning is accomplished by a 6-bit binary-weighted switched capacitor bank, while the fine tuning is achieved by a pair of small NMOS varactors. C_c's are fixed and implemented by means of high-Q metal-insulator-metal (MIM) capacitors. The QVCO core uses a low power supply voltage of 0.6 V. The MOS switches that consume no static power are controlled through a 0/1.2 V voltage bias to minimize their on-resistance. In order to use the whole range of MOS varactors, they are directly connected to the inductors with dc bias of 0.6 V and their control voltage is tuned from 0 to 1.2 V.

4.4 Fabrication and Measurement Results

The transformer was realized in 65 nm CMOS technology using the 3.4 μm thick top metal layer. The layout of the implemented transformer is shown in Fig. 4.11, where the inner inductor has four turns with metal width of 8 μm while the outer one has two turns with metal width of 12.5 μm, for maximum quality factor. Fig. 4.11 also shows the simulated quality factor, inductance, and coupling factor (k) for the two coupled inductors using the electromagnetic simulator Sonnet. The inner and outer

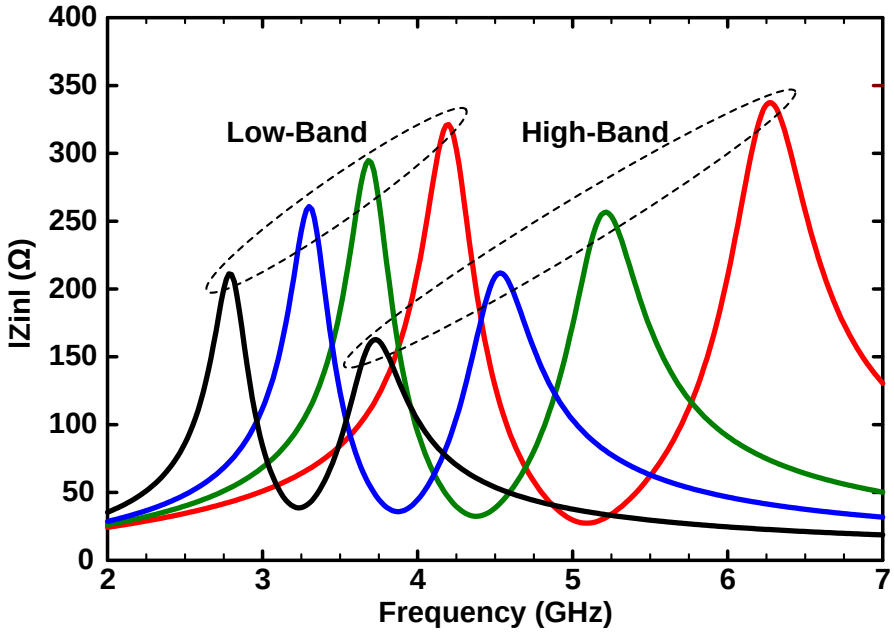

Fig. 4.12: Amplitude of Z_{in} for four different values of B<5:0>.

coils achieve quality factors of 15.6 and 22 at 5 GHz, respectively while showing approximately the same inductance of 1.4 nH. Fig. 4.12 shows the simulated resonator's input impedance Z_{in} when the digital control word of the switched-capacitor banks (B<5:0>) is swept. At the low and high frequency bands, QVCO continuously covers 2.7-4.2 GHz and 3.6-6.3 GHz, respectively, leading to whole frequency coverage of 2.7-6.3 GHz. Also, as can be seen, the amplitudes of Z_{in} at the two resonant frequencies are almost the same, ranging from 210 to 320 Ω at the low-band and from 190 to 340 Ω at the high-band (not considering the overlap region). As a result, nearly the same power needs to be consumed in both modes to push the oscillator into the voltage-limited regime.

The QVCO was fabricated in a TSMC 65 nm CMOS technology and encapsulated in a 32-pin QFN package for performance characterization. A die microphotograph of the chip is shown in Fig. 4.13. The chip occupies an active core area of 0.35 mm^2 and

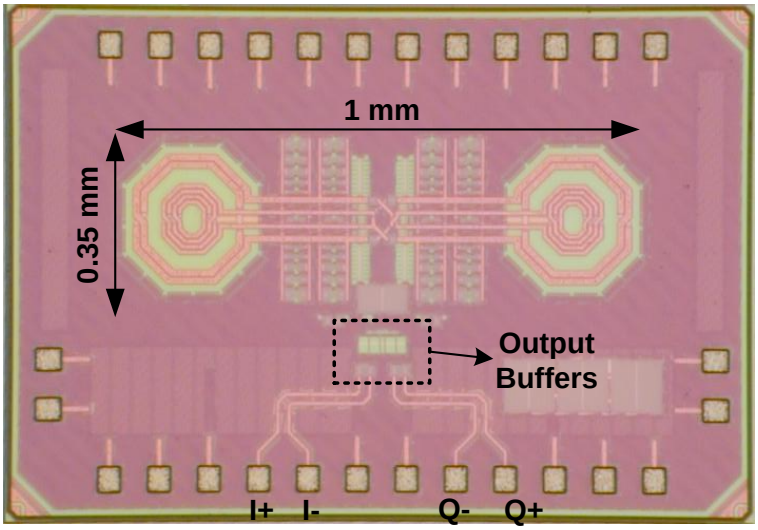

Fig. 4.13: QVCO Chip Photograph.

consumes a total current of 9.7-15.6 mA from a 0.6 V voltage supply. With reducing frequency in each band, the amplitude of the input impedance Z_{in} drops and thereby more power must be consumed to achieve low phase noise performance. The tuning range of the QVCO was measured using an Agilent E4446A spectrum analyzer and is shown in Fig. 4.14(a), in which each bar represents the continuous tuning range when the control voltage of varactors is tuned from 0 to 1.2 V. The QVCO continuously covers the frequency range of 2.75-4.2 GHz at the low-band and 3.62-6.25 GHz at the high-band, corresponding to the tuning ranges of 41.7% and 53.3%, respectively. The significant overlap between the two bands ($\sim$ 580 MHz) ensures continuous tuning range under worst case PVT variations. The measured frequency ranges are very close to the simulated values, which are 2.84 GHz to 4.34 GHz and 3.67 GHz to 6.68 GHz, for low-band and high-band, respectively.

The QVCO phase noise is also measured using Agilent E4446A spectrum analyzer. Fig. 4.14(b) shows the simulated and measured phase noise at 1 MHz offset across

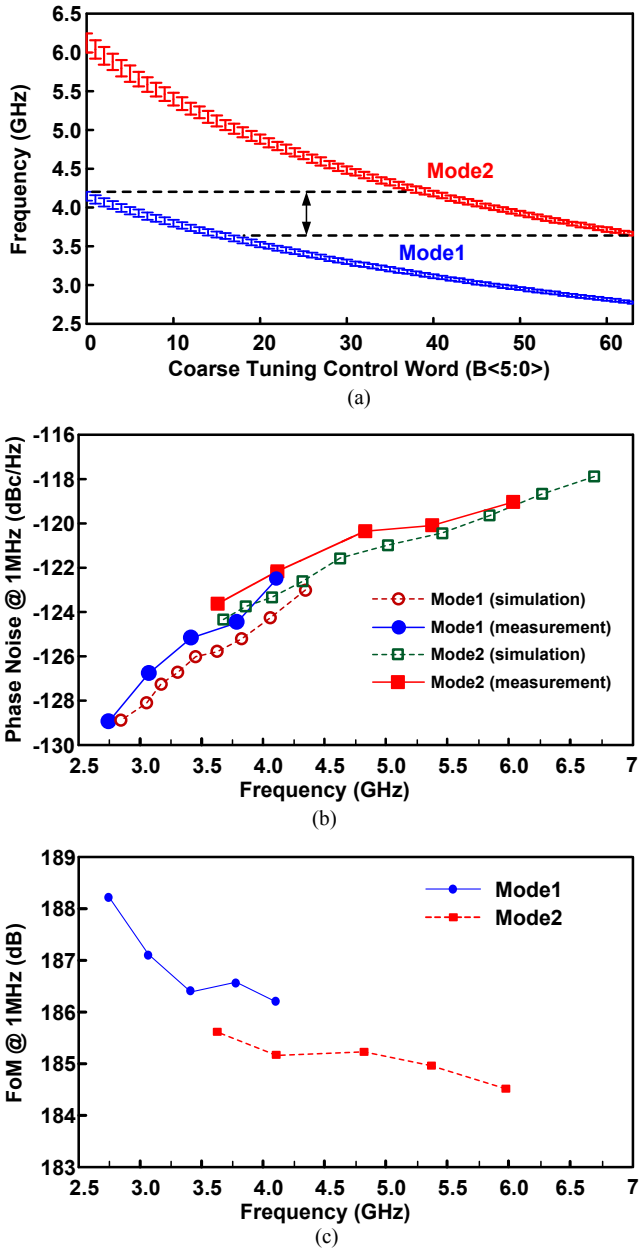

Fig. 4.14: (a) Measured QVCO tuning range, (b) simulated and measured phase noise at 1 MHz offset across the tuning range, (c) measured FoM at 1 MHz offset across the tuning range.

the entire tuning range. The varactor voltage was set to 0 V for the phase noise measurements. The QVCO gain (K_{VCO}) has its minimum value at this voltage;

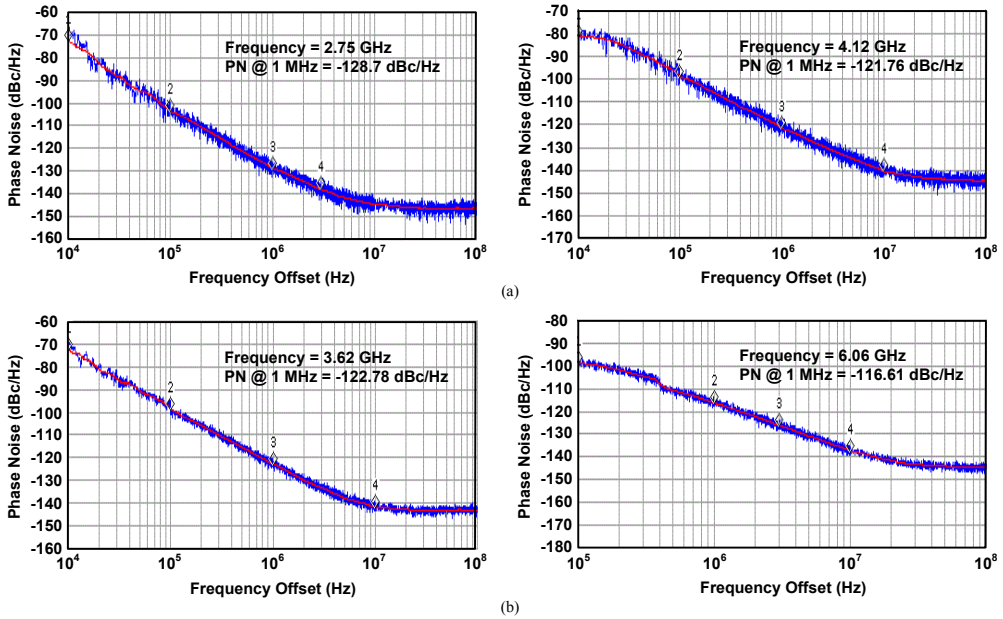

Fig. 4.15: Measured phase noise (PN) at the lowest and highest frequencies of the (a) low-band and (b) high-band when the varactor control voltage is set to 0 V.

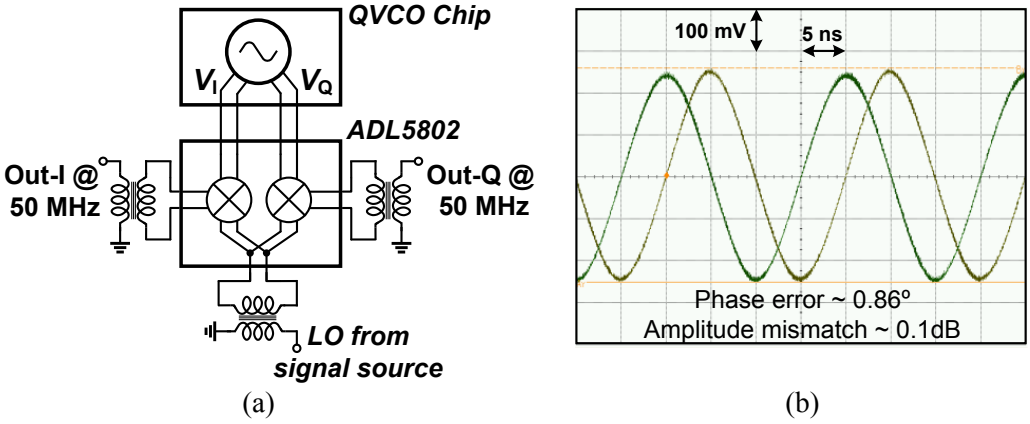

Fig. 4.16: (a) Setup for measuring the phase accuracy of the QVCO, (b) 6 GHz quadrature output signals down-converted to 50 MHz.

thereby Fig. 4.14(b) shows the best achievable phase noise performance. A phase noise degradation of up to 1.2 dB was observed at 1 MHz offset frequency for the

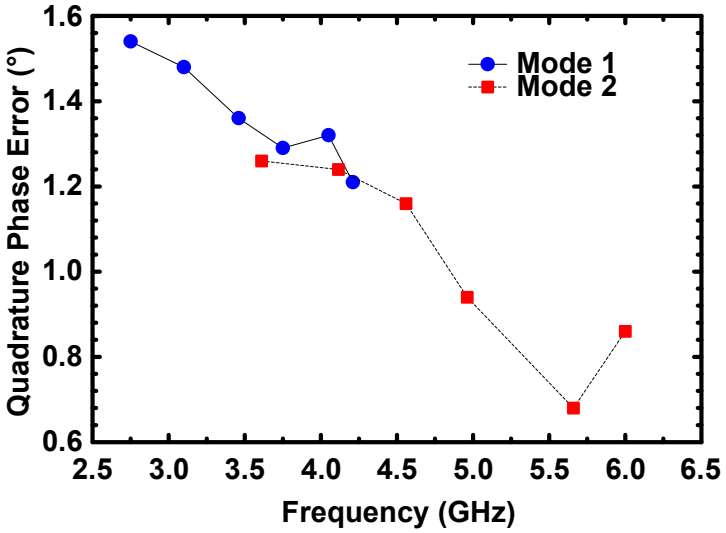

Fig. 4.17: Measured quadrature phase error as a function of oscillation frequency.

worst case varactor setting across the tuning range. The corresponding FoM for the measured phase noise data is also depicted in Fig. 4.14(c), where FoM is defined as

$$FoM = 10\log_{10}\left[\frac{1}{P_{diss,mW}}\left(\frac{f_{osc}}{\Delta f}\right)^2\right] - L(\Delta f). \tag{4.38}$$

The FoM of QVCO ranges from 184-188.2 dB which is comparable to those of differential multi-band LC oscillators [39, 63]. Fig. 4.15(a) and (b) show the measured phase noise profiles at the lowest and highest frequencies in each band, respectively when the control voltage of varactor is 0 V.

In order to measure the quadrature phase accuracy, the QVCO outputs are downconverted to a low frequency of 50 MHz using an external LO. As depicted in Fig. 4.16(a), an off-chip dual-channel mixer (ADL5802 from Analog Devices) is used for frequency down-conversion and is mounted very close to the QCVO chip on the testing board to minimize the errors in the measurement setup. Fig. 4.16(b) shows the down-converted 6 GHz quadrature signals at 50 MHz. The same mea-

Table 4.1: Performance Summary and Comparison to Reported Wide-Tuning-Range QVCOs.

	[67]	[57]	[68]	[69]	[56]	This Work
CMOS Process	0.18 μm	0.13 μm	65 nm	0.13 μm	65 nm	65 nm
Supply Voltage (V)	1	1.2	1.2	1.2	0.6	0.6
Power (mW)	6-10	14-24	7.2-24	20-29	9.8-11.1	5.8-9.4
Frequency (GHz)	3.27-5.02 /9.48-11.36	2.7-4.3 /8.4-12.4	3.2-6.4	11.5-22	2.78-5.00	2.75-6.25
Tuning Range	42% / 18%	46% / 38%	67%	62.7%	57%	78%
PN @ 1 MHz (dBc/Hz)	-116.3 @ 4.2 GHz	-125.2 @ 3.6 GHz	-114.1 @ 3.2 GHz	-107 @ 13.3 GHz	-124.9 @ 3.66 GHz	-123.7 @ 3.8 GHz
FoM @ 1 MHz (dB)	181-182	177-185	170.5-176.5	< 176.5	180-186	184-188.2
Phase Error	$< 0.5°$	$< 1.6°$	$< 1.5°$	$< 3.3°$	N/A	$< 1.5°$
Area (mm^2)	0.88	0.84	0.2	N/A	1	0.35

surement is repeated across the entire tuning range and the results are shown in Fig. 4.17. The quadrature phase error of the QVCO is always less than 1.5° over its entire operating range.

The experimental results are summarized in Table 4.1 and compared against the other state-of-the-art wide-tuning-range QVCOs. The presented oscillator shows a competitive FoM while covering the widest tuning range among the other published QVCOs, to the best of authors' knowledge. It also achieves good quadrature phase accuracy and consumes a relatively small silicon area.

4.5 Summary

A novel dual-band quadrature oscillator was presented using a transformer-based LC ring. The proposed structure was verified by a prototype in 65 nm CMOS technology, which achieves low phase noise performance and covers a wide frequency range of 2.75-6.25 GHz. A thorough analysis of the QVCO's operation and its performance was also provided.

4.6 Appendix

This appendix drives equations for R_{p,ω_L} and R_{p,ω_H} assuming the series resistance of the inductors dominates in the resonator's loss.

Modeling the resonator's energy loss with a resistor R_s in series with the inductors and following the same analysis as in Section 4.2.1, the input impedance Z_{in} can be found as

$$\begin{aligned}
Z_{in}(s) &= \frac{N(s)}{D(s)}, \\
N(s) &= \frac{j\omega}{2}\left[2L - \left(L^2 - M^2\right)\left(C_c + 2C_p\right)\omega^2 + R_s^2\left(C_c + 2C_p\right)\right] \\
&\quad + \frac{j\omega R_s}{2}\left(1 - L\left(C_c + 2C_p\right)\omega^2\right), \\
D(s) &= \left[\left(L^2 - M^2\right)C_p\left(C_c + C_p\right)\omega^4 - \left[L\left(C_c + 2C_p\right) + R_s^2 C_p\left(C_c + C_p\right)\right]\omega^2 + 1\right] \\
&\quad + j\omega R_s\left[C_c + 2C_p - 2LC_p\left(C_c + C_p\right)\omega^2\right].
\end{aligned} \tag{4.39}$$

At the oscillation frequency ω_{osc} ($= \omega_L$ or ω_H), (4.39) can be written as

$$Z_{in} = \frac{N(j\omega_{osc})}{D(j\omega_{osc})} \tag{4.40}$$

where

$$\begin{aligned}
N(j\omega_{osc}) &= \left[1 - L\left(C_c + 2C_p\right)\omega_{osc}^2\right] + \\
&\qquad j\left[\frac{L\omega}{R_s}\left(1 - \frac{\omega_{osc}^2}{\omega_z^2}\right) + \frac{R_s}{2}\left(C_c + 2C_p\right)\omega_{osc}\right],
\end{aligned} \tag{4.41}$$

and

$$D(j\omega_{osc}) = -R_s C_p \left(C_c + C_p\right) \omega_{osc}^2 + j\omega_{osc} \left[\left(C_c + 2C_p\right) - 2LC_p \left(C_c + C_p\right) \omega_{osc}^2\right]. \tag{4.42}$$

For $L\omega_{osc}/R_s \gg 1$ and $1/(R_s C_p \omega_{osc}) \gg 1$, the amplitude of Z_{in} in (4.40) can be approximated as

$$|Z_{in,R_s}| \approx \frac{L}{R_s \left(C_c + 2C_p\right)} \frac{1 - \dfrac{\omega_{osc}^2}{\omega_z^2}}{1 - \dfrac{2\left(\alpha + 1\right)}{\left(\alpha + 2\right)} \dfrac{\omega_{osc}^2}{\omega_o^2}}. \tag{4.43}$$

In the same way, it can be readily shown that the amplitude of Z_{in} in (4.8) at the resonance frequency ω_{osc} is well approximated as

$$\left|Z_{in,R_p}\right| \approx \frac{R_p}{2}. \tag{4.44}$$

By Equating Z_{in} amplitudes in (4.43) and (4.44), the expressions for R_{p,ω_L} and R_{p,ω_H} can be obtained as reported in (4.11) and (4.12), respectively.

5. CONCLUSION

The work described in this thesis has been concerned with the development of a broadband complex permittivity spectroscopy system. The sensing system indirectly measures the complex admittance of the sensing capacitor exposed to the MUT. A quadrature downconversion architecture is employed to detect the magnitude and phase of the RF signals in a voltage divider circuit comprising the sensing element and a fixed capacitor. Depending on the operating frequency band, the downconversion chain has two different fundamental configurations. At lower frequencies where the system sensitivity can be degraded by harmonic mixing phenomenon, the system performs as a direct-conversion topology with 3^{rd} and 5^{th} harmonic-rejection. On the other hand, at higher frequencies, it has a dual-downconversion architecture and utilizes a sub-harmonic mixing method to reduce the required frequency range of the master clock. Implemented in 0.18-μm CMOS, the proposed system is able to measure the permittivity of organic chemicals under test with an rms error of less than 1% in the frequency range of 0.62-10 GHz.

Two wide-tuning-range VCOs have been proposed to generate the required RF signals for the sensor: 1) A triple-band VCO is presented based on an LC resonator with three possible oscillation frequencies. Implemented in 0.18μm CMOS technology, the VCO prototype covers a frequency range of 5.12-12.95 GHz and achieves excellent phase noise performance across the whole band, and (2) a novel dual-band quadrature oscillator is reported using a transformer-based LC ring. The proposed structure is verified by a prototype in 65-nm CMOS technology, which achieves low phase-noise performance and covers a wide frequency range of 2.75-6.25 GHz. A thorough analysis of the QVCOs operation and its performance is also provided.

The next-generation chip will incorporate a frequency synthesizer using one of the proposed wide-tuning range VCOs, enabling a self-sustained operation for the sensor. The integrated spectrometer chip will be also combined with a microfluidic module on top of the sensing capacitor to realize a miniaturized portable BDS platform.

REFERENCES

[1] M. M. Bajestan, A. A. Helmy, H. Hedayati, and K. Entesari, "A 0.62-10 GHz CMOS dielectric spectroscopy system for chemical/biological material characterization," in *IEEE MTT-S International Microwave Symposium Digest*, Jun. 2014.

[2] F. Buckley and A. A. Maryott, "Tables of dielectric dispersion data for pure liquids and dilute solutions," U.S. Dept. of Commerce, National Bureau of Standards, 1958.

[3] A. P. Gregory and R. N. Clarke, "Tables of the complex permittivity of dielectric reference liquids at frequencies up to 5 GHz," NPL Report MAT 23, Jan. 2012.

[4] F. Kremer and A. Schonhals, *Broadband Dielectric Spectroscopy.* Springer Berlin Heidelberg, 2003.

[5] K. Folgero, T. Friiso, J. Hilland, and T. Tjomsland, "A broad-band and high-sensitivity dielectric spectroscopy measurement system for quality determination of low-permittivity fluids," *Measurement Science and Technology*, vol. 6, no. 7, pp. 995–1008, 1995.

[6] M. Venkatesh and G. Raghavan, "An overview of microwave processing and dielectric properties of agri-food materials," *Biosystems Engineering*, vol. 88, no. 1, pp. 1 – 18, 2004.

[7] N. Miura, S. Yagihara, and S. Mashimo, "Microwave dielectric properties of solid and liquid foods investigated by time-domain reflectometry," *Journal of Food Science*, vol. 68, no. 4, pp. 1396–1403, 2003.

[8] G. Smith, A. P. Duffy, J. Shen, and C. J. Olliff, "Dielectric relaxation spectroscopy and some applications in the pharmaceutical sciences," *J. Pharm. Sci.*, vol. 84, pp. 1029–1044., Sep. 1995.

[9] A. Lonappan, G. Bindu, V. Thomas, J. Jacob, C. Rajasekaran, and K. T. Mathew, "Diagnosis of diabetes mellitus using microwaves," *Journal of Electromagnetic Waves and Applications*, vol. 21, no. 10, pp. 1393–1401, 2007.

[10] A. Lonappan, V. Thomas, G. Bindu, C. Rajasekaran, and K. T. Mathew, "Non-destructive measurement of human blood at microwave frequencies," *Journal of Electromagnetic Waves and Applications*, vol. 21, no. 8, pp. 1131–1139, 2007.

[11] K. Grenier, D. Dubuc, T. Chen, F. Artis, T. Chretiennot, M. Poupot, and J. Fournie, "Recent advances in microwave-based dielectric spectroscopy at the cellular level for cancer investigations," *IEEE Transactions on Microwave Theory and Techniques*, vol. 61, no. 5, pp. 2023–2030, May 2013.

[12] K. Heileman, J. Daoud, and M. Tabrizian, "Dielectric spectroscopy as a viable biosensing tool for cell and tissue characterization and analysis," *Biosensors and Bioelectronics*, vol. 49, pp. 348 – 359, 2013.

[13] Y. Feldman, I. Ermolina, and Y. Hayashi, "Time domain dielectric spectroscopy study of biological systems," *IEEE Trans. Dielect. Elect. Insul.*, vol. 10, no. 5, pp. 728–753, Oct. 2003.

[14] J. Zhuang, K. Schoenbach, and J. Kolb, "Time domain dielectric spectroscopy of biological cells after pulsed electric field exposure," in *Annu. Rep. Elect. Insul. Dielect. Phenomena Conf.*, Oct. 2011, pp. 44–47.

[15] A. Cataldo, L. Tarricone, F. Attivissimo, and A. Trotta, "A TDR method for real-time monitoring of liquids," *IEEE Trans. Instrum. Meas.*, vol. 56, no. 5,

pp. 1616–1625, Oct. 2007.

[16] K. Saeed, A. Guyette, I. Hunter, and R. D. Pollard, "Microstrip resonator technique for measuring dielectric permittivity of liquid solvents and for solution sensing," in *IEEE MTT-S Int. Microw. Symp. Dig.*, Jun. 2007, pp. 1185–1188.

[17] K. Saeed, R. D. Pollard, and I. Hunter, "Substrate integrated waveguide cavity resonators for complex permittivity characterization of materials," *IEEE Trans. Microw. Theory Techn.*, vol. 56, no. 10, pp. 2340–2347, Oct. 2008.

[18] P. Bernard and J. Gautray, "Measurement of dielectric constant using a microstrip ring resonator," *IEEE Trans. Microw. Theory Techn.*, vol. 39, no. 3, pp. 592–595, Mar. 1991.

[19] V. Sekar, W. Torke, S. Palermo, and K. Entesari, "A self-sustained microwave system for dielectric-constant measurement of lossy organic liquids," *IEEE Trans. Microw. Theory Techn.*, vol. 60, no. 5, pp. 1444–1455, May 2012.

[20] T. Chretiennot, D. Dubuc, and K. Grenier, "A microwave and microfluidic planar resonator for efficient and accurate complex permittivity characterization of aqueous solutions," *IEEE Trans. Microw. Theory Techn.*, vol. 61, no. 2, pp. 972–978, Feb. 2013.

[21] K. Saeed, R. D. Pollard, and I. Hunter, "Substrate integrated waveguide cavity resonators for complex permittivity characterization of materials," *IEEE Transactions on Microwave Theory and Techniques*, vol. 56, no. 10, pp. 2340–2347, Oct. 2008.

[22] P. A. Bernard and J. M. Gautray, "Measurement of dielectric constant using a microstrip ring resonator," *IEEE Transactions on Microwave Theory and Techniques*, vol. 39, no. 3, pp. 592–595, Mar. 1991.

[23] A. Helmy, H.-J. Jeon, Y.-C. Lo, A. Larsson, R. Kulkarni, J. Kim, J. Silva-Martinez, and K. Entesari, "A self-sustained CMOS microwave chemical sensor using a frequency synthesizer," *IEEE Journal of Solid-State Circuits*, vol. 47, no. 10, pp. 2467–2483, Oct. 2012.

[24] O. Elhadidy, M. Elkholy, A. Helmy, S. Palermo, and K. Entesari, "A CMOS fractional-N PLL-based microwave chemical sensor with 1.5 % permittivity accuracy," *IEEE Transactions on Microwave Theory and Techniques*, vol. 61, no. 9, pp. 3402–3416, Sep. 2013.

[25] M. Bakhshiani, M. Suster, and P. Mohseni, "A broadband sensor interface IC for miniaturized dielectric spectroscopy from MHz to GHz," *IEEE Journal of Solid-State Circuits*, vol. 49, no. 8, Aug. 2014.

[26] J.-C. Chien, M. Anwar, E.-C. Yeh, L. Lee, and A. Niknejad, "A 1-50 GHz dielectric spectroscopy biosensor with integrated receiver front-end in 65nm CMOS," in *IEEE MTT-S International Microwave Symposium Digest*, Jun. 2013.

[27] A. Helmy, S. Kabiri, M. M. Bajestan, and K. Entesari, "A miniaturized spectroscopy system for complex permittivity detection of organic mixtures in the 0.65-2 GHz frequency range," in *IEEE MTT-S International Microwave Symposium Digest*, Jun. 2013.

[28] A. A. Helmy, S. Kabiri, M. M. Bajestan, and K. Entesari, "Complex permittivity detection of organic chemicals and mixtures using a 0.5-3 GHz miniaturized spectroscopy system," *IEEE Transactions on Microwave Theory and Techniques*, vol. 61, no. 12, pp. 4646–4659, Dec. 2013.

[29] B. Razavi, *RF Microelectronics, 2nd ed.* Prentice Hall, 2012.

[30] H.-K. Cha, K. Kwon, J. Choi, H.-T. Kim, and K. Lee, "A CMOS wideband RF front-end with mismatch calibrated harmonic rejection mixer for terrestrial digital TV tuner applications," *IEEE Transactions on Microwave Theory and Techniques*, vol. 58, no. 8, pp. 2143–2151, Aug. 2010.

[31] S. Lerstaveesin, M. Gupta, D. Kang, and B.-S. Song, "A 48-860 MHz CMOS low-IF direct-conversion DTV tuner," *IEEE Journal of Solid-State Circuits*, vol. 43, no. 9, pp. 2013–2024, Sep. 2008.

[32] Z. Ru, N. Moseley, E. Klumperink, and B. Nauta, "Digitally enhanced software-defined radio receiver robust to out-of-band interference," *IEEE Journal of Solid-State Circuits*, vol. 44, no. 12, pp. 3359–3375, Dec. 2009.

[33] M. El-Nozahi, A. Amer, E. Sanchez-Sinencio, and K. Entesari, "A millimeter-wave (24/31GHz) dual-band switchable harmonic receiver in 0.18-μm SiGe process," *IEEE Transactions on Microwave Theory and Techniques*, vol. 58, no. 11, pp. 2717–2730, Nov. 2010.

[34] H. Wang, "A 1.8-V 3-mW 16.8-GHz frequency divider in 0.25-μm CMOS," in *IEEE International Solid-State Circuits Conference Digest of Technical Papers*, Feb. 2000, pp. 196–197.

[35] J. Wong, V.-L. Cheung, and H. Luong, "A 1-V 2.5-mW 5.2-GHz frequency divider in a 0.35-μm CMOS process," *IEEE Journal of Solid-State Circuits*, vol. 38, no. 10, pp. 1643–1648, Oct. 2003.

[36] M. Demirkan, S. Bruss, and R. Spencer, "Design of wide tuning-range CMOS VCOs using switched coupled-inductors," *IEEE J. Solid-State Circuits*, vol. 43, no. 5, pp. 1156–1163, May 2008.

[37] A. Bevilacqua, F. Pavan, C. Sandner, A. Gerosa, and A. Neviani, "A 3.4-7 GHz transformer-based dual-mode wideband VCO," in *Proc. IEEE Eur. Solid-State Circuits Conf. (ESSCIRC)*, Sep. 2006, pp. 440–443.

[38] J. Borremans, S. Bronckers, P. Wambacq, M. Kuijk, and J. Craninckx, "A single-inductor dual-band VCO in a 0.06 mm^2 5.6 GHz multi-band front-end in 90 nm digital CMOS," in *IEEE Int. Solid-State Circuits Conf. (ISSCC) Dig.*, Feb. 2008, pp. 324–616.

[39] G. Li, L. Liu, Y. Tang, and E. Afshari, "A low-phase-noise wide-tuning-range oscillator based on resonant mode switching," *IEEE J. Solid-State Circuits*, vol. 47, no. 6, pp. 1295–1308, Jun. 2012.

[40] Z. Safarian and H. Hashemi, "Wideband multi-mode CMOS VCO design using coupled inductors," *IEEE Trans. Circuits Syst. I, Reg. Papers*, vol. 56, no. 8, pp. 1830–1843, Aug. 2009.

[41] A. Rofougaran, J. Rael, M. Rofougaran, and A. Abidi, "A 900 MHz CMOS LC-oscillator with quadrature outputs," in *IEEE Int. Solid-State Circuits Conf. (ISSCC) Dig.*, Feb. 1996, pp. 392–393.

[42] A. Mazzanti, F. Svelto, and P. Andreani, "On the amplitude and phase errors of quadrature LC-tank CMOS oscillators," *IEEE J. Solid-State Circuits*, vol. 41, no. 6, pp. 1305–1313, Jun. 2006.

[43] S. Li, I. Kipnis, and M. Ismail, "A 10 GHz CMOS quadrature LC-VCO for multirate optical applications," *IEEE J. Solid-State Circuits*, vol. 38, no. 10, pp. 1626–1634, Oct. 2003.

[44] H. Tong, S. Cheng, Y.-C. Lo, A. Karsilayan, and J. Silva-Martinez, "An LC quadrature VCO using capacitive source degeneration coupling to eliminate bi-

modal oscillation," *IEEE Trans. Circuits Syst. I, Reg. Papers*, vol. 59, no. 9, pp. 1871–1879, Sep. 2012.

[45] D. Huang, W. Li, J. Zhou, N. Li, and J. Chen, "A frequency synthesizer with optimally coupled QVCO and harmonic-rejection SSBmixer for multi-standard wireless receiver," *IEEE J. Solid-State Circuits*, vol. 46, no. 6, pp. 1307–1320, Jun. 2011.

[46] J. van der Tang, P. van de Ven, D. Kasperkovitz, and A. van Roermund, "Analysis and design of an optimally coupled 5-GHz quadrature LC oscillator," *IEEE J. Solid-State Circuits*, vol. 37, no. 5, pp. 657–661, May 2002.

[47] L. Romano, S. Levantino, C. Samori, and A. Lacaita, "Multiphase LC oscillators," *IEEE Trans. Circuits Syst. I, Reg. Papers*, vol. 53, no. 7, pp. 1579–1588, Jul. 2006.

[48] L. Romano, A. Bonfanti, S. Levantino, C. Samori, and A. Lacaita, "5 GHz oscillator array with reduced flicker up-conversion in 0.13-μm CMOS," *IEEE J. Solid-State Circuits*, vol. 41, no. 11, pp. 2457–2467, Nov. 2006.

[49] A. Mazzanti and P. Andreani, "A time-variant analysis of fundamental $1/f^3$ phase noise in CMOS parallel LC-tank quadrature oscillators," *IEEE Trans. Circuits Syst. I, Reg. Papers*, vol. 56, no. 10, pp. 2173–2180, Oct. 2009.

[50] L. Romano, S. Levantino, A. Bonfanti, C. Samori, and A. Lacaita, "Phase noise and accuracy in quadrature oscillators," in *Int. Symp. on Circuits and Systems (ISCAS)*, May 2004.

[51] S. L. J. Gierkink, S. Levantino, R. Frye, C. Samori, and V. Boccuzzi, "A low-phase-noise 5-GHz CMOS quadrature VCO using superharmonic coupling," *IEEE J. Solid-State Circuits*, vol. 38, no. 7, pp. 1148–1154, Jul. 2003.

[52] X. Yi, C. C. Boon, H. Liu, J. F. Lin, and W. M. Lim, "A 57.9-to-68.3 GHz 24.6 mW frequency synthesizer with in-phase injection-coupled QVCO in 65 nm CMOS technology," *IEEE J. Solid-State Circuits*, vol. 49, no. 2, pp. 347–359, Feb. 2014.

[53] A. Mirzaei, M. Heidari, R. Bagheri, S. Chehrazi, and A. Abidi, "The quadrature LC oscillator: A complete portrait based on injection locking," *IEEE J. Solid-State Circuits*, vol. 42, no. 9, pp. 1916–1932, Sep. 2007.

[54] U. Decanis, A. Ghilioni, E. Monaco, A. Mazzanti, and F. Svelto, "A low-noise quadrature VCO based on magnetically coupled resonators and a wideband frequency divider at millimeter waves," *IEEE J. Solid-State Circuits*, vol. 46, no. 12, pp. 2943–2955, Dec. 2011.

[55] G. Li and E. Afshari, "A low-phase-noise multi-phase oscillator based on left-handed LC-ring," *IEEE J. Solid-State Circuits*, vol. 45, no. 9, pp. 1822–1833, Sep. 2010.

[56] G. Li and E. Afshari, "A low-phase-noise wide-tuning-range quadrature oscillator in 65 nm CMOS," in *Proc. IEEE Custom Integrated Circuits Conf. (CICC)*, Sep. 2012.

[57] S. Rong and H. Luong, "Analysis and design of transformer-based dual-band VCO for software-defined radios," *IEEE Trans. Circuits Syst. I, Reg. Papers*, vol. 59, no. 3, pp. 449–462, Mar. 2012.

[58] C. T. Fu and H. Luong, "A 0.8-V CMOS quadrature LC VCO using capacitive coupling," in *IEEE Asian Solid-State Circuits Conf.*, Nov. 2007, pp. 436–439.

[59] A. Ng and H. Luong, "A 1-V 17-GHz 5-mW CMOS quadrature VCO based on transformer coupling," *IEEE J. Solid-State Circuits*, vol. 42, no. 9, pp. 1933–

1941, Sep. 2007.

[60] M. Bajestan, V. Rezaei, and K. Entesari, "A 2.75-6.25 GHz low-phase-noise quadrature VCO based on a dual-mode ring resonator in 65 nm CMOS," in *IEEE Radio Frequency Integrated Circuits Symp. Dig.*, Jun. 2014, pp. 265–268.

[61] J. Borremans, A. Bevilacqua, S. Bronckers, M. Dehan, M. Kuijk, P. Wambacq, and J. Craninckx, "A compact wideband front-end using a single-inductor dual-band VCO in 90 nm digital CMOS," *IEEE J. Solid-State Circuits*, vol. 43, no. 12, pp. 2693–2705, Dec. 2008.

[62] B. Razavi, "Multi-decade carrier generation for cognitive radios," in *Symp. on VLSI Circuits*, Jun. 2009, pp. 120–121.

[63] M. Bajestan and K. Entesari, "A 5.12-12.95 GHz triple-resonance low phase noise CMOS VCO for software-defined radio applications," in *IEEE Radio Frequency Integrated Circuits Symp. Dig.*, Jun. 2013, pp. 195–198.

[64] A. Hajimiri and T. Lee, "A general theory of phase noise in electrical oscillators," *IEEE J. Solid-State Circuits*, vol. 33, no. 2, pp. 179–194, Feb. 1998.

[65] P. Andreani, "A time-variant analysis of the $1/f^2$ phase noise in CMOS parallel LC-tank quadrature oscillators," *IEEE Trans. Circuits Syst. I, Reg. Papers*, vol. 53, no. 8, pp. 1749–1760, Aug. 2006.

[66] C. Samori, A. Lacaita, F. Villa, and F. Zappa, "Spectrum folding and phase noise in LC tuned oscillators," *IEEE Trans. Circuits Syst. II, Analog Digit. Signal Process.*, vol. 45, no. 7, pp. 781–790, Jul. 1998.

[67] S. Rong and H. Luong, "A 1V 4GHz-and-10GHz transformer-based dual-band quadrature VCO in 0.18-μm CMOS," in *Proc. IEEE Custom Integrated Circuits Conf. (CICC)*, Sep. 2007, pp. 817–820.

[68] G. Cusmai, M. Repossi, G. Albasini, A. Mazzanti, and F. Svelto, "A magnetically tuned quadrature oscillator," *IEEE J. Solid-State Circuits*, vol. 42, no. 12, pp. 2870–2877, Dec. 2007.

[69] S. Saberi and J. Paramesh, "A 11.5-22 GHz dual-resonance transformer-coupled quadrature VCO," in *IEEE Radio Frequency Integrated Circuits Symp. Dig.*, Jun. 2011.